Signal Design and Processing Techniques for WSR-88D Ambiguity Resolution

Staggered PRT Algorithm Updates, the CLEAN-AP Filter, and the Hybrid Spectrum Width Estimator

National Severe Storms Laboratory Report

prepared by: **Sebastian Torres, David Warde, Beatriz Gallardo, Khoi Le, and Dusan Zrnic**

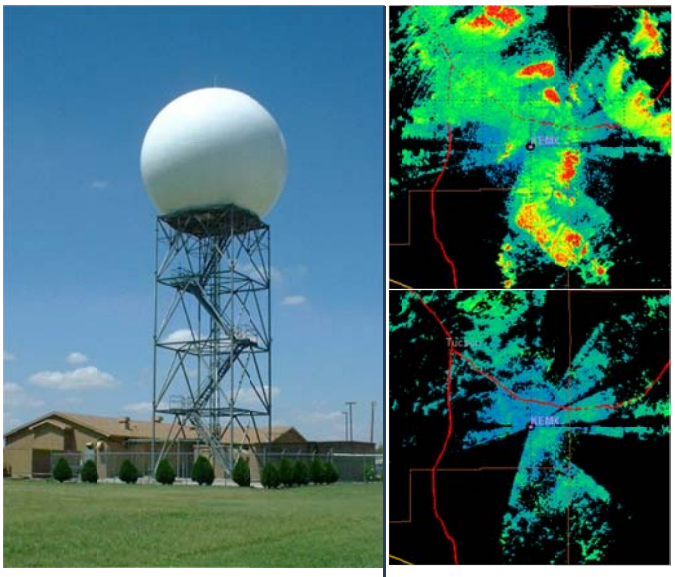

Part 14
December 2010

National Oceanic and Atmospheric Administration
National Severe Storms Laboratory

SIGNAL DESIGN AND PROCESSING TECHNIQUES FOR WSR-88D AMBIGUITY RESOLUTION

Part 14: Staggered PRT Algorithm Updates, the CLEAN-AP Filter, and the Hybrid Spectrum Width Estimator

National Severe Storms Laboratory Report

prepared by: Sebastián Torres, David Warde, Beatriz Gallardo, Khoi Le, and Dusan Zrnić

December 2010

NOAA, National Severe Storms Laboratory
120 David L. Boren Blvd., Norman, Oklahoma 73072

SIGNAL DESIGN AND PROCESSING TECHNIQUES FOR WSR-88D AMBIGUITY RESOLUTION

Part 14: Staggered PRT Algorithm Updates, the CLEAN-AP Filter, and the Hybrid Spectrum Width Estimator

Contents

SIGNAL DESIGN AND PROCESSING TECHNIQUES FOR WSR-88D AMBIGUITY RESOLUTION

Part 14: Staggered PRT Algorithm Updates, the CLEAN-AP Filter, and the Hybrid Spectrum Width Estimator

1. Introduction

The Radar Operations Center (ROC) of the National Weather Service (NWS) has funded the National Severe Storms Laboratory (NSSL) to address data quality improvements for the WSR-88D. This is the fourteenth report in the series that deals with range and velocity ambiguity resolution and other data quality techniques for the WSR-88D (other relevant reports are listed at the end). It documents NSSL accomplishments in FY10.

Section 2 provides a brief review of the SPRT algorithm and the modifications that are needed to accommodate dual polarization data. Alternative solutions for ground clutter filtering the two polarization channels are evaluated and a recommendation is provided. Although changes with respect to the single-polarization version are minimal, a complete description of the recommended algorithm is included. Simulations show that the recommended dual-pol SPRT algorithm exhibits good performance under realistic conditions. These results are validated with examples from real data processed with the recommended algorithm.

Section 3 describes and documents the performance of the CLEAN-AP filter. This ground clutter filter was developed for the National Weather Radar Testbed Phased Array Radar (NWRT PAR), but is recommended as a complete ground-clutter mitigation

technique for future upgrades of the WSR-88D. CLEAN-AP combines automatic detection and filtering capabilities so that seamless integration with other functions in the signal processing pipeline is possible. The performance of the CLEAN-AP filter is extensively quantified using simulations within the framework outlined by the NEXRAD Technical Requirements (NTR). The filter is shown to meet NTR and exceed the already superior performance of GMAP. Real data analyses are also included to demonstrate the performance of this novel scheme on mechanically scanned radars. Qualitative comparisons with the currently operational clutter mitigation scheme reveal the potential for improved data quality with less user intervention.

Section 4 is devoted to the analysis of the hybrid spectrum width estimator proposed by NCAR. This independent evaluation confirms that the proposed estimator outperforms the classical spectrum width estimator in most situations. However, modifications to the proposed hybrid estimator are recommended to further improve the performance. These include adaptive thresholds for estimator selection, an additional spectrum width estimator, and enhanced censoring rules for quality control.

This report also includes two appendices. Appendix A contains the latest description of the staggered PRT algorithm that is able to produce spectral moments and polarimetric variables. Appendix B includes one relevant conference paper on the CLEAN-AP filter that was presented at the last AMS Radar Meteorology conference.

Once again, the work performed in FY10 exceeded considerably the allocated budget; hence, a part of it had to be done on other NOAA funds.

2. Staggered PRT in the Dual-Polarization Era

2.1. The Dual-Polarization Staggered PRT Algorithm

The July 2009 algorithm description addressed the integration and documentation of the ground clutter filter as well as the recovery of overlaid echoes. For the ground clutter filter, the SACHI filter (Report 2009) is used on segments I and II, see Fig. 2.1, and DC removal is used on the overlaid segment I. The recovery of overlaid echoes allows the use of shorter PRTs for better performance while meeting range coverage requirements.

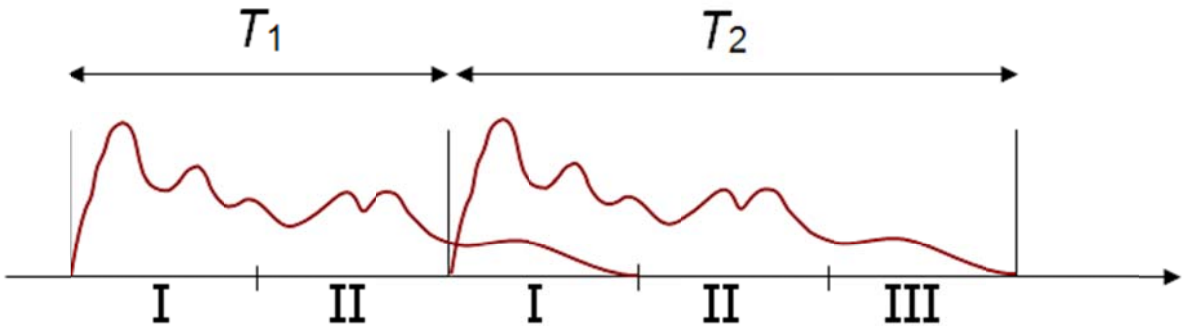

Fig. 2.1. Overlaid echoes in SPRT.

Staggered PRT is currently scheduled for operational implementation after the dual polarization upgrade. Therefore, an algorithm that provides polarimetric variable computations must be provided. The inputs for this algorithm are the time series for the horizontal and vertical polarization channels, V_h and V_v, respectively. The outputs are the spectral moments: reflectivity, velocity and spectrum width; and the polarimetric variables: differential reflectivity, differential phase and cross-correlation coefficient.

2.1.1. *Algorithm Steps*

The previous SPRT algorithm was modified to accommodate the computations required to produce dual-polarization variables; a few existing steps were modified and a few new ones were added. These changes are summarized in Fig. 2.2. and explained next.

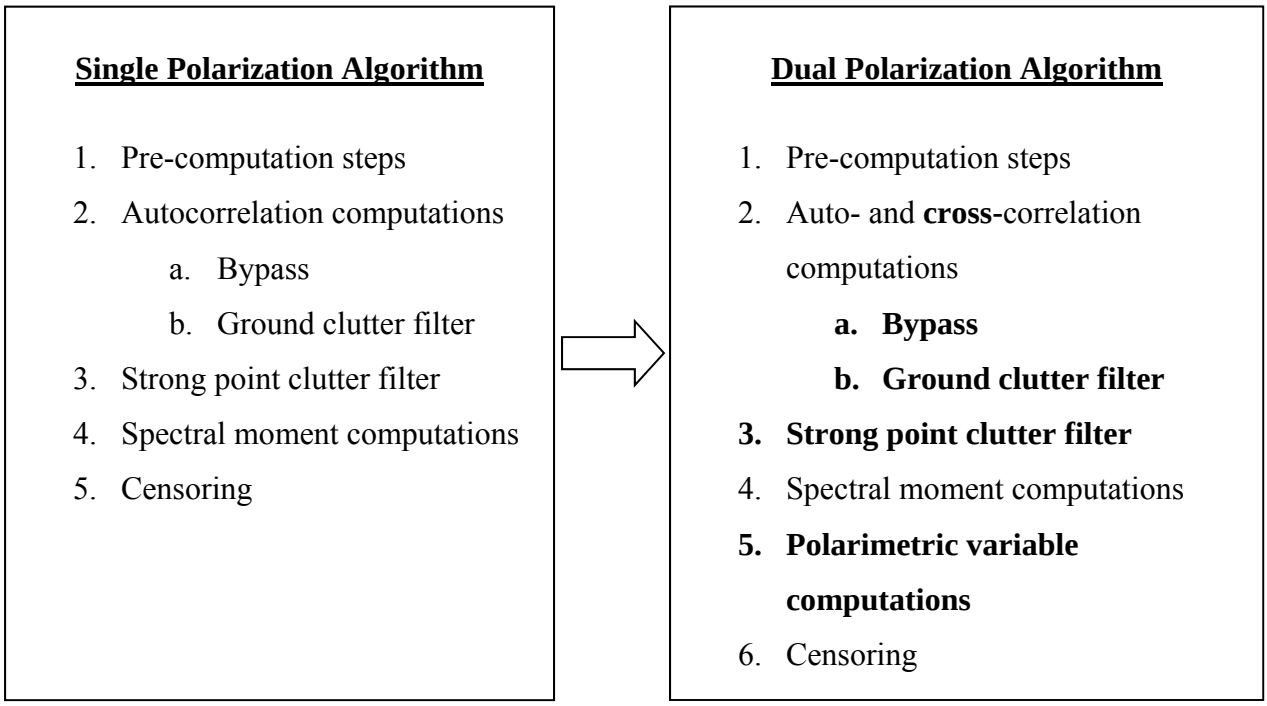

Fig. 2.2. Changes to the staggered PRT algorithm for the dual polarization implementation. Bold fonts denote changes or additions.

1. *Pre-computation steps*

   This set of steps, which defines the velocity dealiasing rules and other constants for the SACHI clutter filter, doesn't need any changes.

2. *Auto- and cross- correlation computations*

   Either for the bypass or the ground clutter filter schemes, some computations must be added to later calculate the polarimetric variables. The required computations are:

   2.1. H-channel mean power

   2.2. V-channel mean power

2.3. H-channel lag-1 correlation

2.4. **H-channel and V-channel cross-correlation**

For the bypass mode (i.e., no clutter filtering) the computations will be done for each PRT, and then combined according to the range segment (see the Appendix for the detailed expressions). Similarly, the DC removal is applied in the time-domain, H- and V- channels will be filtered independently following the bypass procedure. On the other hand, the SACHI ground clutter filter, which is used in the frequency domain, will provide these computations directly.

3. *Strong point clutter filter*

   The strong point clutter filter is applied based on the H-channel power and applied to all power, autocorrelation, and cross-correlation arrays.

4. *Spectral moment computations*

   The calculations for reflectivity, velocity and spectrum width use the H-channel computations from step 2: H-channel mean power and H-channel lag-1 correlation.

5. *Polarimetric variable computations*

   The calculations of differential reflectivity, differential phase and correlation coefficient use the computations from step 2: H-channel mean power, V-channel mean power, and H-channel V-channel cross-correlation.

6. *Censoring*

   The non-significant return arrays for reflectivity, velocity, and spectrum width are determined. The array for reflectivity is also used for the polarimetric variables. The determination of overlaid returns is done by using the mean power of the H-channel.

2.1.2. *The SACHI Filter*

The SACHI filter that is currently recommended for use in the SPRT algorithm has the following high-level steps:

1. *Extended spectrum computation*

   The SPRT time series with M samples are interpolated with zeroes so that an extended uniform PRT sequence of $5M/2$ samples is built. A uniform sequence is needed to go to the frequency domain. Because of this manipulation, the spectrum of the extended time series will contain the original spectrum of weather and clutter as well as their "replicas".

2. *Notchwidth determination*

   The GMAP clutter filter is applied to one fifth of the spectrum around zero velocity. GMAP returns a value for the notch width.

3. *Ground clutter filtering*

   The ground clutter contamination around zero Doppler is removed with the notch filter obtained in 2). Clutter components projected to $\pm 2v_a/5$ and $\pm 4v_a/5$ are also removed.

4. *Magnitude deconvolution*

   A magnitude deconvolution is applied at this point. This means that only the amplitude of the matrix coefficients is obtained.

5. *Interpolation*

   Values across zero Doppler are linearly interpolated

6. *Power and autocorrelations for spectral moments*

   Two-fifths of the spectrum around the estimated weather velocity are retained. Then, the power and autocorrelations for spectral moments are computed.

As it can be seen, the phases of the spectral components are lost in step 4). Since the polarimetric variable computations require this phase, the SACHI filter has to be modified. Recall that it must produce filtered power computations for both channels, H-channel lag-1 correlation, and H-channel V-channel cross correlation.

Two different solutions were considered. First, the spectral reconstruction method, presented by Sachinanda and Zrnić (2006) was tested. This is a complex solution that also serves a broader need. The spectral reconstruction, which can be performed in the time or frequency domains, allows the recovery of the phases of weather signals after the ground clutter has been filtered. Because the SACHI ground clutter filter operates in the frequency domain, the second approach was chosen for these tests. In this approach, the spectrum is reconstructed over two-fifths of the total number of spectral coefficients centered on the estimated mean velocity. The remaining coefficients are set to zero. This method is only valid if the original signal spectrum agrees with the definition of "narrow spectrum." That is, the spread of the nonzero spectral coefficients is less than $M/2$ coefficients in the $5M/2$ -point DFT extended spectrum for the conventional staggered ratio of $\kappa = 2/3$. In the absence of ground clutter contamination, the spectrum can be fully restored. Otherwise, the reconstruction is made for just $(M - n_c)$ coefficients, where n_c is the clutter filter width. An important drawback is that this method relies on the accuracy of the weather velocity estimation. When catastrophic errors occur, the spectrum is erroneously reconstructed.

Due to the complexity and limitations of the spectral reconstruction method, a new method was developed. This is a direct method that uses the remaining complex spectral coefficients after ground clutter filtering (step 3) to perform the cross-correlation computations. Simulations were used to compare the performance of both methods. The results are shown in Fig. 2.3. The parameters used in these simulations are as follows:

- Weather:
    - $SNR_h = 40$ dB, $v = 20$ m/s, $w = [0.5, 8]$ m/s
    - $Z_{DR} = 3$ dB, $\Phi_{DP} = -30$ deg, $\rho_{HV} = 0.90$

- Clutter:
    - CSR_h = 40 dB, v = 0, w = 0.28 m/s,
    - Z_{DR} = -0 dB, Φ_{DP} = -30 deg, ρ_{HV} = 0.80
- v_a = 50 m/s, M = 64.
- Number of realizations = 1000.

Fig 2.3 shows the errors from the spectral reconstruction and direct methods. They are the additional errors of estimates introduced by each processing option with respect to the typical statistical errors obtained by time-domain computation of clutter-free signals. Two time series are independently generated for each method; one for the ground clutter and the other for the weather signal. The reference estimates (Z_{DR}, Φ_{DP}, and ρ_{HV}) are obtained from the *windowed* weather signal using the pulse-pair processing of time series. The sum of the weather and the ground clutter time series is processed with the clutter filter and then the direct or spectral reconstruction method; that is, the second set of parameters are estimated from the final spectrum (directly estimated or reconstructed). Statistical errors are computed with respect to the reference estimates.

The results show little difference between the direct and spectral reconstruction methods. The biases of polarimetric variables are almost zero for both methods, whereas there is a small difference in the standard deviations. However, it is very small for both cases: less than 0.25 dB for differential reflectivity, 1.5 degrees for differential phase, and 0.001 for cross-correlation coefficient. For all variables, errors are slightly smaller for the spectral reconstruction approach for spectrum widths between 1.5 and 6 m/s, whereas the behavior of the direct method is more consistent across the range of simulated parameters. This is because the spectral reconstruction method performs best under the assumption of narrow spectrum.

Due to the similar performances of both methods, the direct method was chosen due to its simplicity. The direct method also provides an easier implementation in the previous SPRT clutter filtering scheme, explained in the next section, and is independent of the mean velocity estimation (hence it is immune to catastrophic errors).

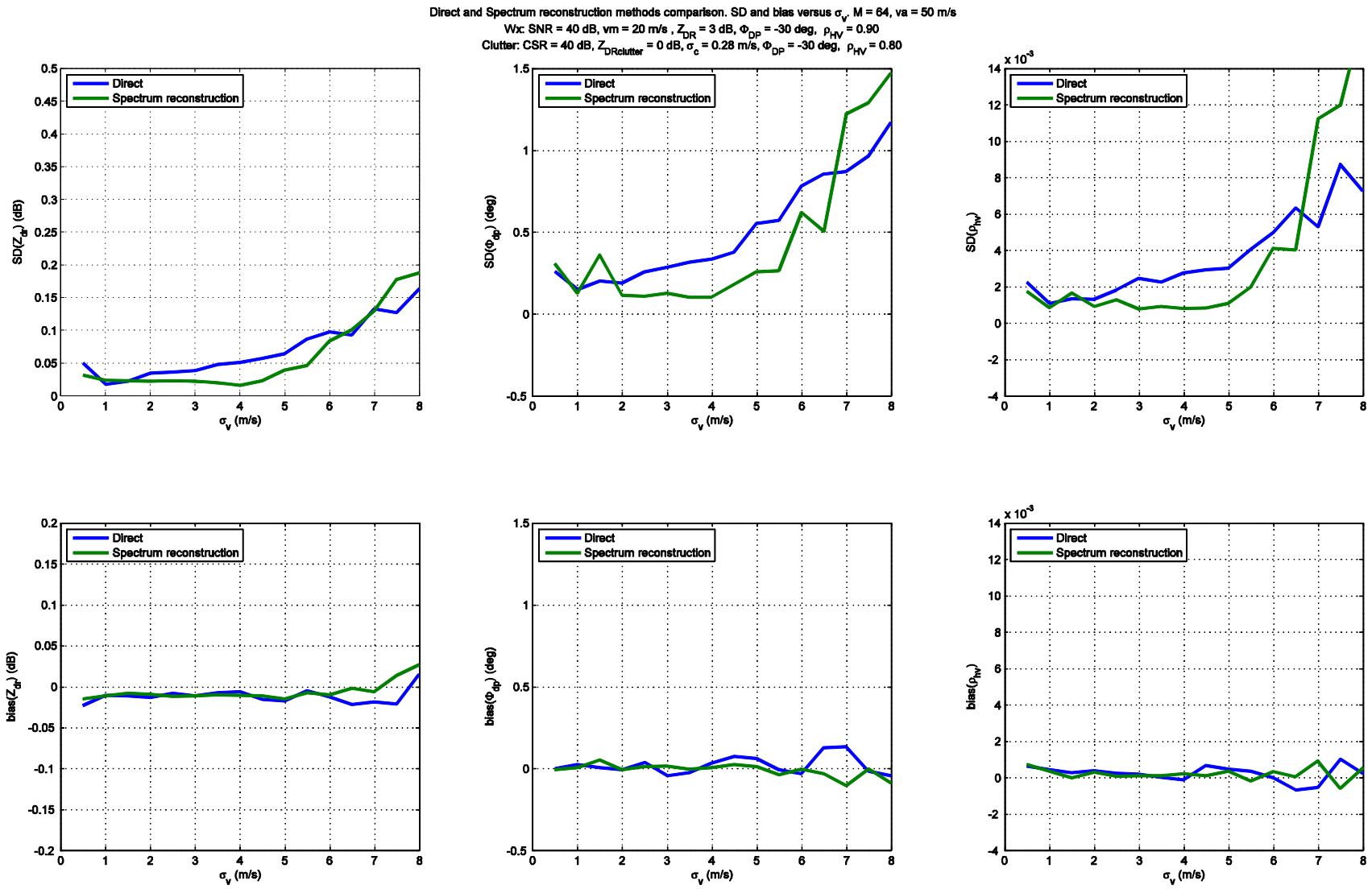

Fig. 2.3. Spectral reconstruction and direct method comparisons.

2.2. Polarimetric Variable Computations Using the Direct Method

2.2.1. *A Brief Review of Staggered PRT Processing in the Spectral Domain*

In the staggered PRT, scheme two different pulse repetition times, T_1 and T_2 ($T_1 < T_2$), are alternated. Then, alternate pairs of samples are used to compute autocorrelation estimates R_1 at lag T_1, and R_2 at lag T_2. These estimates are used to compute the spectral moments. When spectral processing is needed, we must proceed in a different way because uniform sampling is required. In this case, the signal is "reconstructed" as if it were sampled at intervals $T_u = (T_2 - T_1)$. This puts a small restriction on the selection of T_1 and T_2. Namely, they should be integer multiples of the difference T_u, so that $T_1 = n_1 T_u$ and $T_2 = n_2 T_u$, where n_1 and n_2 are integers. The best choice, as discussed in previous reports, is $n_1 = 2$ and $n_2 = 3$, or the stagger ratio $\kappa = T_1/T_2 = 2/3$. Once this condition is satisfied, we can generate an M_x-sample uniform time series, v_i, $i = 0, 1, 2, \ldots, M_x\text{-}1$, (signal sampled at intervals T_u) from the staggered PRT sequence by inserting zeros in the place of missing samples. For $\kappa = 2/3$, we have only the 1st and the 3rd samples available in each set of 5 samples. We call this the derived time series. Now, we can write the derived time series, v_i, $i = 0, 1, 2, \ldots, M_x\text{-}1$, as a product of the sequences c and e, where e is the signal time series sampled at T_u intervals, and c_i, $i = 0, 1, 2, \ldots, M_x\text{-}1$, is a code sequence of zeros and ones given by c = [1010010100… etc.] for $\kappa = 2/3$. In other words,

$$v_i = c_i e_i;\ i = 0, 1, 2, \ldots, M_x\text{-}1. \tag{2.1}$$

If there are M staggered PRT samples, we have $M_x = M(n_1+n_2)/2$ samples in the derived time series. The DFT spectrum of v is a convolution of the spectra of c and e:

$$\mathrm{DFT}(v) = \mathrm{DFT}(c) \bigstar \mathrm{DFT}(e), \tag{2.2}$$

where the symbol ★ represents the convolution operation and the DFT stands for discrete Fourier transform. We use capital letters to denote DFT coefficients of the corresponding time-domain quantities in lower-case letters, and capital bold face letters to denote matrices or vectors. The subscript '*i*' is used for time-domain quantities and the subscript '*k*' is used for spectral-domain coefficients. For example, E_k is the k^{th} spectral coefficient of DFT(*e*), and **E** is the column matrix of coefficients E_k, $k = 0, 1, 2, \ldots, M_x\text{-}1$. In matrix notation, (2.2) can be written as

$$\mathbf{V} = \mathbf{C}\,\mathbf{E}. \tag{2.3}$$

V and **E** are (M_x–by-1) column matrices and **C** is the (M_x-by-M_x) convolution matrix whose columns are cyclically shifted versions of the DFT(*c*). The convolution matrix is formed from the spectrum of the code sequence as follows: (a) Form a matrix with first row as the DFT(*c*), the second row is the same coefficients cyclically shifted to the right by one coefficient, the 3rd row is the same spectrum shifted to the right by two coefficients, and so on through the last row. This forms an M_x-by-M_x matrix. (b) Take the complex conjugate transpose of this matrix to get the convolution matrix, **C**. (c) Normalize the matrix to preserve the power in the spectrum; the columns of the convolution matrix are normalized to be unit vectors (i.e., the norm of each column vector is unity). Note that normalizing the columns also normalizes the row vectors of **C** automatically.

2.2.2. *Magnitude Deconvolution and Computation of Spectral Moments.*

The convolution matrix is singular (its rank is *M*), hence we cannot solve for **E**, but we can get the magnitudes without the phases under certain conditions as explained next. If we discard the

phases of **C**, the convolution matrix becomes non-singular and hence can be inverted. Further, we note that it is sufficient to recover the magnitude spectrum of the weather signal to recover the **spectral moments**; the phases are not needed. Hence, we discard the phases of all the three matrices in (2.3) and write $abs\{\mathbf{V}\} = abs\{\mathbf{C}\}\ abs\{\mathbf{E}\}$ which is valid under the "narrow spectrum" condition. The spectrum is considered narrow if the spectral spread of the weather signal is less than $M_x/(n_1+n_2)$ coefficients. Because the staggered PRT scheme can be designed to have a large unambiguous velocity, v_a, this condition can be *nearly* met for most weather signals. In general, $abs\{\mathbf{V}\} \neq abs\{\mathbf{C}\}abs\{\mathbf{E}\}$ because of the complex addition process; however, under the "narrow spectrum" condition, the complex addition does not take place, hence we can replace the inequality sign with the equality sign. Note that each row of **C** has only five non-zero coefficients spaced $M/2$ coefficients apart, and if **E** has only $M/2$ contiguous non-zero coefficients, the product of **E** and each row of **C** results in only one non-zero term. Hence, no complex addition takes place in the convolution operation. Therefore, we can recover $abs\{\mathbf{E}\}$ from the inverse operation

$$abs\{\mathbf{E}\} = abs([abs\{\mathbf{C}\}]^{-1} abs\{\mathbf{V}\}). \tag{2.4}$$

We refer to the operation indicated in (2.4) as the "*magnitude deconvolution*". The recovery of the magnitude spectrum is exact under the "narrow spectrum" condition. If the spread of the spectral coefficients is more than $M_x/(n_1+n_2)$, the reconstruction is not exact; however, the velocity estimate is not biased by this non-ideal reconstruction; only its variance is increased. The spectrum width bias is removed by eliminating the residual coefficients outside an interval $2M/(n_1+n_2)$ centered on the estimated weather velocity. The amplitude coefficients of $abs\{\mathbf{E}\}$ are then used to compute the signal power, P, and the short and long PRT autocorrelations, R_1 at lag

T_1 and R_2 at lag T_2. These computations allow the estimation of the three spectral moments: reflectivity, velocity, and spectrum width.

2.2.3. *Computation of Polarimetric Variables in the Spectral Domain.*

As we discussed in the previous section, the spectral moments can be calculated from the recovered *abs*{**E**} from eq. (2.4). Unfortunately, the same is not possible for the polarimetric variables because the phase is lost. However, for the computation of these variables, only the powers from both channels and the cross-correlation between the horizontal and the vertical channels are needed. That is, the spectral reconstruction is not actually needed since we can compute these values from the V_{Hk} and V_{Vk} coefficients for the horizontal and the vertical polarization, regardless of the spectral structure. In other words, the power and the cross-correlation do not depend on the sample-time autocorrelation of the time series. Thus, the spectral reconstruction is not needed. The cross-correlation and horizontal and vertical powers are calculated as

$$R_{HV} = \sum_{k=0}^{N-1} V_H^*(k) V_V(k), \tag{2.5}$$

$$P_H = \sum_{k=0}^{N-1} |V_H(k)|^2, \text{ and} \tag{2.6}$$

$$P_V = \sum_{k=0}^{N-1} |V_V(k)|^2. \tag{2.7}$$

Fig. 2.4 shows a representation of the magnitude and phase of the spectrum used to compute these values for both the direct method and the spectral reconstruction for a simulated clutter-contaminated weather time series.

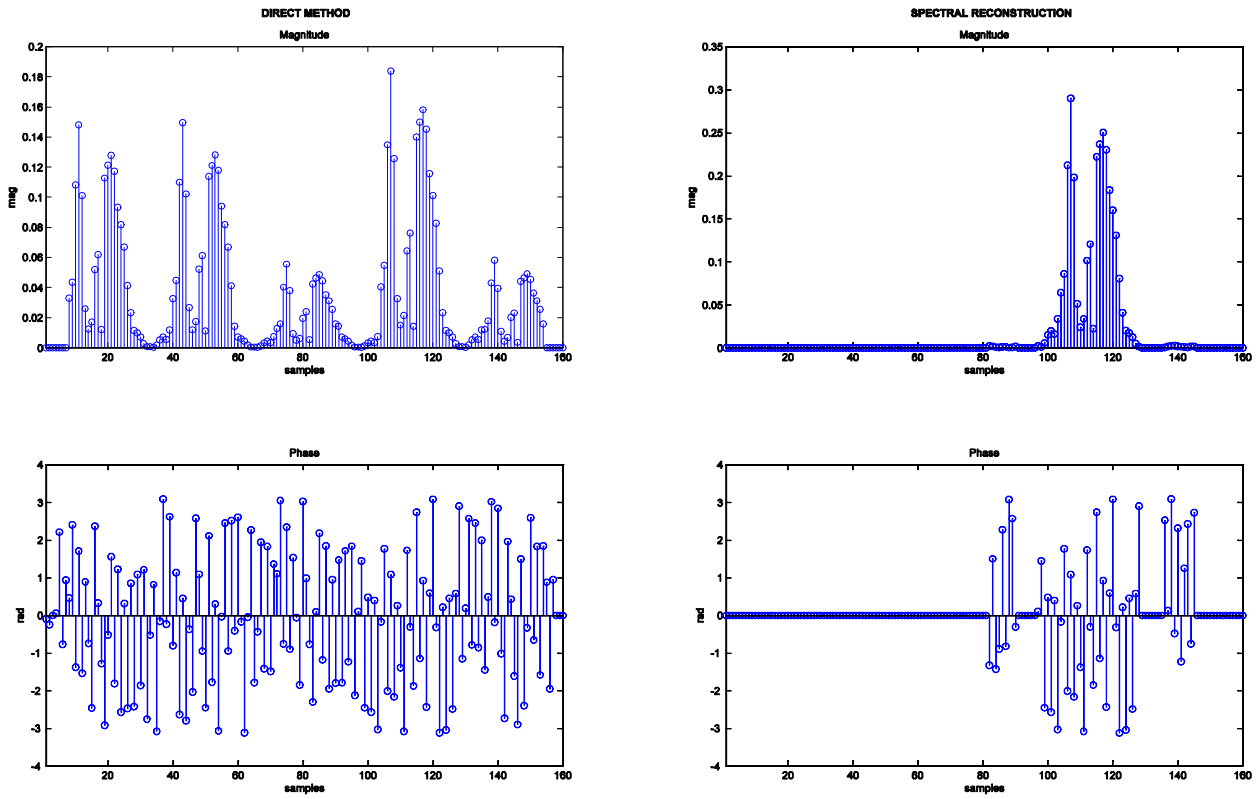

Fig. 2.4. Spectrum used to calculate powers and cross-correlation for the two methods under consideration. In the left side, the magnitude (up) and the phase (bottom) for the direct method are plotted. In the right side, the magnitude (up) and the phase (bottom) for the spectral reconstruction method are plotted. The results are very similar for both methods.

2.2.4. *Clutter Filtering Procedure*

In equation (2.3), **V** is the spectrum of the derived time series, and **E** is the unknown spectrum we are trying to recover. In other words, the vector **V** is the spectrum of the staggered PRT sequence obtained after converting the time series into a uniform sequence by inserting zeros in places of "missing samples", or the spectrum after convolving **E** with the code spectrum. Here we assume that the weather signal and the ground clutter are present in the time series. To contain the spread of the clutter power around zero Doppler, we need to multiply the time series by the data window weights. It is assumed that the effects of the data window are included in the spectrum **V**. Now, if we examine the convolution matrix, **C**, we find that each row has only five

non-zero coefficients (for κ =2/3) spaced $M/2$ coefficients apart. For example, with $M = 64$ (M_x = 160), of the 160 coefficients of DFT$\{c\}$ = [C_1, C_2, C_3, …, C_{160}] only C_1, C_{33}, C_{65}, C_{97}, and C_{128} are non-zero. In terms of these DFT coefficients the convolution matrix will have its first row as [C_1, $C1_{60}$, C_{159}, C_{158}, …, C_2], the second row as [C_2, C_1, C_{160}, C_{159}, C_{158}, …, C_3], which is the 1st row cyclically shifted to the right by one element, and so on. The first row has non-zero coefficients at column numbers 1, 33, 65, 97, and 129, and the DFT coefficients of the code sequence in these positions are C_1, C_{129}, C_{97}, C_{65}, and C_{33}. In the second row these same coefficients would shift to columns 2, 34, 66, 98, 130. Thus, after the convolution, the first and second elements V_1 and V_2 of the matrix **V** would be a weighted sum of the elements given by

$$V_1 = C_1 E_1 + C_{129} E_{33} + C_{97} E_{65} + C_{65} E_{97} + C_{33} E_{129}, \text{ and} \tag{2.8}$$

$$V_2 = C_1 E_2 + C_{129} E_{34} + C_{97} E_{66} + C_{65} E_{98} + C_{33} E_{130}.$$

Similarly, we can write equations for all 160 elements. Since each row of **C** is obtained by cyclically shifting the elements of the previous row to the right; all the coefficients are the same in the first 32 equations. For the next 32 equations, the coefficients would be shifted to the right by one, i.e., C_{33}, C_1, C_{129}, C_{97}, and C_{65}. Similarly, for every 32 equations, the coefficients are shifted to the right by one, and there are five such sets. Therefore, we can rearrange the convolution matrix as a 5-by-5 matrix $\mathbf{C_r}$, and **E** and **V** are rearranged row-wise as 5-by-32 matrices, $\mathbf{E_r}$ and $\mathbf{V_r}$, respectively (e.g., the first row of $\mathbf{V_r}$ has V_1 to V_{32}, the second row V_{33} to V_{64}, etc.). Equation (2.3) then becomes

$$\mathbf{V_r} = \mathbf{C_r}\,\mathbf{E_r}, \tag{2.9}$$

where the subscript ‘r’ represents a re-arranged matrix. $\mathbf{C_r}$ can be obtained from **C** by first deleting all rows containing zero in the *first* column of **C**, and then deleting all columns containing zero in the *first* row, which reduces it to a 5-by-5 matrix. (Note: The five non-zero spectral coefficients of **C** can also be obtained from a code vector of length 5, [10100], taking its DFT, and normalizing the power in the spectrum.) The matrix $\mathbf{C_r}$ is also singular (its rank is 2), and its columns are normalized such that each column is a unit vector (row vectors are normalized automatically).

Therefore, the 160 coefficients of the spectra are arranged row-wise into 5-by-32 matrices. Each column of $\mathbf{V_r}$ represents one of the 32 independent equations. The first column of $\mathbf{V_r}$ is related to the first column of $\mathbf{E_r}$ via the transformation matrix $\mathbf{C_r}$, the second column of $\mathbf{V_r}$ is related to the second column of $\mathbf{E_r}$ and so on. Clutter contamination is in the first few and last few coefficients of **E**, and the signal is centered on its mean velocity. After rearrangement, clutter contamination is in the first few coefficients in the first row and last coefficients in the last row of $\mathbf{E_r}$. If the narrow spectrum criterion is satisfied, the signal coefficients are spread, at most, over two rows. Therefore, in each column of $\mathbf{E_r}$, at most two elements are non-zero. After the transformation via the matrix $\mathbf{C_r}$, powers in these two coefficients spread to all the elements of each column of $\mathbf{V_r}$. The clutter and the weather signal have five weighted replicas in the **V** spectrum because of the convolution with the code spectrum which has only five non-zero coefficients. The clutter will be in the first coefficients of the first few columns and in the last coefficients of the last few columns. Figure 2.5 attempts to clarify these concepts by showing the magnitude of an extended spectrum.

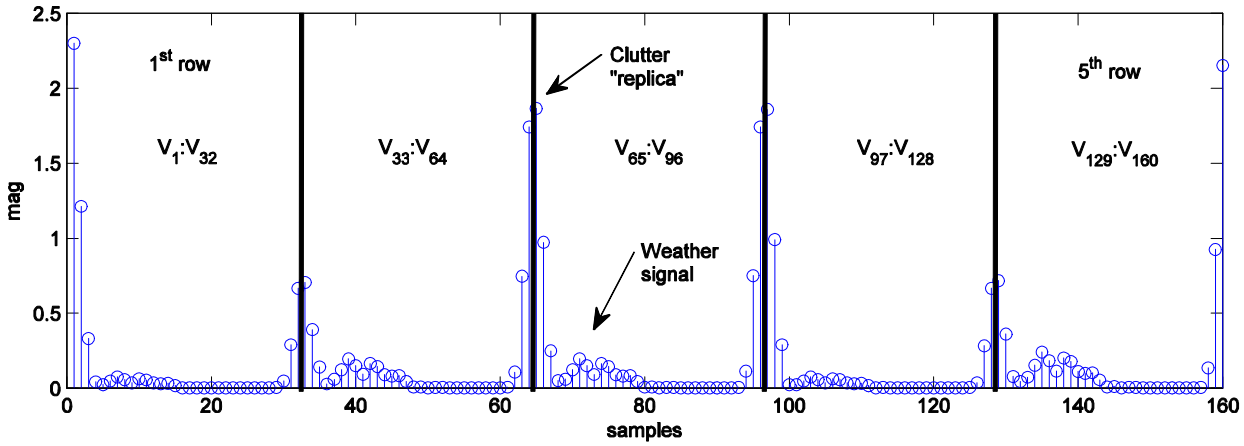

Fig. 2.5. **V** and $\mathbf{V_r}$ in the extended spectrum.

Let us take the equation corresponding to the first column of $\mathbf{V_r}$ to demonstrate the clutter filtering procedure:

$$\begin{bmatrix} V_1 \\ V_{33} \\ V_{65} \\ V_{97} \\ V_{129} \end{bmatrix} = \begin{bmatrix} C_1 & C_{129} & C_{97} & C_{65} & C_{33} \\ C_{33} & C_1 & C_{129} & C_{97} & C_{65} \\ C_{65} & C_{33} & C_1 & C_{129} & C_{97} \\ C_{97} & C_{65} & C_{33} & C_1 & C_{129} \\ C_{129} & C_{97} & C_{65} & C_{33} & C_1 \end{bmatrix} \begin{bmatrix} E_1 \\ E_{33} \\ E_{65} \\ E_{97} \\ E_{129} \end{bmatrix}. \tag{2.10}$$

For simplicity, we write the transformation matrix in terms of its column vectors:

$$\begin{bmatrix} V_1 \\ V_{33} \\ V_{65} \\ V_{97} \\ V_{129} \end{bmatrix} = \begin{bmatrix} \mathbf{C}_1 & \mathbf{C}_2 & \mathbf{C}_3 & \mathbf{C}_4 & \mathbf{C}_5 \end{bmatrix} \begin{bmatrix} E_1 \\ E_{33} \\ E_{65} \\ E_{97} \\ E_{129} \end{bmatrix} \tag{2.11}$$

If we assume that the signal coefficient is E_{97}, we can reduce equation (2.11) to

$$\mathbf{V_1} = \mathbf{C_1}E_1 + \mathbf{C_4}E_4, \tag{2.12}$$

where vector $\mathbf{V_1}$ on the left hand side is the first column of $\mathbf{V_r}$. To filter the clutter we just have to take the component of $\mathbf{V_1}$ along the direction $\mathbf{C_1}$ and substract it from $\mathbf{V_1}$. This is accomplished by taking the inner product between $\mathbf{C_1}$ and $\mathbf{V_1}$, multiplying this by $\mathbf{C_1}$ and then substracting it from $\mathbf{V_1}$:

$$\mathbf{V_{f1}} = \mathbf{V_1} - (\mathbf{C_1}^{*T}\,\mathbf{V_1})\,\mathbf{C_1}. \tag{2.13}$$

In other words, the main replica around zero and the projected clutter around $\pm 2v_a/5$ and $\pm 4v_a/5$ are removed.

Since the clutter is present in the first few and the last few columns of $\mathbf{E_r}$, we apply this procedure only to those columns in which the clutter is present. In the last columns the clutter coefficient are in the last row, hence, we replace the vector $\mathbf{C_1}$ by $\mathbf{C_5}$:

$$\mathbf{V_{f32}} = \mathbf{V_{32}} - (\mathbf{C_5}^{*T}\,\mathbf{V_{32}})\,\mathbf{C_5}. \tag{2.14}$$

In terms of the DFT coefficients, the ground clutter filtering procedure is applied to the first q columns and the last (q-1) columns (where the clutter filter width, $n_c = 2q - 1$). n_c has to be an odd number in order to maintain symmetry around zero Doppler (or the 1st coefficient). Therefore, we select first q columns and last (q-1) columns and remove the clutter by applying (2.13) or (2.14). This complete operation can be written in matrix notation as

$$\mathbf{V_f} = \mathbf{V_r} - \mathbf{C_{f1}}\,\mathbf{V_r}\,\mathbf{I_{f1}} - \mathbf{C_{f1}}\,\mathbf{V_r}\,\mathbf{I_{f2}}, \tag{2.15}$$

where $\mathbf{C_{f1}}$ and $\mathbf{C_{f1}}$ are the clutter filter matrices and $\mathbf{I_{f1}}$ and $\mathbf{I_{f2}}$ are matrices that select the columns to be filtered:

$$\mathbf{C_{f1}} = \mathbf{C_1}\,\mathbf{C_1}^{*\mathbf{T}}, \text{ and} \tag{2.16}$$

$$\mathbf{C_{f2}} = \mathbf{C_5}\,\mathbf{C_5}^{*\mathbf{T}}. \tag{2.17}$$

The matrix $\mathbf{I_{f1}}$ is an M/2-by-M/2 diagonal matrix with diagonal elements equal to 1 for the first q elements and 0 for the rest. Similarly, the matrix $\mathbf{I_{f2}}$ is an M/2-by-M/2 diagonal matrix with last (q-1) elements unity and the rest zeros.

Finally the matrix $\mathbf{V_f}$ is rearranged into a N-by-1 vector $\mathbf{V_{df}}$. This vector represents the filtered extended spectrum. Fig. 2.6 shows vector $\mathbf{V}$ before and after clutter filtering. It can be seen how the first and the last coefficients are removed, but it is only the projections that are removed in the replicas.

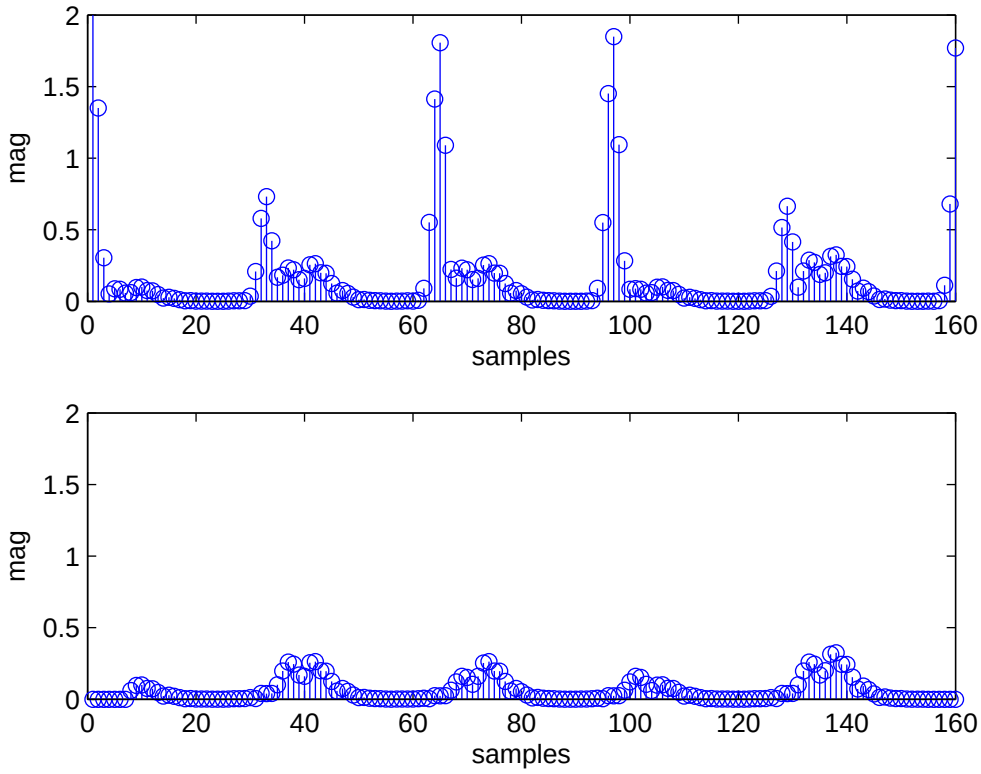

Fig. 2.6. Vector **V** before (up) and after (down) clutter filtering.

This procedure is applied for both channels, and once the clutter has been filtered, the powers and cross-correlation can be computed from vector $\mathbf{V_{df}}$ according to equations (2.5), (2.6) and (2.7). After this, the final steps of the clutter filter remain unchanged. That is, after the computation of the powers and cross-correlation **for the polarimetric variables**, the magnitude deconvolution is applied to the H-channel data, and the rearranged vector is used to retrieve the values for the auto-correlations and power. More details about this procedure are explained in previous reports.

2.2.5. *Notchwidth Determination*

Given that we have two different time series, one for each polarization channel, the notchwidth determination is an important issue. For single polarization, the value for n_c is determined by the GMAP algorithm. The input to GMAP is one-fifth of the spectrum around zero velocity; i.e., containing the first and the last coefficients. We considered three different possibilities:

1. Use the H channel as a "master" channel. The input to GMAP will be one-fifth of the H-channel spectrum.
2. Consider H and V channels independently, each with its own q value. The clutter filtering will be performed independently for each channel.
3. Use the channel with larger clutter-to-signal ratio (CSR) as a "master" channel. Retrieve q values from GMAP for the H and V channels and then choose the maximum value to filter both spectra in the same manner.

Simulations were employed to find the optimum approach. Fig. 2.7 shows the bias and the standard deviation for the three polarimetric variables for a high CSR versus Z_{DR}. We chose Z_{DR} as the independent variable because we found that these results were highly influenced by this variable. As we can see, the three methods offer similar results. Since the CSR was fixed for the H channel, negative Z_{DR} produce higher errors and standard deviations. A negative Z_{DR} means that the CSR for the V channel is higher than the CSR for the H channel. However, if we choose a low CSR, results are completely different for each approach for negative Z_{DR}, Fig. 2.8 shows that. With these results in mind, the third approach was chosen. The notchwidth will be the same for both channels, and it will be the maximum between them as computed independently. If we choose the first approach (the H channel as the master channel) and the Z_{DR} is negative, we are underestimating the amount of clutter in the V channel. If we choose the second approach, the q

values can be completely different and may lead to biased computations since we can have different number of coefficients filtered for each channel.

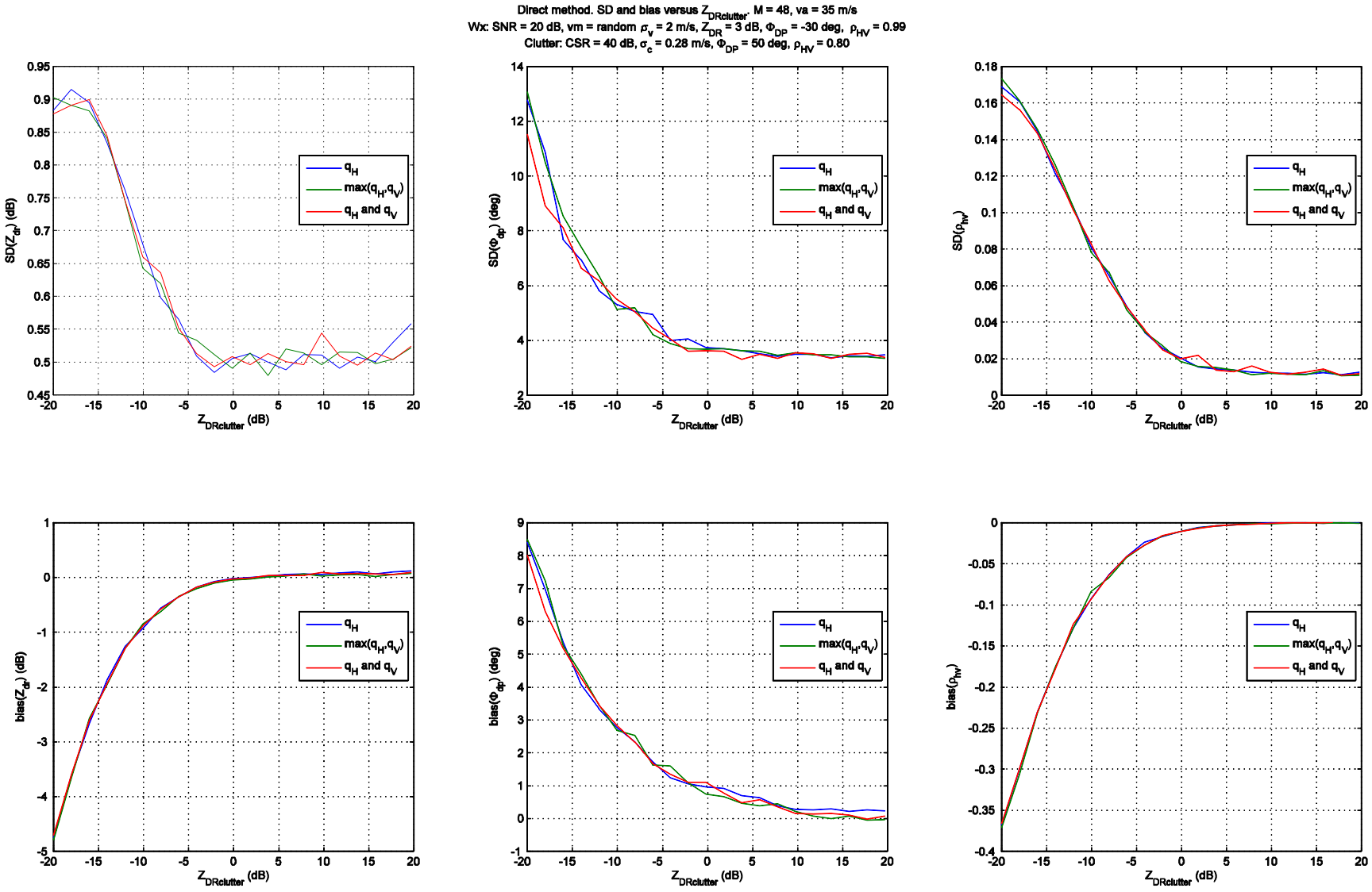

Fig. 2.7. Bias and standard deviation for Z_{DR}, Φ_{DR} and ρ_{HV} varying Z_{DR} for a fixed CSR_H of 40 dB comparing three notchwidth determination approaches.

Since only the H-channel is used for the spectral moment computations, the q retrieved with H channel spectrum will be used for this purpose. That is, two different q values can be considered. Fig. 2.9 shows the procedure.

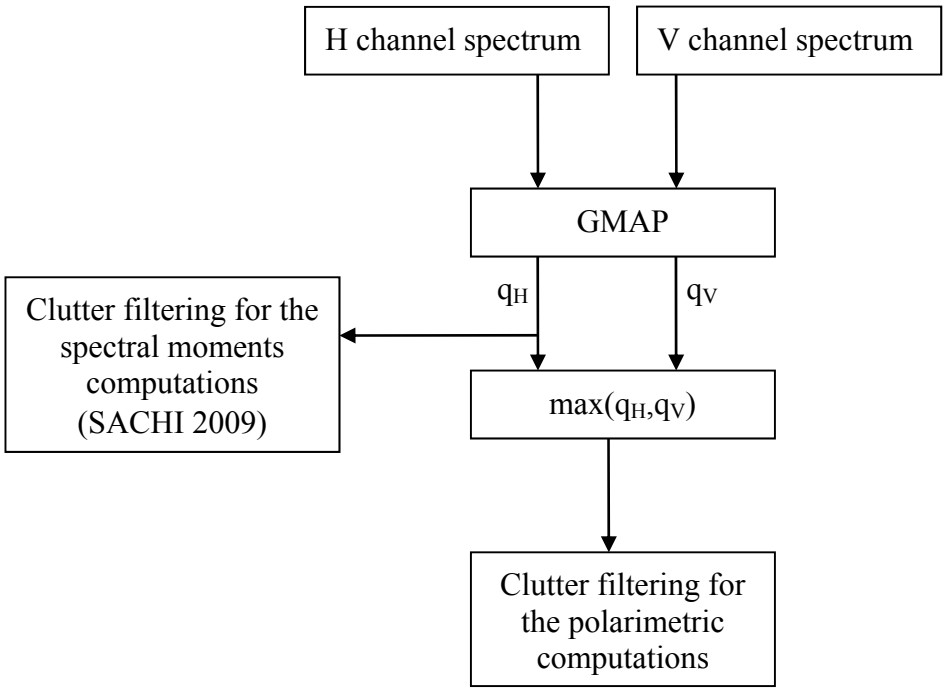

Fig. 2.9. Notchwidth determination for dual polarization SPRT ground clutter filter

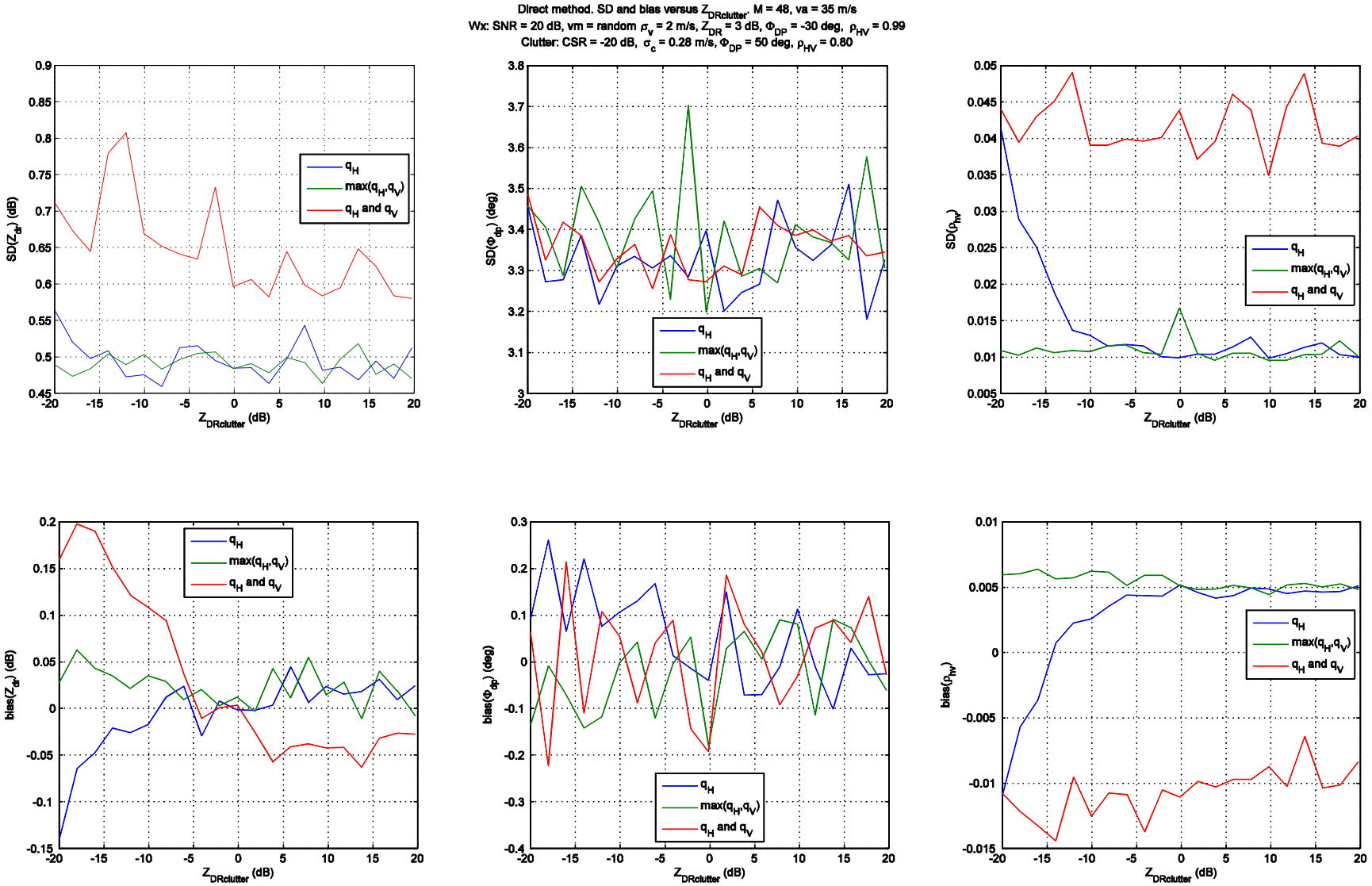

Fig. 2.8. Bias and standard deviation for Z_{DR}, Φ_{DR} and ρ_{HV} varying Z_{DR} for a fixed CSR_H of -20 dB comparing three notchwidth determination approaches.

2.2.6. *Dual-Polarization Time-Series Simulation*

Simulations were performed to test the dual polarization staggered PRT ground clutter filter method. The bias and the standard deviation for the polarimetric variables are plotted for a variety of situations. The default parameters are detailed below. Since this algorithm update only affects polarimetric variable computations, they were chosen as the independent variables in the simulations. One of the simulations is used to quantify the clutter filter suppression, and the rest illustrate the effects of varying the polarimetric properties of the input signals. In these cases, several CSR were used, as well as a no-clutter case (i.e., CSR = -∞).

- Weather:
  - SNR_h = 20 dB, v = random in the extended Nyquist interval, w = 2 m/s
  - Z_{DR} = 3 dB, Φ_{DP} = -30 deg, ρ_{HV} = 0.99
- Clutter:
  - CSR_h = 40 dB, v = 0, w = 0.28 m/s,
  - Z_{DR} = -5 dB, Φ_{DP} = 50 deg, ρ_{HV} = 0.8
- v_a = 35 m/s, M = 48
- 1000 realizations

Note that these parameters correspond to a worst case scenario. For the weather signal, we chose typical testing parameters for SNR and spectrum width. The velocity was chosen randomly in every realization in the range from $-v_a$ to v_a. The positive value of differential reflectivity means that the SNR is higher for the H channel than for the V channel, since the noise in both channels is assumed to be the same. For the clutter, we considered a high CSR and the typical values for velocity and spectrum width. We also considered a different value for the differential phase, since this difference in Φ_{DP} for weather and clutter can cause a higher bias. For differential reflectivity and correlation coefficient we chose a worst case based on Fig. 2.10. It is important

to realize that a positive Z_{DR} for the weather together with a negative Z_{DR} for the clutter mean that the CSR for the vertical channel is higher than for the horizontal channel. That is, in the simulations, the CSR_v is much higher than 40 dB (CSR_h); this will be evident in the examples. The maximum unambiguous velocity and the number of samples are representative of an operational scanning strategy.

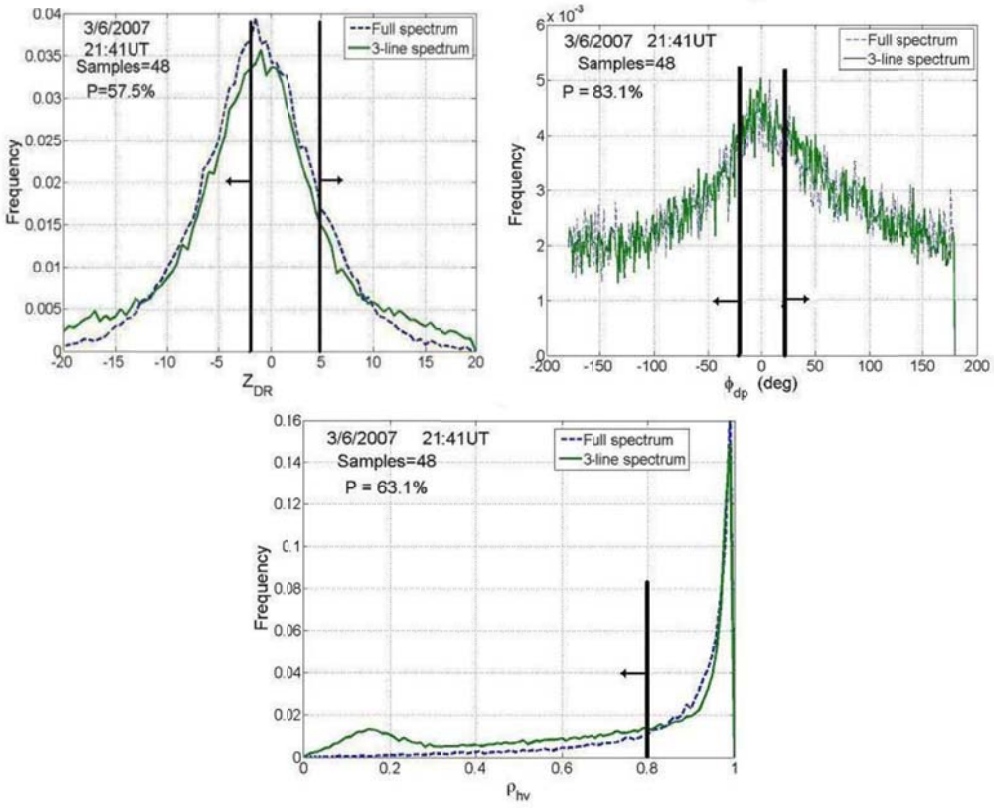

Fig. 2.10. Polarimetric characteristics of ground clutter. From Melnikov and Zrnic (2006)

2.2.6.1. Ground clutter filter suppression

Fig. 2.11 shows the ground clutter filter suppression. Bias and standard deviation are plotted versus CSR_h for several spectrum widths. The results show a good ground clutter filter behavior for CSR up to 40 dB. The bias and standard deviation are higher for w = 1 m/s because, for certain velocities, the weather signal can be almost completely removed by the filter. For wider

spectrum widths, the results are as expected. Given a GCF suppression of 40 dB, the error in Z_{DR} will be less than 0.6 dB, 6 degrees for Φ_{DP}, and 0.06 for ρ_{HV}.

2.2.6.2. Ground clutter filter performance as a function of clutter Z_{DR}

Fig. 2.12 shows the ground clutter filter performance versus the clutter differential reflectivity for several CSR_h. The results agree with the expected GCF suppression. Only CSR_h= 40 dB causes a high bias and standard deviation for negative clutter Z_{DR}, since this really represents a higher value for CSR_v. For instance, consider the case where CSR_h= 40 dB, Z_{DRc} = -3 dB (subscript 'c' indicates clutter) and Z_{DR} = 3 dB (no subscript indicates weather). The CSR_v can be written as a function of CSR_h as follows:

$$CSR_h = C_h/S_h,\ CSR_v = C_v/S_v$$

$$Z_{DR} = S_h/S_v = 3\ \text{dB} \Rightarrow S_v = \tfrac{1}{2}S_h$$

$$Z_{DRc} = C_h/C_v = -3\ \text{dB} \Rightarrow C_v = 2C_h$$

$$CSR_v = C_v/S_v = 2C_h/\tfrac{1}{2}S_h = 4CSR_h.$$

That is, CSR_v would be 6 dB higher than CSR_h. This explains the exponential behavior of the purple curve in Fig. 2.12, which is exactly the same behavior we see in Fig. 2.11 for the GCF suppression. For lower CSR values, the bias is around zero in every case, and the standard deviation is very close to the no-clutter case.

2.2.6.3. Ground clutter filter performance as a function of clutter Φ_{DP}

Fig. 2.13 shows the performance of the filter as a function the clutter Φ_{DP}. In these simulations we maintained a fixed Φ_{DP} for the weather and we varied the Φ_{DP} for the clutter. The difference between the two differential phases is what causes the high bias and standard deviation for high CSR. The bias of differential reflectivity is small. The Φ_{DP} difference between weather and clutter has little influence on its computation, but a strong effect on differential phase and cross-correlation coefficient. For lower CSR, the results are close to the no-clutter case.

2.2.6.4. Ground clutter filter performance as a function of clutter ρ_{HV}

Fig. 2.14 depicts the performance of the filter versus the clutter cross-correlation coefficient. The results agree with the previous simulations for the standard case, since this independent value has little influence on the computation of the polarimetric variables for a CSR lower than 40 dB. Hence, we can conclude for each variable:

- **Z_{DR}:** There is no bias in the Z_{DR} computation except for CSR = 40 dB. The standard deviation is well below 0.6 dB even for the worst CSR case.
- **Φ_{DP}:** The bias is zero for CSR < 40 dB. The standard deviation is only 3.5 degrees, not too far from the 3 degree standard deviation for the no-clutter case.
- **ρ_{HV}:** The bias is lower than 0.006 for CSR < 40 dB. The standard deviation is around 0.01, a very close value to the no-clutter case.

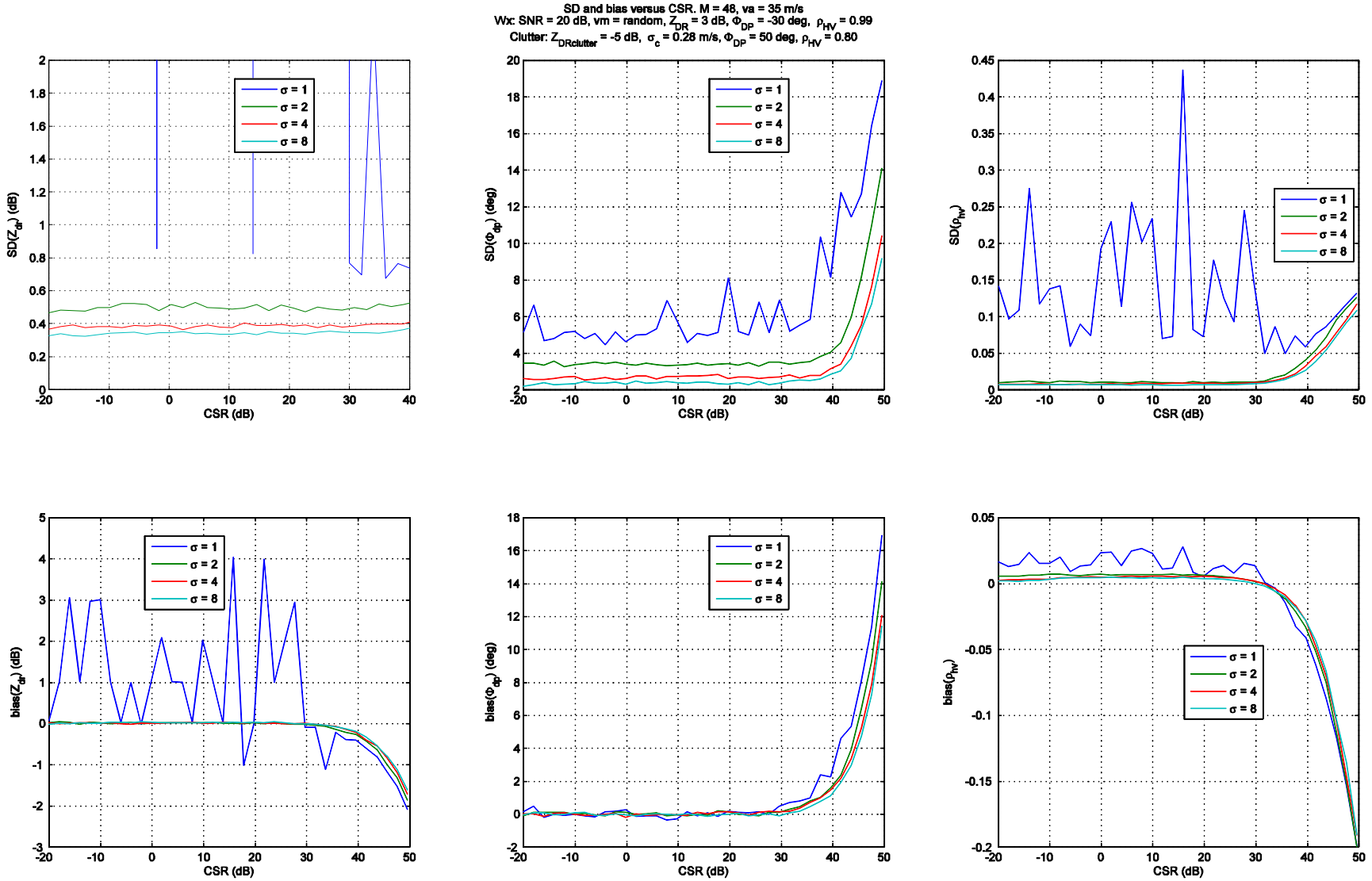

Fig. 2.11. GCF suppression.

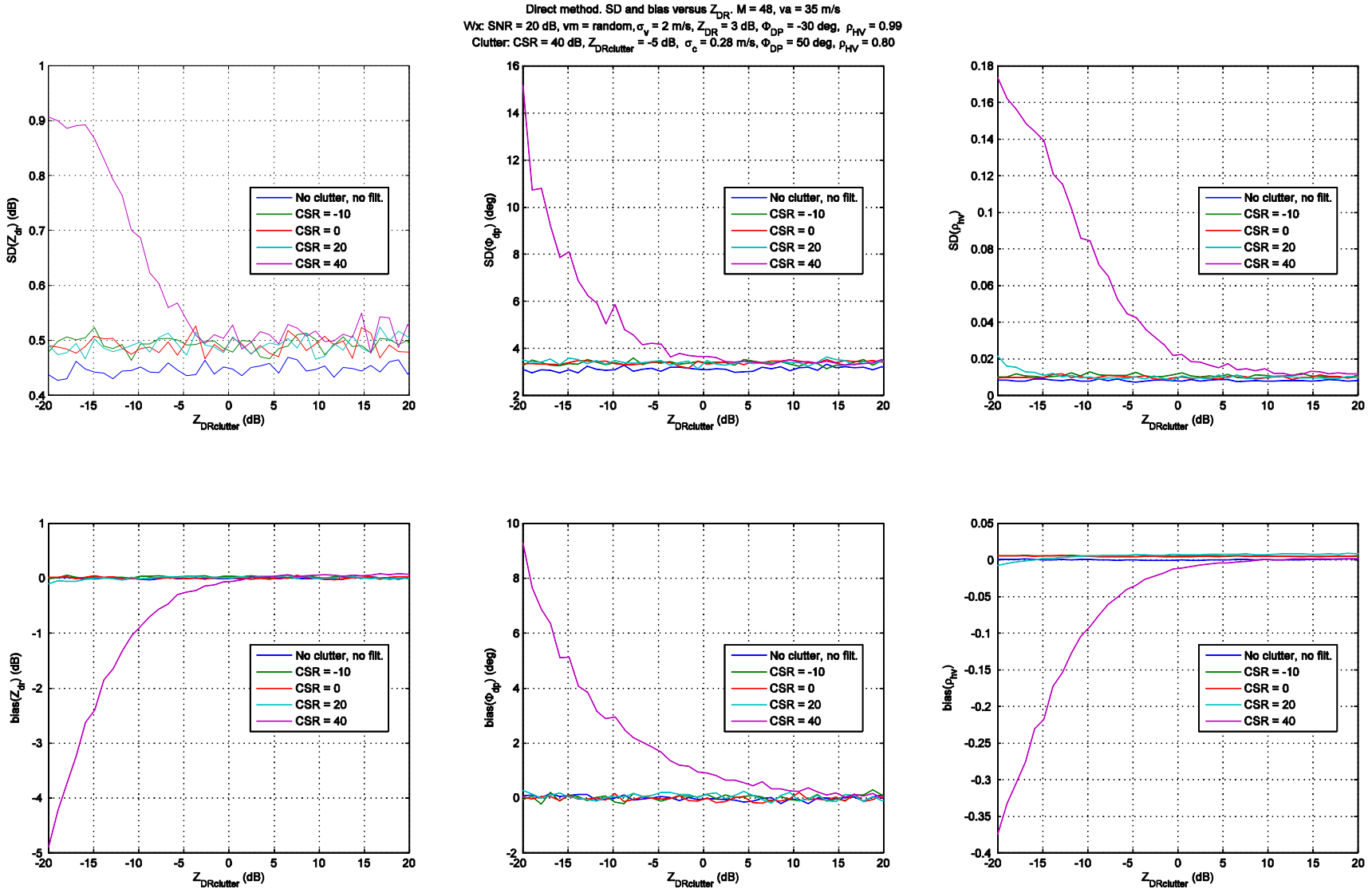

Fig. 2.12. GCF Performance vs. Clutter Z_{DR}

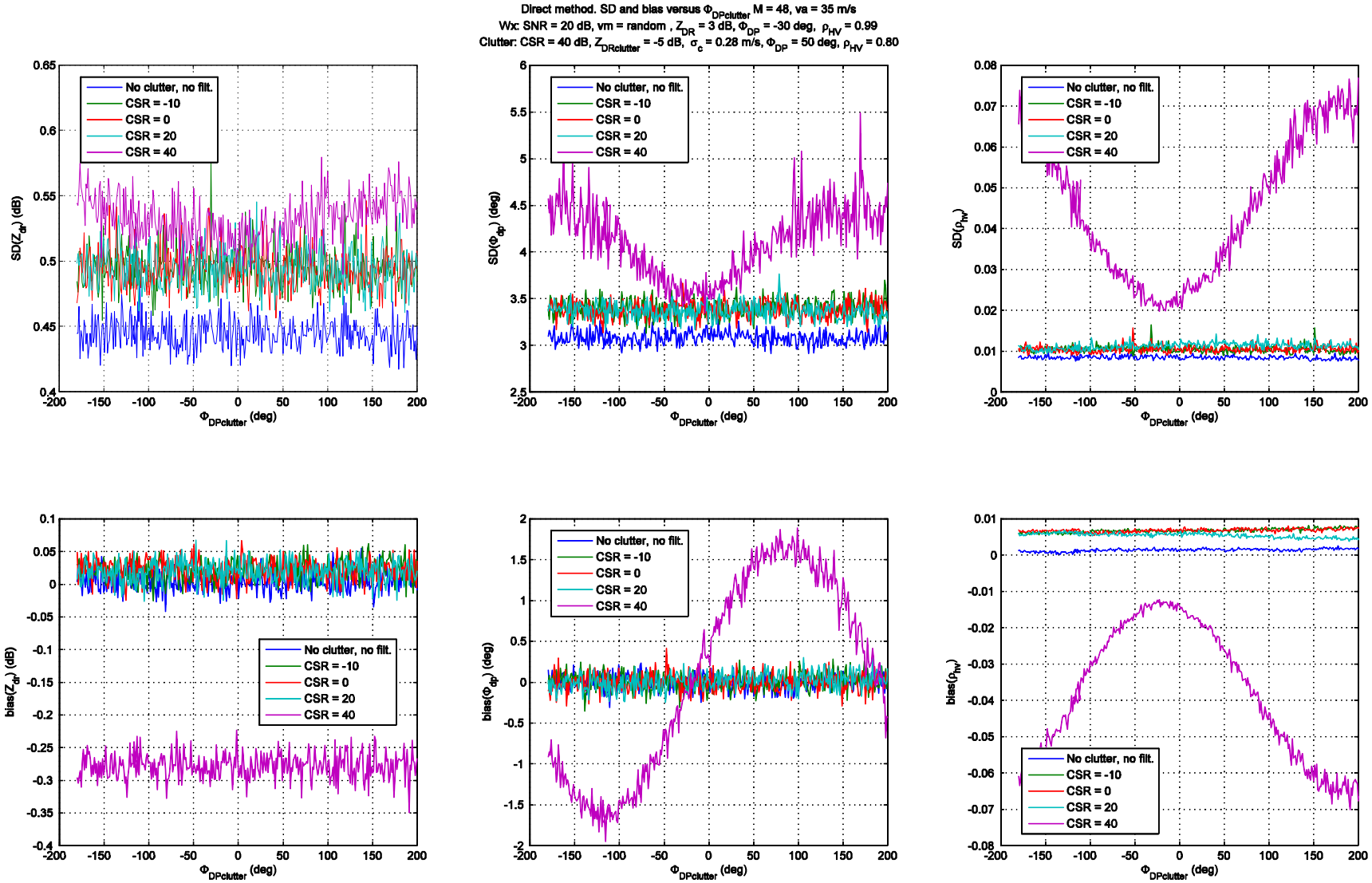

Fig. 2.13. GCF Performance vs. Clutter Φ_{DP}

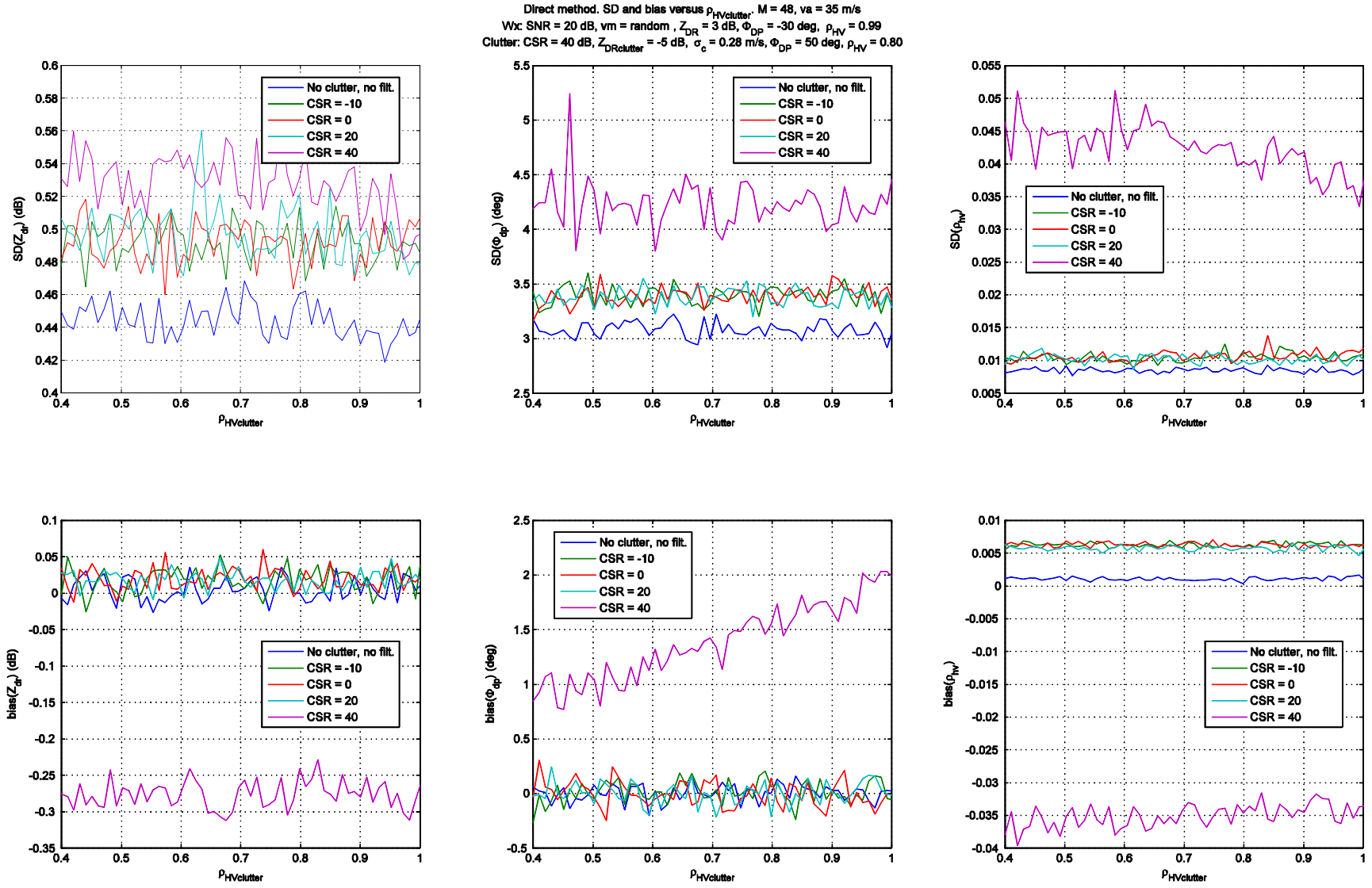

Fig. 2.14. GCF Performance vs. Clutter ρ_{HV}

2.3. Real Data Results

The proposed algorithm was tested on real data. We used a single-elevation scan of time series data recorded on March 4th, 2004 with the KOUN radar in Norman, OK. The main parameters are in the table below.

VCP 2048	
Elev. (deg)	2.45
AZ rate (deg/s)	16.30
Period (s)	22.08
Dwell time (ms)	61.4
Staggered ratio κ	2/3
M	20
T_1 (ms)	1.23
T_2 (ms)	1.84
r_{ar} (km)	276
r_{a1} (km)	184
v_a (m/s)	45.1

Figures 2.15 to 2.20 show the filtered and unfiltered PPIs for the spectral moments and the polarimetric variables. By visual inspection, it can be confirmed that the recommended dual-polarization SPRT algorithm fulfills the requirements. The polarimetric variables are calculated, the clutter is filtered, and the spectral moment computation is not harmed.

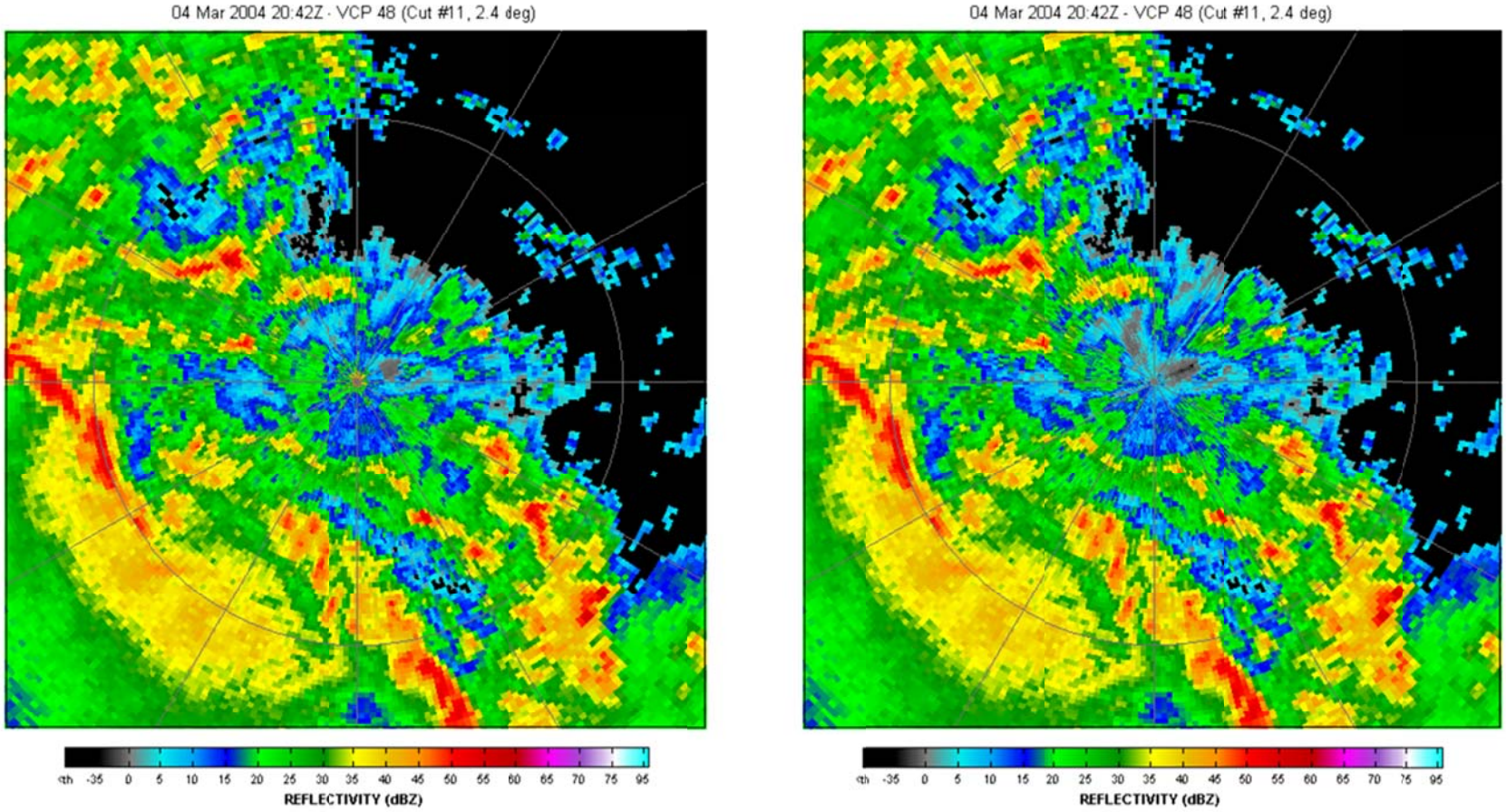

(a) (b)

Fig. 2.15. Unfiltered (a) and filtered (b) reflectivities.

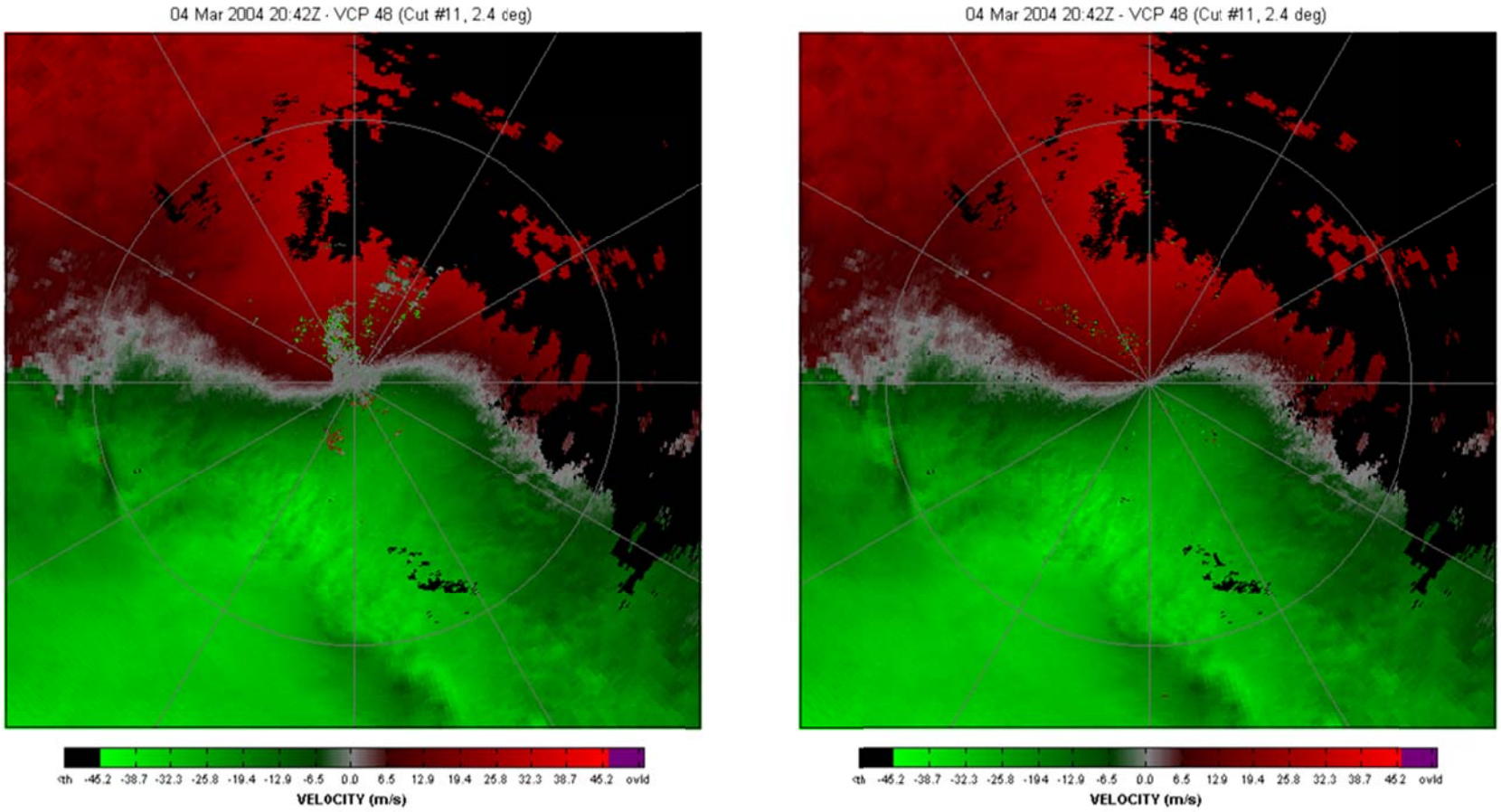

(a) (b)

Fig. 2.16. Unfiltered (a) and filtered (b) velocities.

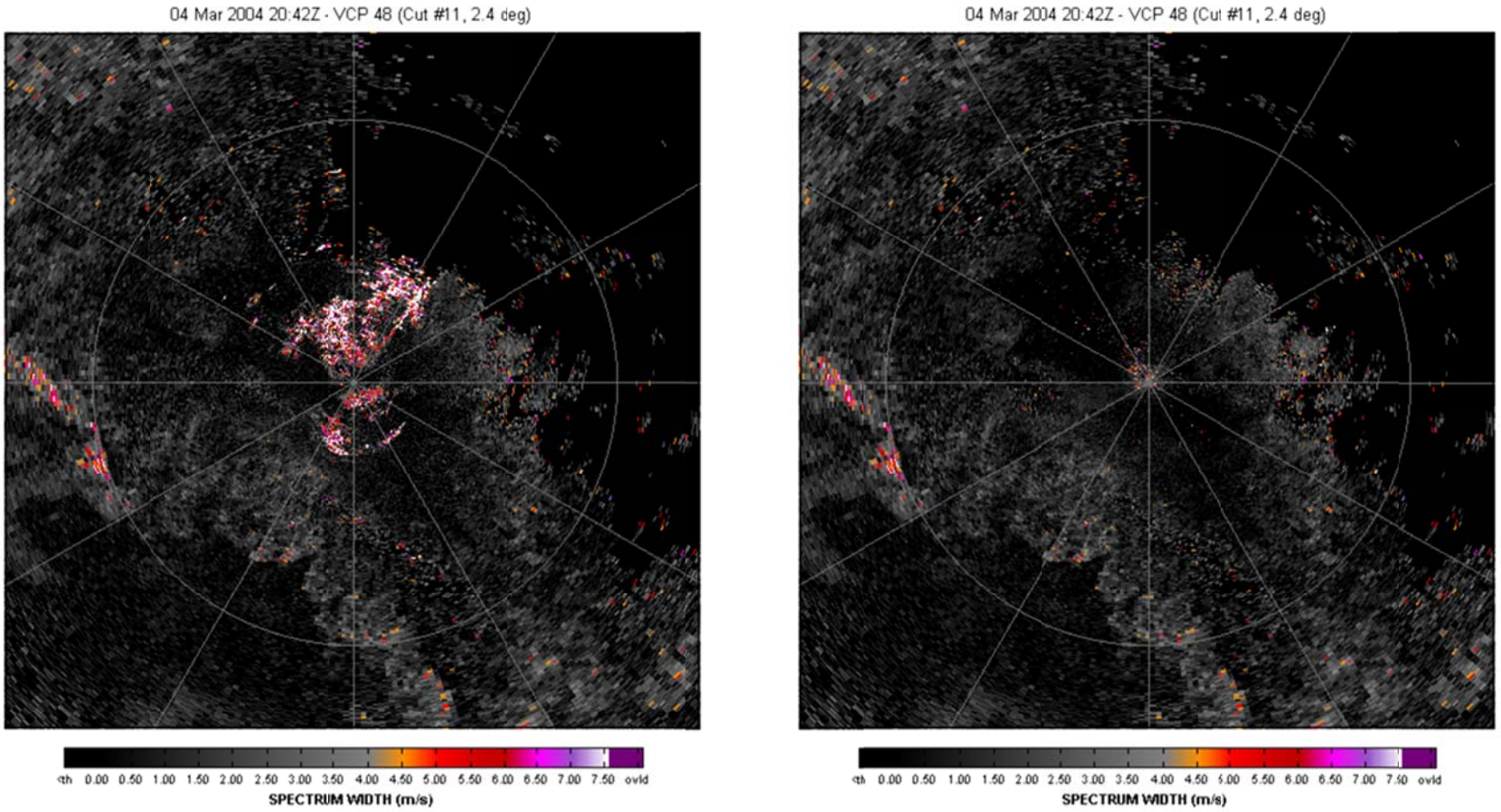

(a) (b)

Fig. 2.17. Unfiltered (a) and filtered (b) spectrum widths.

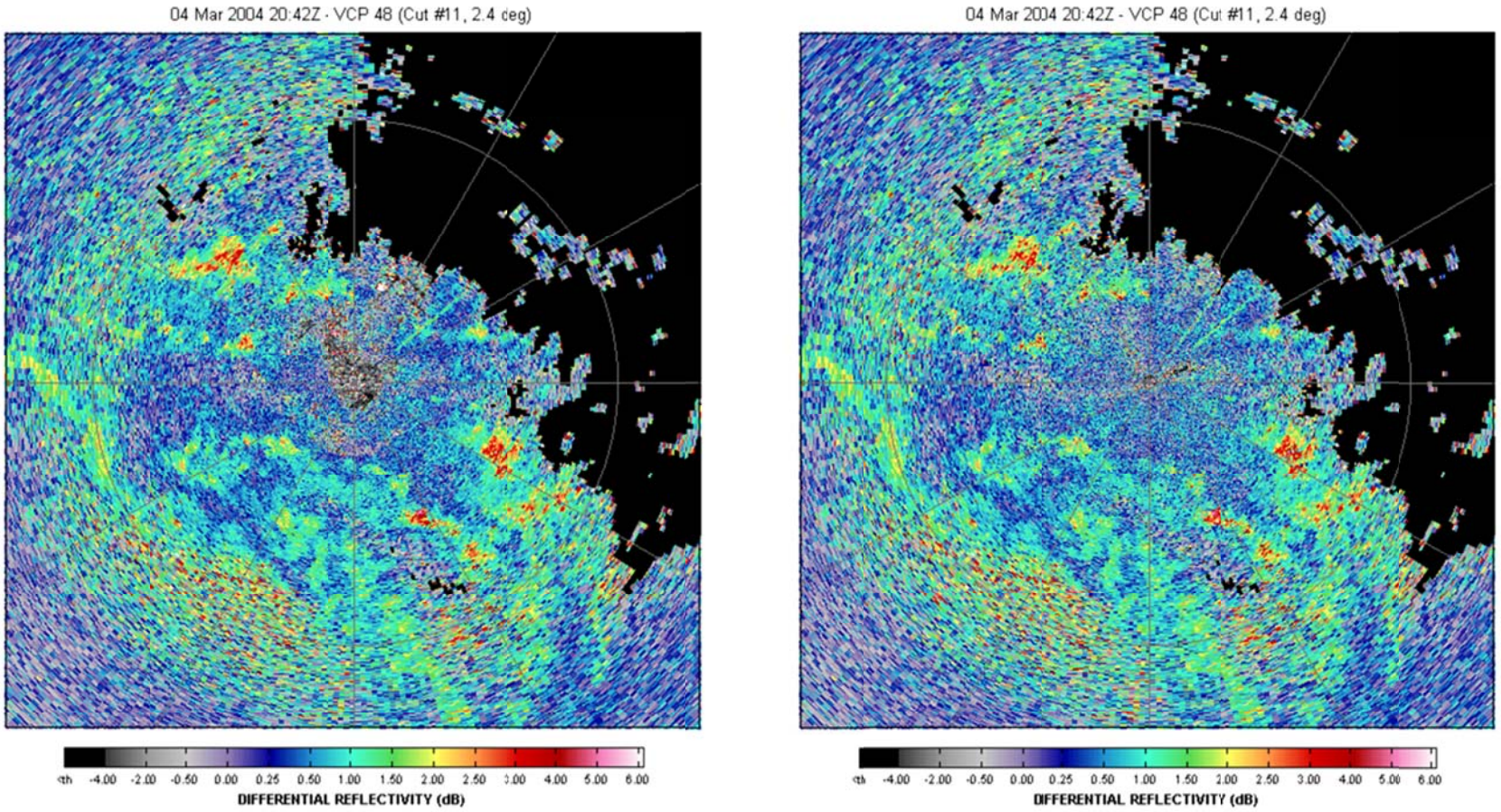

(a) (b)

Fig. 2.18. Unfiltered (a) and filtered (b) differential reflectivities.

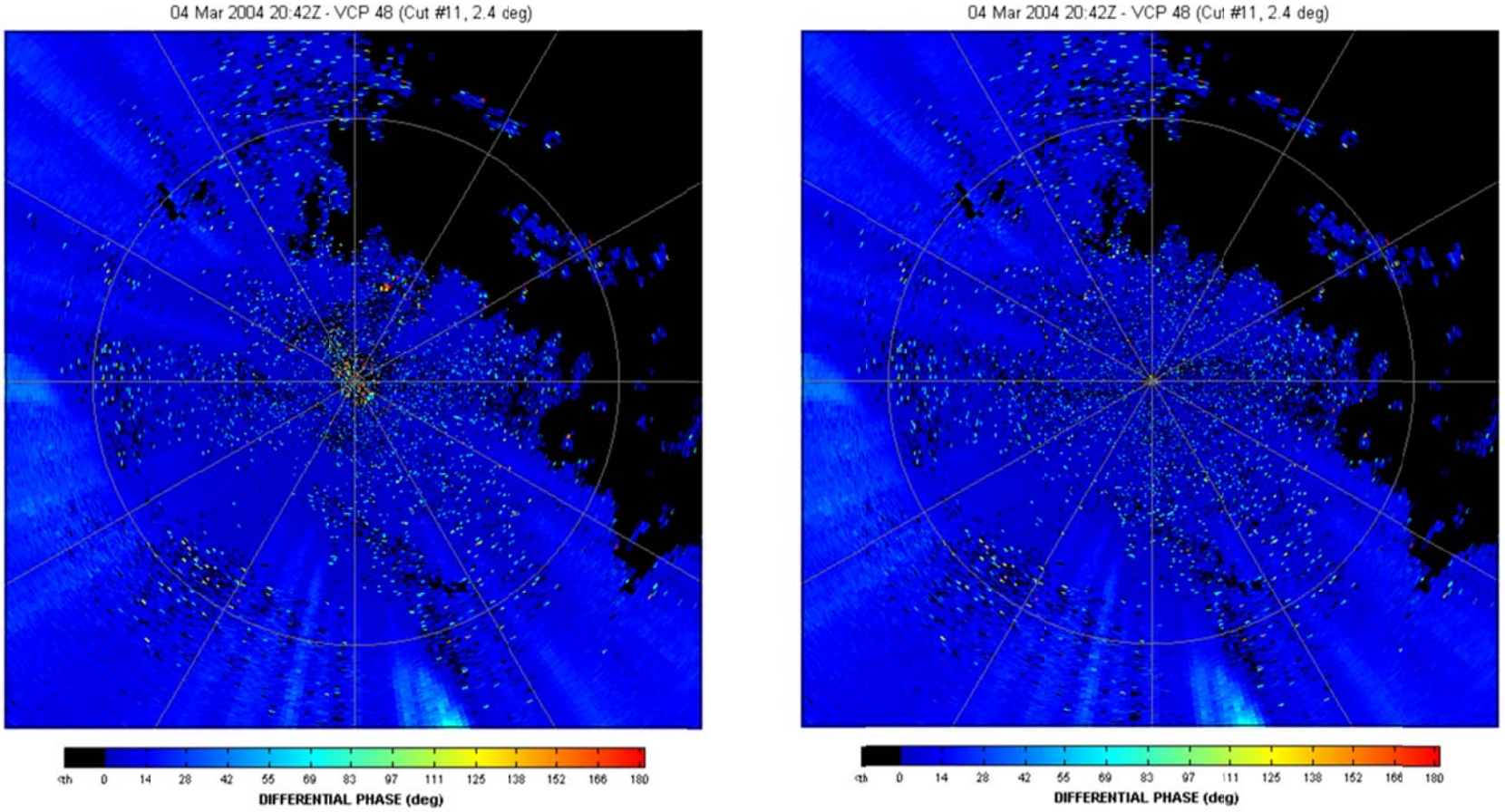

(a) (b)

Fig. 2.19. Unfiltered (a) and filtered (b) differential phases.

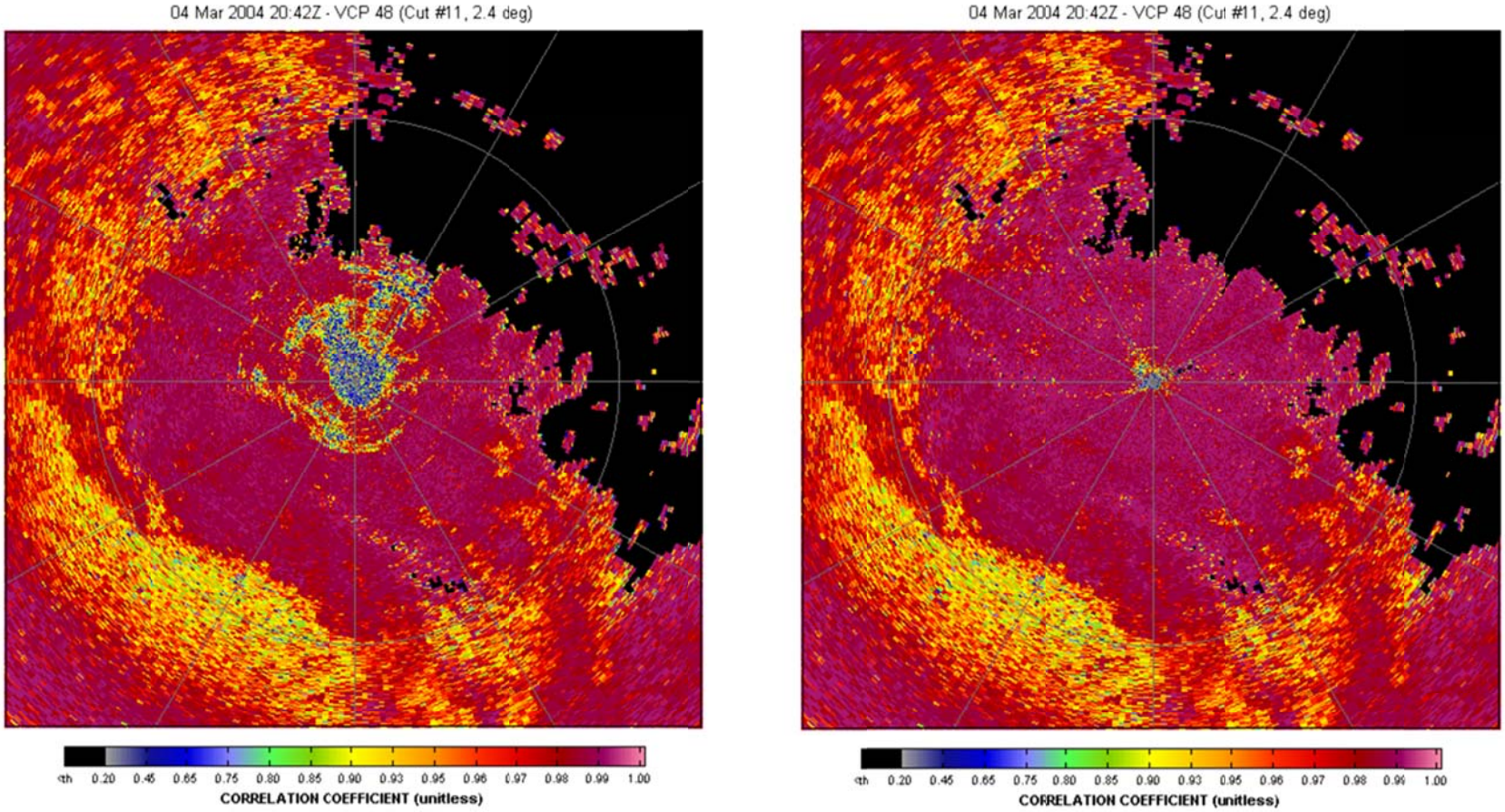

(a) (b)

Fig. 2.20. Unfiltered (a) and filtered (b) cross-correlation coefficients.

2.4. Data Window Effects: Some Observations

A higher noise in the real-data cross-correlation coefficient was perceived when we compared the filtered and unfiltered PPI images. Since the no-clutter simulations were also computed in the spectral domain, a brief study about this issue was performed. The reason for this is clear if we recall that the meteorological variable computations for SPRT in the time and the spectral domain differ considerably. The zero padding and the window result in higher standard deviation of the cross-correlation coefficient computation. In region II, a rectangular window would provide the same results than the computations in the time domain. But in regions I and III we are considering different sets of data: even or odd pulses in time and extended series in frequency. The cross-correlation coefficient is an extremely sensitive variable, and these slight differences in the power computations can lead to a noticeable change, see Fig. 2.21. However, this is only important for low SNR values, as it can be appreciated in Fig. 2.22, where the highest differences coincide with the lowest SNRs.

Additionally, we conducted simulations to analyze the probability of obtaining a cross-correlation coefficient higher than 1 for staggered PRT processing in the time and in the spectral domains and also for uniform PRT (UPRT). The results are shown in Fig. 2.23. These simulations employ the same set of default parameters of section 2.2.6. No clutter was added to the simulations. For the SPRT case, the cross-correlation coefficient is computed first from the powers and cross-correlation calculated from the unwindowed time samples. Second, the powers and cross-correlation are calculated from the extended spectra, using a standard Blackman window. The UPRT computations are the time domain with the same v_a (v_a = 35 m/s) and number of samples M_x (M_x = 120). As expected, the probability of $\rho_{HV} > 1$ increases for low

SNRs. For instance, given an SNR of 10 dB, the probability of obtaining $\rho_{HV} > 1$ is basically zero for UPRT processing, 0.38 for SPRT time-domain processing, and 0.51 for SPRT spectral processing. Fig. 2.24 shows the differences in standard deviation. For SNRs lower than 10 dB, this standard deviation can exceed 0.05 for SPRT spectral processing, which is a very high value for a variable as sensitive as the cross-correlation coefficient.

Note that these results are preliminary and further studies are warranted.

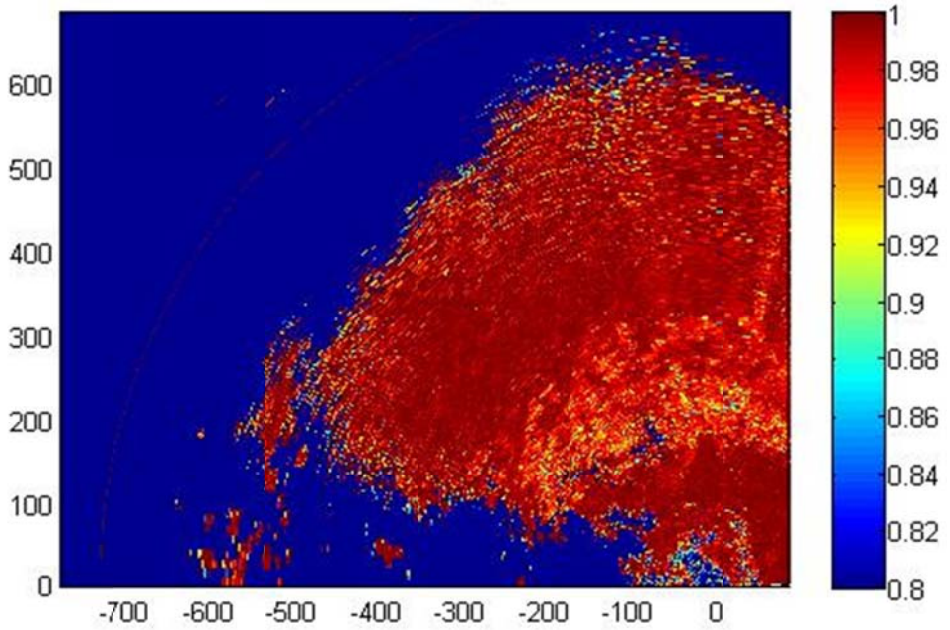

(a)

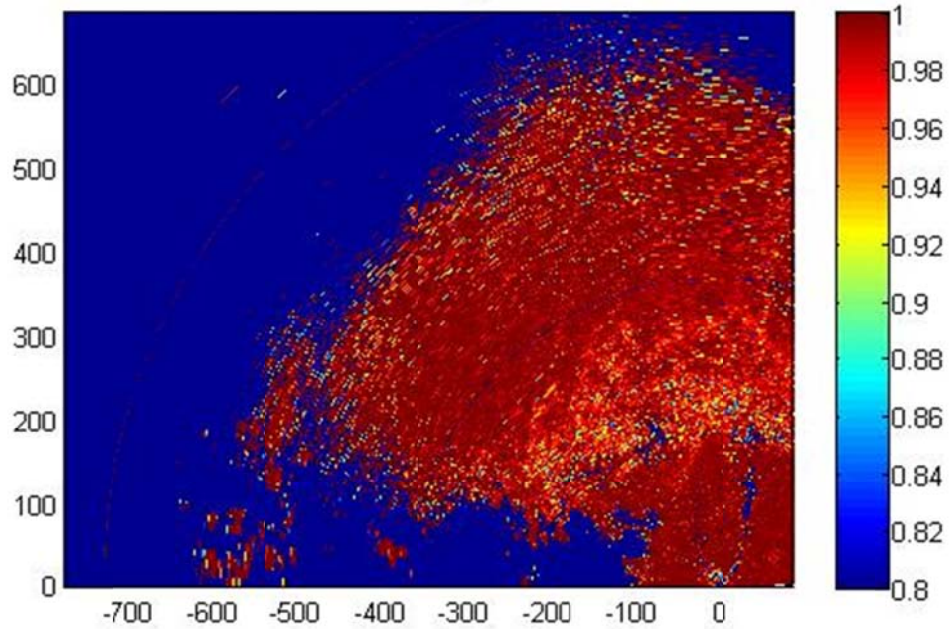

(b)

Fig. 2.21. Unfiltered (a) and filtered (b) cross-correlation coefficient.

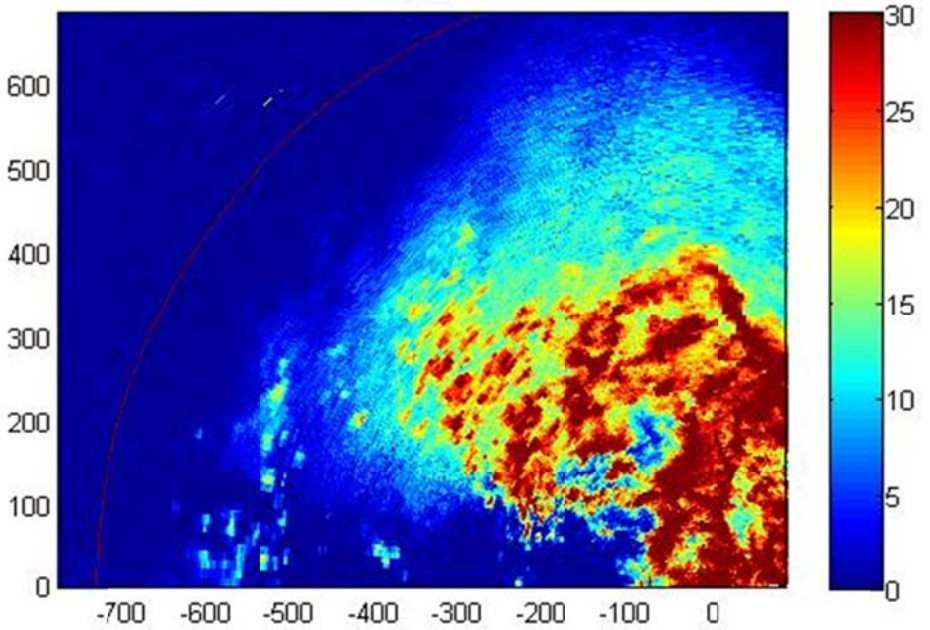

(a)

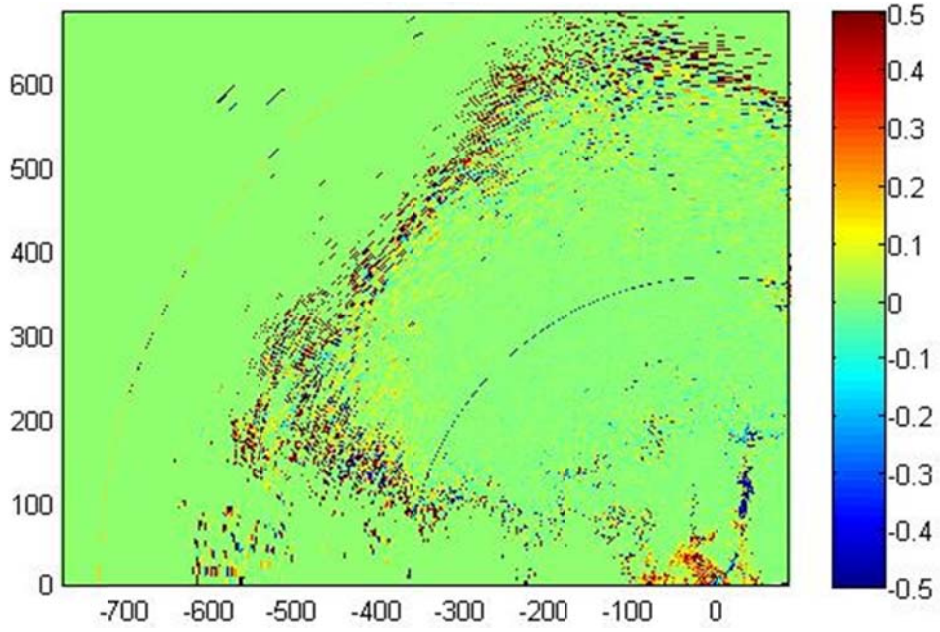

(b)

Fig. 2.22. SNR (a) and difference between filtered and unfiltered cross-correlation coefficient (b). Notice how the higher difference areas match with the lower SNRs.

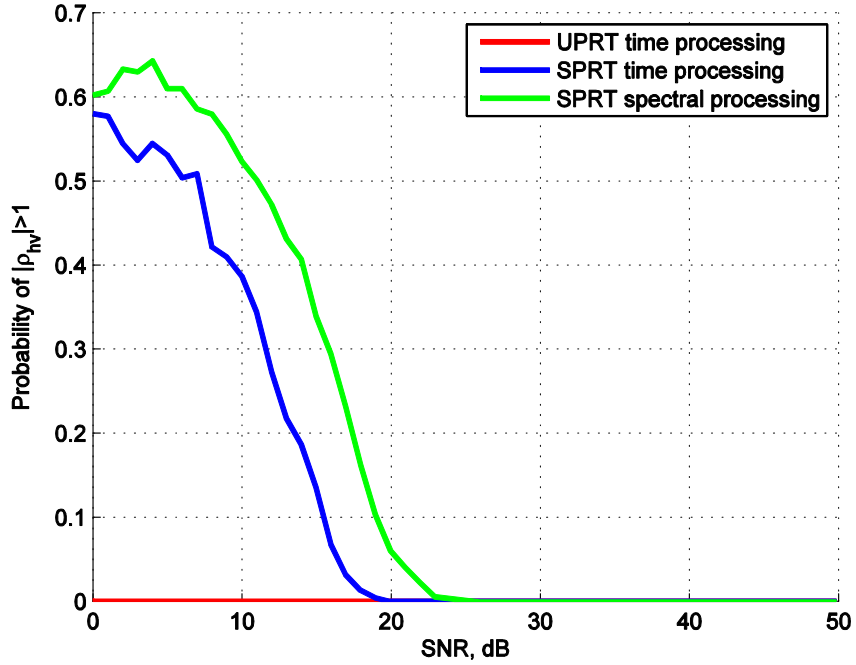

Fig. 2.23. Probability of $|\rho_{HV}|>1$ for UPRT time-domain, SPRT time-domain, and SPRT frequency-domain processing.

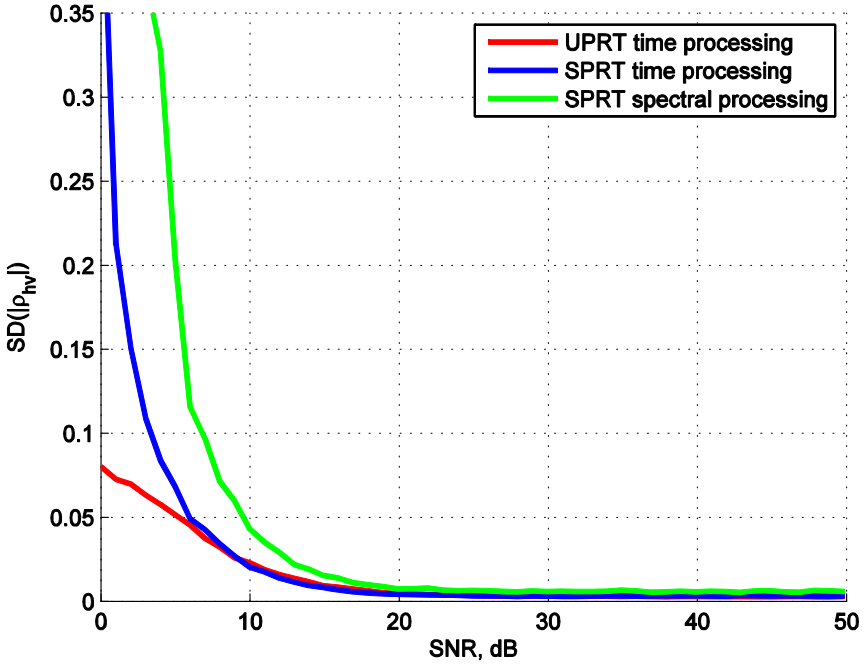

Fig. 2.24. Standard deviation of $|\rho_{HV}|$ for UPRT time-domain, SPRT time-domain, and SPRT frequency-domain processing.

3. The CLEAN-AP Filter

Ground clutter mitigation (detection and filtering) continues to be a major concern for operational ground based Doppler weather radar systems. For the WSR-88D system, the Radar Operations Center (ROC) has received field complaints of reflectivity loss along the contour of zero velocity (zero-isodop); "hot spots" within clutter regions; and spatial irregularities in the reflectivity, velocity, and spectrum width fields (Data Quality Team personal correspondence 2010). The performance of the clutter mitigation algorithm has a direct impact in all these areas of concern. Ideally, the detection algorithm should apply (or bypass) the ground clutter filter when ground clutter is present (or absent) in the received radar signal. As well, the ideal ground clutter filter should provide effective ground clutter removal with minimum disturbance of the desired weather signal. The goal of the two algorithms is to work collectively to mitigate ground clutter and provide quality meteorological estimates of reflectivity, velocity, and spectrum width. To accomplish this goal, the detection algorithm should not miss a ground-clutter contaminated gate; otherwise, the unfiltered ground clutter results in hot spots. Just as important, the ground clutter filter should not overly suppress ground clutter when the detection algorithm falsely identifies a clutter–contaminated gate. Such false detections create irregularities or partial/complete loss of the meteorological estimates. Thus, an integrated ground clutter mitigation algorithm is warranted. That is, an algorithm for which the detection and filtering characteristics are tuned to the clutter characteristics of the received radar signals. In this report, we describe the CLutter Environment ANalysis using Adaptive Processing (CLEAN-AP © 2009 Board of Regents of the University of Oklahoma) filter (Warde and Torres, 2009). The CLEAN-AP filter provides a real-time,

integrated clutter mitigation solution with: (a) improved ground clutter suppression, (b) effective ground clutter detection, and (c) dynamic ground clutter suppression characteristics optimally matched to the existing ground clutter environment.

3.1. Background

Radar backscatter from the ground (or fixed targets on the ground), known as ground clutter, can contaminate weather signals, often resulting in severely biased meteorological estimates. If not removed from the estimate, the ground clutter contamination tends to bias reflectivity high as well as biasing radial Doppler velocity and spectrum width toward zero. A ground clutter filter (GCF) can mitigate this contamination and provide unbiased meteorological estimates but usually with reduced quality. However, the overall quality of the meteorological estimates needlessly suffers when a GCF is applied when no ground clutter contamination exists and the weather signal has near-zero Doppler velocities. In this case, significant biases result from the misapplication of the GCF. Preferably, the GCF should only be applied if the ground clutter contamination contaminates (biases) the weather signal. Thus, judicious application of the GCF is needed to mitigate ground clutter contamination.

Typically, weather radars use static clutter maps (i.e., pre-identified clutter contaminated regions) to control the application of the GCF. However, anomalous propagation conditions can cause the radar beam to increase contact or overshoot ground clutter, giving the appearance that the clutter shifts within or disappears from the radar volume coverage very rapidly. This constant shift of the ground clutter in the radar volume coverage renders static clutter maps ineffective for controlling the application of the GCF

in a dynamic atmosphere. Fortunately, spectral examination of the received echoes provides a means to determine the presence of ground clutter in real time without having to rely on static clutter maps. A disadvantage of using spectral analysis on a finite number of samples comes from spectral leakage; hence, data windows are classically applied to contain this detrimental effect. It is desirable to use low dynamic range windows to preserve the quality and resolution of the meteorological estimates. However, high dynamic ranges windows may be required to adequately suppress strong ground clutter returns, consequently reducing the quality and resolution of the meteorological estimates.

The CLEAN-AP spectral GCF is capable of mitigating the adverse effects of ground clutter contamination while preserving the quality of the meteorological estimates. This 'smart' filter performs real-time detection and suppression of ground clutter returns in dynamic atmospheric environments.

3.2. CLEAN-AP Performance Analysis

The CLEAN-AP filter clutter mitigation performance was reported by Warde and Torres (2009) using a MATLAB implementation and signal simulations. Additionally, Warde and Torres (2010) used recorded time-series data from WSR-88D operational sites to qualitatively assess the detection performance of the CLEAN-AP filter. The results from the simulations and the real data show that the CLEAN-AP filter meets and in most cases exceeds the WSR-88D requirements for both ground clutter detection and filtering. The analysis reported here and in Warde and Torres (2009, 2010) was completed using empirically derived notch widths based on a Gaussian model with expected spectrum width of 0.28 m/s and velocity of 0 m/s.

3.2.1. *Analysis Methodology*

The CLEAN-AP filter performance is characterized using a MATLAB implementation of the algorithm. Simulations of weather and clutter were generated from Gaussian power spectra (Zrnić 1975). To reduce windowing effects and to provide a pseudo-continuous spectrum, the number of spectral coefficients is increased by a factor of three and the resulting time series signal is truncated to create a uniformly spaced signal of the appropriate sample size. The statistical performance of the filter is characterized over a range of parameters with one hundred realizations created for each parameter set.

3.2.2. *Clutter Suppression Requirements*

The CLEAN-AP filter was compared against requirements detailed in the WSR-88D System Specifications 2810000H dated 25 April 2008, chapter 3.7.2.7 "Ground Clutter Suppression". Although the system specification includes filter requirements for dual polarization, only the single polarization requirements for reflectivity, velocity, and spectrum width are statistically assessed in this report. The WSR-88D System Specification (SS) is written for an Infinite-Impulse Response (IIR) filter with selectable notch widths; thus, some of the specifications do not apply to frequency domain filters using automatic adaptable notch widths (Ice et al. 2004a and 2004b). The goal of ground clutter filtering is to remove the effects of ground clutter bias on reflectivity, velocity, and spectrum width while providing meaningful estimates of these moments (i.e., small errors of estimates). To that end, the WSR-88D SS provides bias and standard deviation requirements for the application of a filter for a signal at 20 dB signal-to-noise ratio (SNR) with a weather spectrum of 4 m/s. Clutter model A of the WSR-88D SS provides

for a zero-mean normally distributed clutter model and is most relevant for this ground clutter filter evaluation. Although not specified in the WSR-88D SS, a 0.28 m/s clutter spectrum width is used for this evaluation which is in line with the expected clutter spectrum width of 0.1 m/s when accounting for spectrum broadening due to the antenna scanning motion. Additionally, 0.28 m/s clutter spectrum width provides ready comparison with earlier filter evaluations conducted for the WSR-88D system at the Radar Operation Center (e.g., Sirmans 1992, Ice et al. 2004a).

When applied, the filter is required to provide a clutter suppression capability of 30 dB in the reflectivity channel and selectable clutter suppression levels from 20 dB to 50 dB in the Doppler channel (velocity and spectrum width) where clutter suppression is defined as the ratio of the input power to the output power after application of the clutter filter. The bias on the moments caused by the application of the filter is assessed with a signal-to-clutter ratio (SCR) of 30 dB. In the bias assessment, the low clutter level with high signal level is used so that the prominent contributor to the moment bias is associated with the filter performance and not due to clutter residue. An additional allowance in moment bias is provided in the WSR-88D SS when clutter residue is present in the output signal: reflectivity bias of 1 dB for an output SCR of 10 dB, velocity bias of 1 m/s for an output SCR of 11 dB and spectrum width bias of 1 m/s for an output SCR of 15 dB.

The filtered reflectivity bias requirement is assessed with a weather signal at 0 m/s and is dependent on the spectrum width of the weather as shown in table 3.1 (reproduced from the WSR-88D SS). As can be seen in table 3.1, the bias in reflectivity is expected to increase as the weather spectrum width becomes small compared to the notch width of

the clutter filter. The bias in reflectivity is due to portions of the weather signal coincident with the notch width of the filter centered at 0 m/s. When the weather signal is completely contained within the notch width of the filter, the entire weather signal moments are likely to be unrecoverable (i.e. severely biased).

Weather Spectrum Width (m/s)	Maximum Bias of Reflectivity (dB)
1	10
2	2
≥3	1

Table 3.1. WSR-88D Filtered Reflectivity Bias Requirements

The filtered Doppler moments have a bias requirement of less than 2 m/s over a range of usable velocities as a function of the notch width selection as shown in table 3.2 (reproduced from the WSR-88D SS). As mentioned earlier, this requirement is for an IIR filter with selectable notch widths. The WSR-88D system no longer uses an IIR filter; however, filtered velocity and spectrum width bias and standard deviation can be assessed to ensure 2 m/s is not exceeded for all usable velocities above those minimums stated on the left side of table 3.2 when the filter provides the clutter suppression level listed on the right side of the table.

Notch Width Selection	Minimum Usable Velocity (m/s)	Clutter Suppression (dB)
Low	2	20
Medium	3	28
High	4	50

Table 3.2. WSR-88D Usable Filtered Velocity Requirement

3.2.3. *Reflectivity Clutter Suppression and Bias Analysis*

Two examples of the clutter suppression performance of the CLEAN-AP filer are shown in figures 3.1 and 3.2. In these figures, two scatter plots of filtered power bias as a

function of input clutter-to-signal ratio (CSR) level show the clutter suppression performance of the CLEAN-AP filter. The simulated weather signal has an SNR of 20 dB with a 4 m/s spectrum width and representative velocities uniformly distributed throughout the Nyquist co-interval. The PRT for these examples are 882 μs and 1000 μs, respectively. The dwell time is set at 40 ms giving 45 samples for figure 3.1 and 64 samples for figure 3.2. The input CSR levels used are -30 dB and 0 dB to 100 dB in 5 dB step sizes. At each CSR level, 5000 (50 velocities x 100 realizations) power bias results are shown. The color scale indicates the percentage of occurrences at each power bias level with the maroon indicating 100% (100 occurrences) and white indicating 0% (0 occurrences). Optimal clutter suppression performance is indicated when the power bias is at 0 dB. Clutter residue is present when the power bias increases above 0 dB; while over-suppression occurs when the power bias drops below 0 dB. In each scatter plot, high occurrences (>90%) are seen in red along the zero power bias with a quick taper to near zero occurrences on either side of zero power bias. The clutter suppression performance of the tested filter can be estimated at the point where the highest occurrence of power bias level (blue line) departs from zero power bias. For the examples in figure 3.1, clutter suppression is seen at ~70 dB; whereas, clutter suppression is seen at ~80 dB in figure 3.2. The red ovals indicate over-suppression that begin at ~60 dB in both figures. In both cases, the CLEAN-AP clutter suppression performance is above the WSR-88D requirement of 50 dB. Although not shown, reduced number of samples and different PRT settings meet or exceed the 50 dB requirement.

Another measure of CLEAN-AP filter performance is seen when compared to current (GMAP) and past (IIR) filters used in the WSR-88D system. The comparisons are made

in Surveillance, Clear Air, and Doppler weather modes which make up the VCP scanning strategies employed on the WSR-88D system for both precipitation and clear air operations. The simulated weather signal has a 20 dB SNR. Although the WSR-88D SS reflectivity bias requirement applies to all radial velocities, the reflectivity bias effects of ground clutter filtering are more prominent at 0 velocity. Thus, the evaluation is performed with the signal centered at 0 velocity. The spectrum width is varied from 0.1 to 0.5 m/s in 0.1 m/s steps and from 1 to 4 m/s in 1 m/s steps. At each spectrum width, the average of 100 reflectivity (power) bias results is shown. The CSR is set at -30 dB to assess the filter's influence in the stop band when no clutter contamination is present. The -30 dB CSR setting is chosen in accordance with the WSR-88D SS and is expected to have no appreciable bias on the reflectivity estimate.

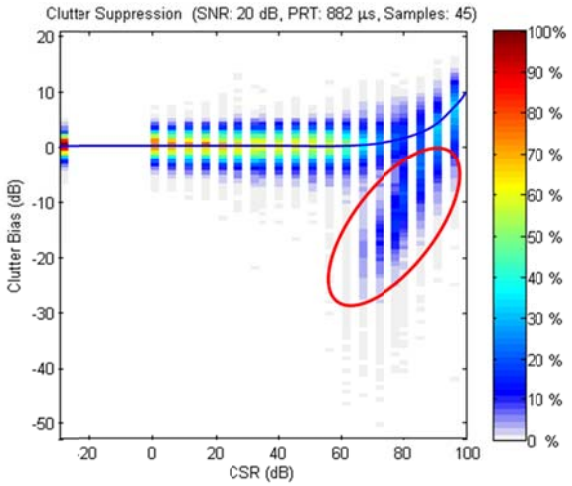

Fig. 3.1. Clutter suppression of the CLEAN-AP filter for a signal with 882µs PRT, 20 dB SNR, 4 m/s spectrum width and velocities uniformly distributed across the Nyquist co-interval. The simulated clutter signal varies from -30 dB to 100 dB CSR and has a 0.28 m/s spectrum width centered on a velocity of 0 m/s. The histogram includes 5000 realizations for each CSR level. The blue line shows the mean value of the estimate and the red oval surrounds a region of over-suppression.

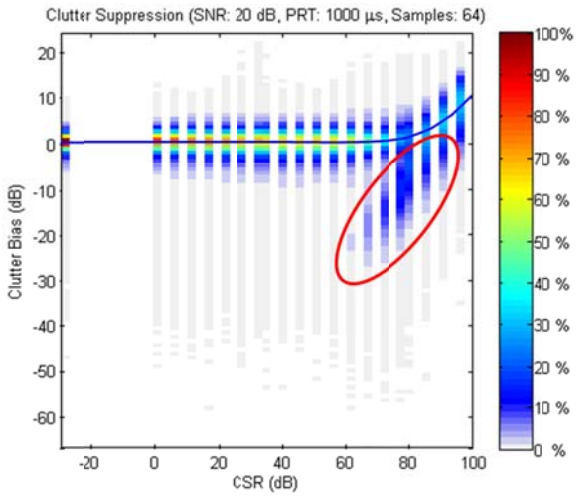

Fig. 3.2. Clutter suppression of the CLEAN-AP filter for a signal with 1000µs PRT, 20 dB SNR, 4 m/s spectrum width and velocities uniformly distributed across the Nyquist co-interval. The simulated clutter signal varies from -30 dB to 100 dB CSR and has a 0.28 m/s spectrum width centered on a velocity of 0 m/s. The histogram includes 5000 realizations for each CSR level. The blue line shows the mean value of the estimate and the red oval surrounds a region of over-suppression.

3.2.4. *Surveillance Mode*

In the Surveillance mode, long PRTs (~3000 µs) are used to sample the convective environment at low elevation angles providing reflectivity coverage to ~450 km. The unambiguous reflectivity range is established by the relationship $cT_s/2$ where T_s is PRT of the waveforms under test. To meet the unambiguous reflectivity range of 450 km, a PRT of 3100 µs is used with a sample size of 16 pulses. Figure 3.3 shows the reflectivity bias of all three filters (legacy IIR, GMAP, CLEAN-AP) in the Surveillance weather mode as a function of the true weather-signal spectrum width. The reflectivity bias requirements from table 3.1 are plotted in figure 3.3 as blue circled x's to provide easy reference to the WSR-88D requirements. The legacy IIR filter is shown with three notch width suppression levels (high (blue), medium (green) and low (orange)) (e.g., Sirmans

1992). The GMAP filter (magenta) is displayed with the operational clutter spectrum seed width of 0.4 m/s (e.g., Ice 2004a). The PRT of 3106 μs with 16 samples (dwell ~50 ms) was used for the evaluation. It is seen that the CLEAN-AP filter (light green) meets the reflectivity bias levels at all spectrum width values and easily exceeds WSR-88D requirements in the Surveillance mode.

The performance enhancement seen in the CLEAN-AP filter is due to two aspects of the algorithm. At narrow spectrum widths (<1 m/s), the dominating factor that improves CLEAN-AP performance over the other filters shown in figure 3.1 is attributed to the use of the spectral leakage in the lag-1 ASD phases to correctly identify the spectral components with clutter contamination. At wider spectrum widths, the adaptive window feature of the algorithm automatically adjusts the suppression level of the filter based on the measured power at 0 frequency (seen in figure 3.3 at wide spectrum widths >1 m/s). This is because a wider spectrum signal will have less power concentrated around the mode of the spectrum (in this case 0 velocity or DC level). The bias changes seen in the CLEAN-AP filter plot above 1.5 m/s are attributed to the algorithm choosing lower dynamic range windows as a function of wider spectrum width signals. This feature of the CLEAN-AP filter helps to preserve the quality of the weather estimates. When a signal is away from the zero-isodop, no DC component is measured and the rectangular window is automatically selected giving the best quality for all the weather estimates.

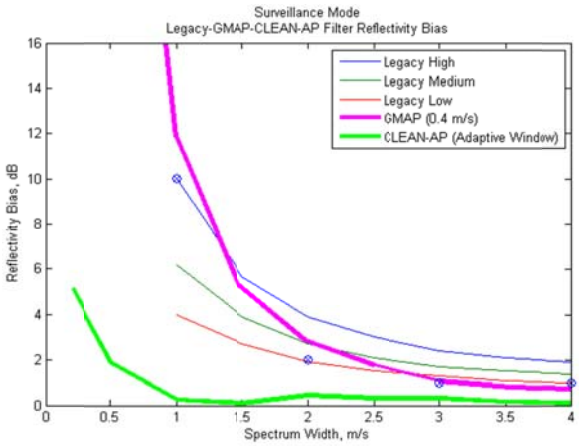

Fig. 3.3. Surveillance mode – reflectivity bias error imparted by the filter as a function of spectrum width. The simulated Gaussian signal has an SNR of 20 dB with a velocity of 0 m/s. Plotted are the reflectivity biases for the WSR-88D legacy filter (IIR – high (blue), medium (green) and low (orange)), the GMAP filter (0.4 m/s seed width and Blackman window (magenta)) and the CLEAN-AP filter (light green).

3.2.5. *Clear Air Mode*

The Clear Air mode is used when expected precipitation is low and provides increased sensitivity for low signal detection (FMH-11). The WSR-88D has two VCP definitions for the Clear Air mode: VCP 31 (long pulse width) and VCP 32 (short pulse width). The filter evaluation is equally applicable to both modes. The plots in figure 3.4 provide a ready comparison of the reflectivity bias for both the CLEAN-AP filter (light green) and the GMAP filter (magenta) as true spectrum widths range from 0.1 m/s to 4 m/s. The signal PRF is 450 Hz (~2222 μs PRT) with 64 samples (~142 ms dwell). In the Clear Air mode, the CLEAN-AP filter is seen to easily meet the reflectivity bias requirements of the WSR-88D SS at all spectrum widths. Again, the enhanced performance of CLEAN-AP filter over the GMAP filter is attributed to the use of the lag-1 ASD phase and the automated window selection feature. In this mode, the CLEAN-AP filter imparts less than 0.25 dB of bias to the reflectivity estimate for true spectrum widths above 1 m/s;

whereas, the GMAP filter imparts ~4 dB of reflectivity bias at a spectrum width of 1 m/s and does not reduce to the 0.25 dB bias level until the spectrum width is above 3 m/s.

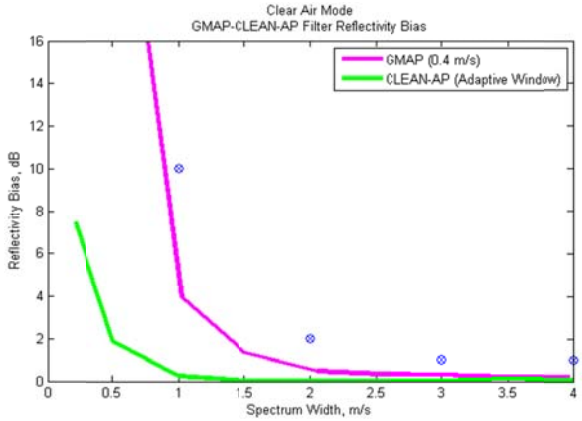

Fig. 3.4. Clear Air mode – reflectivity bias error imparted by the filter as a function of spectrum width. The simulated Gaussian signal has an SNR of 20 dB with a velocity of 0 m/s. Plotted are the reflectivity biases for the GMAP filter (0.4 m/s seed width and Blackman window (magenta)) and the CLEAN-AP filter (light green).

3.2.6. *Doppler Mode*

In the Doppler mode, shorter PRTs are used to extend the Nyquist co-interval; however, the unambiguous range is reduced thus making overlaid echoes more likely, especially at the lowest elevations levels of the VCP. In the intermediate and upper elevations, storm top heights of 70 kft are quickly reached due to the earth's curvature (Doviak and Zrnić 1993), eliminating the concern for overlaid echoes since storm tops above this height are extremely rare.

Figure 3.5 shows reflectivity bias as a function of true spectrum width for legacy IIR, GMAP and CLEAN-AP filters. As in the Surveillance mode, the legacy IIR filter has selections for high, medium and low notch widths. The filters are supplied a signal with a PRF of 1000 Hz (1000 μs PRT) with 64 samples (64 ms dwell). The input signal has a 20

dB SNR with a velocity of 0 m/s. The spectrum width is increased from 0.1 to 4 m/s. The CLEAN-AP filter is shown to provide reflectivity bias performance that exceeds the WSR-88D requirements for the Doppler mode.

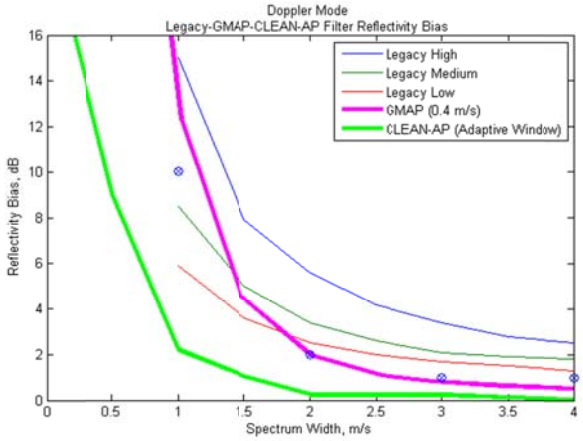

Fig. 3.5. Doppler mode – reflectivity bias error imparted by the filter as a function of spectrum width. The simulated Gaussian signal has an SNR of 20 dB with a velocity of 0 m/s. Plotted are the reflectivity biases for the WSR-88D legacy filter (IIR – high (blue), medium (green) and low (orange)), the GMAP filter (0.4 m/s seed width and Blackman window (magenta)) and the CLEAN-AP filter (light green).

3.2.7. *Velocity Bias Analysis*

If not removed from the composite signal, ground clutter biases the weather velocity estimate toward zero while the power (reflectivity) is increased by the amount of clutter power present in the composite signal. The weather velocity estimate can still be biased toward zero even after filtering when enough clutter remains in the signal at the output to the filter. When all or part of the weather signal is in the filter stop band, the estimates of weather signal velocity and power may be unrecoverable or severely biased. The WSR-88D SS provides guidance for velocity biases for an IIR filter outside the pass bands of 0.875, 1.25, and 1.75 m/s for legacy low, medium, and high notch width selections (Sirmans 1992). For each notch width selection (low, medium, and high), table

3.2 shows the usable velocities that should be unaffected by the filtering process when the clutter suppression levels are at 20, 28 and 50 dB (respectively). In the passband of the filter, the WSR-88D SS allows a 2 m/s bias and 2 m/s standard deviation for these usable velocities. Ice et al. (2004a and 2004b) evaluated the GMAP filter and found that it meets WSR-88D requirements for velocity bias and standard deviation.

Like the GMAP filter, the CLEAN-AP filter does not use a fixed notch width; however, velocity biases and standard deviations can still be established for the conditions listed in table 3.2. The weather signal used for this test has a 20 dB SNR and 4 m/s spectrum width with varying levels of clutter. As seen in figures 3.1 and 3.2, the CLEAN-AP filter starts to overly suppress the clutter signal at around 60 dB. Before this level of clutter, the CLEAN-AP filter without clutter model control meets the WSR-88D requirements for velocity bias and standard deviation, so these images are not shown. However, it is more interesting to see how the CLEAN-AP filter compares to the GMAP filter above the 50 dB clutter level.

In figure 3.6, a histogram of the velocity estimate bias after filtering is shown as a function of true weather velocity for a 20 dB weather signal with a CSR of 55 dB. The PRT is set to 1000 μs and has 64 samples. The filtered weather velocity bias is evaluated at 50 velocities throughout the Nyquist co-interval. For each true velocity, results from 100 realizations are shown and the color indicates the percentage of occurrences. For this example, CLEAN-AP shows < 1 m/s biases and < 1 m/s standard deviation across the complete Nyquist co-interval (including in the stop band). This is typical performance for the CLEAN-AP filter below 55 dB CSR.

Compare the CLEAN-AP filter performance to that of the GMAP filter for the same conditions. In figure 3.7, the GMAP filter produces larger biases and increased standard deviations, especially near ±10 m/s. The GMAP filter imparts velocity biases in the region from -10 m/s to 10 m/s that appear linear. This is due to the clutter residual present in the filter output which biases the velocity estimate toward 0 m/s. Ice et al. (2004a) reported power biases of 0.25 dB at 50 dB CSR increasing to 3.88 dB at 60 dB CSR for the GMAP filter using the same signal parameters. As the power bias increases, the clutter residual becomes the prominent contributor to the velocity estimate which biases the velocity estimate toward zero. For example, figure 3.7 shows that approximately -5 m/s bias is imparted on the velocity estimate at 10 m/s true velocity. This translates to a velocity estimate of 5 m/s (10 true + -5 bias = 5 estimated). Thus, the clutter residual caused a 5 m/s underestimate in velocity at a true velocity of 10 m/s. Another artifact caused by clutter residue is shown in the region of the stop band (near 0 m/s) of the GMAP filter where there appear to be small bias and standard deviation. Increased performance in the areas of clutter suppression with reduced velocity biases of the CLEAN-AP filter over the GMAP filter for this example is, once again, attributed to the use of the lag-1 ASD phases. That is, the CLEAN-AP filter uses phases to identify the notch width; whereas, the GMAP filter uses the magnitudes.

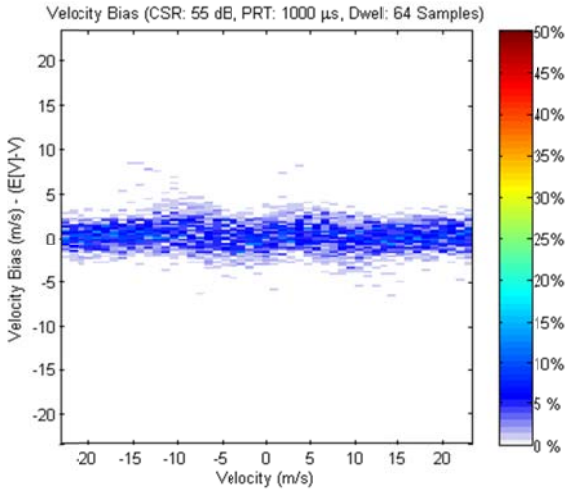

Fig. 3.6. Velocity bias of the CLEAN-AP filter as a function of true velocity. The CSR is 55 dB with a simulated weather signal of 20 dB SNR and 4 m/s spectrum width. For each true velocity, the results of 100 realizations are shown and the color indicates the percentage of occurrences.

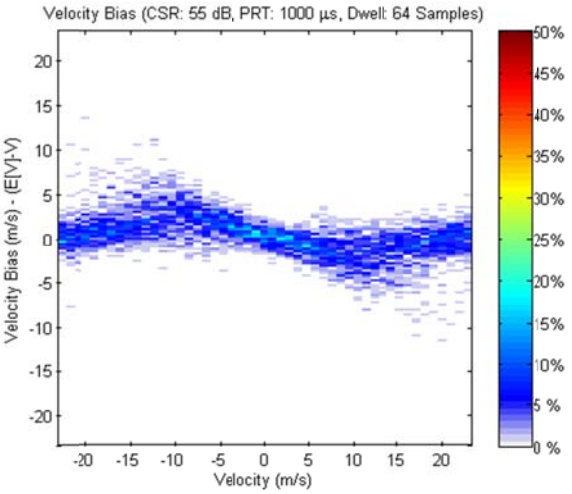

Fig. 3.7. Velocity bias of the GMAP filter as a function of true velocity. The CSR is 55 dB with a simulated weather signal of 20 dB SNR and 4 m/s spectrum width. For each true velocity, the results of 100 realizations are shown and the color indicates the percentage of occurrences.

Increasing the CSR to 60 dB, shows how both filters fail to provide unbiased estimates of velocity. In figure 3.8, the CLEAN-AP filter imparts biases that are caused by over suppression. Reexamine figure 3.2, the red oval region outlines the over-suppressed region; however, not all of the estimates are biased as seen by the blue bias line. The

over-suppressed region can be identified and censored by using the identified clutter contaminated coefficients of the lag-1 ASD as a guide. This technique is used in the CLEAN-AP implementation on the National Weather Research Testbed (NWRT) Phased Array Radar (PAR) but is not discussed in this report. Removing these over-suppressed values leaves velocity estimates that are again within the WSR-88D requirements. Compare the CLEAN-AP filter performance to the GMAP filter performance for the same conditions. In figure 3.7, the GMAP filter completely fails to remove the clutter contamination as seen by the nearly linear bias values running from approximately 23 m/s (bias) at a true velocity of -23 m/s to approximately -23 m/s (bias) at a true velocity of 23 m/s. The enhanced performance of the CLEAN-AP filter comes from the addition of the Blackman-Nuttal data window which has first sidelobe levels of -98 dB. For CSR above ~58 dB, the failure of the GMAP filter to remove the clutter contamination is attributed to the insufficiently low Blackman data window sidelobes. The addition of the Blackman-Nuttal data window to the CLEAN-AP algorithm increases its clutter suppression capability reducing data window sidelobe artifacts.

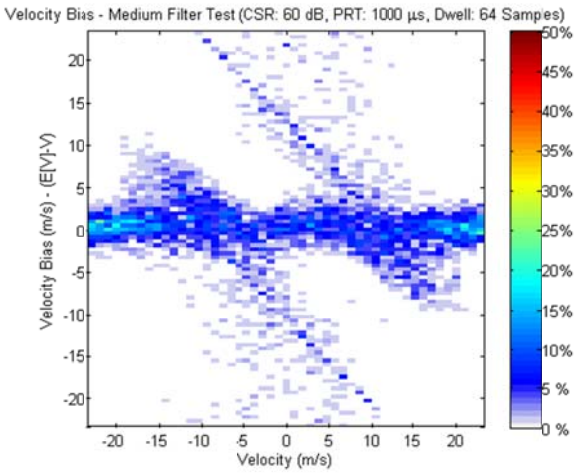

Fig. 3.8. Velocity bias of the CLEAN-AP filter as a function of true velocity. The CSR is 60 dB with a simulated weather signal of 20 dB SNR and 4 m/s spectrum width. For each true velocity, the results of 100 realizations are shown and the color indicates the percentage of occurrences.

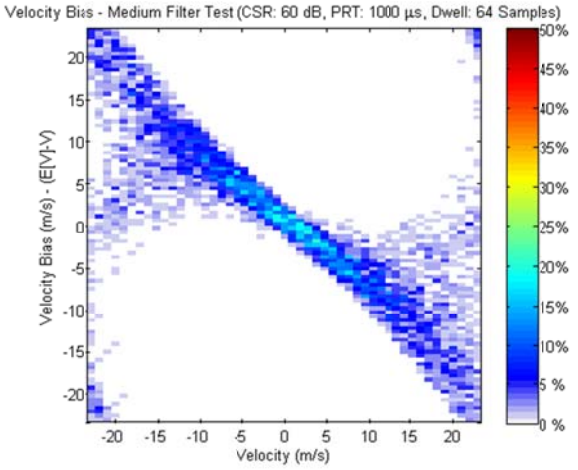

Fig. 3.9. Velocity bias performance of the GMAP filter as a function of true velocity. Clutter level is at 60 dB CSR with a simulated weather signal of 20 dB SNR and 4 m/s spectrum width. For each true velocity, 100 realizations are shown and the color indicates the percentage of occurrences.

3.2.8. *Spectrum Width Bias Analysis*

When clutter filtering is applied, the WSR-88D SS requirements for spectrum width bias and standard deviation are 2 m/s for an input spectrum width of 4 m/s. An additional 1 m/s allowance is provided for spectrum width bias when a clutter residue of -15 dB CSR is present at the output of the filter. The estimator used for these tests is the R0/R1 estimator described by Doviak and Zrnić (1993). At times, the R0/R1 estimator can give a spectrum width estimate that is nonsensical. These values are normally set to 0 m/s in the estimation routine for the WSR-88D system. For the bias and standard deviation estimates, these artificial zeros are removed.

Recall that the CLEAN-AP filter starts to overly suppress the clutter signal at around 60 dB. Before this level of clutter, the CLEAN-AP filter without clutter model control meets the WSR-88D requirements for spectrum width bias and standard. Figure 3.10 through 3.13 show histograms of spectrum width biases as a function of true spectrum width. The color scale shows the level of occurrence of each spectrum width estimate with 500 estimates made for each true spectrum width value. For each true spectrum width value, the mean spectrum width bias is shown with red circles; red vertical bars are used to display the spectrum width standard deviation. The red horizontal lines at ±2 m/s represent the bias requirements of the WSR-88D SS.

Seen in figure 3.10, the CLEAN-AP filter has biases < 1 m/s for all true spectrum widths. Additionally, the standard deviations are ≤ 1 m/s for true spectrum widths above 0.5 m/s and below 7 m/s with values ≤ 2 m/s above 0.1 m/s and below 9 m/s. Contrast the CLEAN-AP filter performance (figure 3.10) with the GMAP filter performance in figure

3.11. The GMAP filter imparts a positive bias for all true spectrum widths tested. The bias constraint imposed by the WSR-88D SS of 2 m/s is achieved in the interval from 3 m/s to 9 m/s. If the 1 m/s bias constraint for clutter residual is added; then, the lower bound can be reduced to 1 m/s. Still, the standard deviation constraint imposed by the WSR-88D SS of 2 m/s is not achieved for any true spectrum width values tested. The advantage realized by the CLEAN-AP filter is due to its increased clutter suppression capability and readily attributed to the use of the unbiased autocorrelation estimator derived from the ASD.

When the CSR is 60 dB, the CLEAN-AP filter performance degrades (figure 3.12). Spectrum width biases are still below 2 m/s, but errors increase above the 2 m/s standard deviation level for true spectrum widths below about 3 m/s. The GMAP filter performance degrades as well with increased bias and standard deviation shown in figure 3.13.

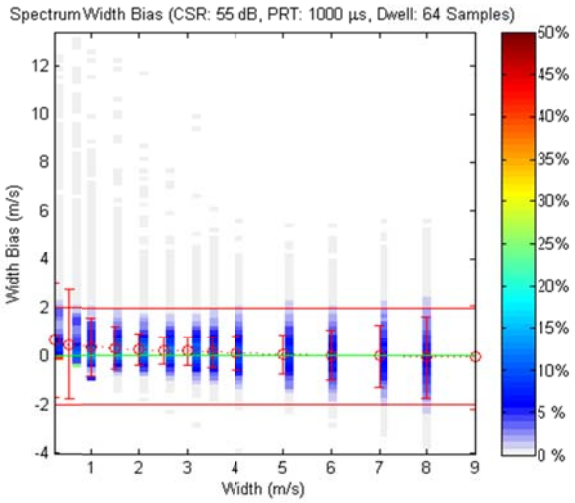

Fig. 3.10. Spectrum width bias of the CLEAN-AP filter as a function of true spectrum width. The CSR is 55 dB with a simulated weather signal of 20 dB SNR and velocities throughout the Nyquist co-interval. For each true spectrum width, results from 500 realizations are shown and the color indicates the percentage of occurrences.

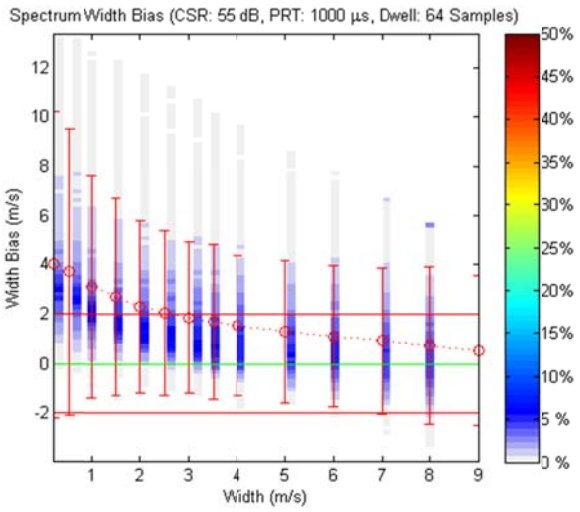

Fig. 3.11. Spectrum width bias of the GMAP filter as a function of true spectrum width. Clutter level is at 55 dB CSR with a simulated weather signal of 20 dB SNR and velocities throughout the Nyquist co-interval. For each true spectrum width, 500 realizations are shown and the color indicates the percentage of occurrences.

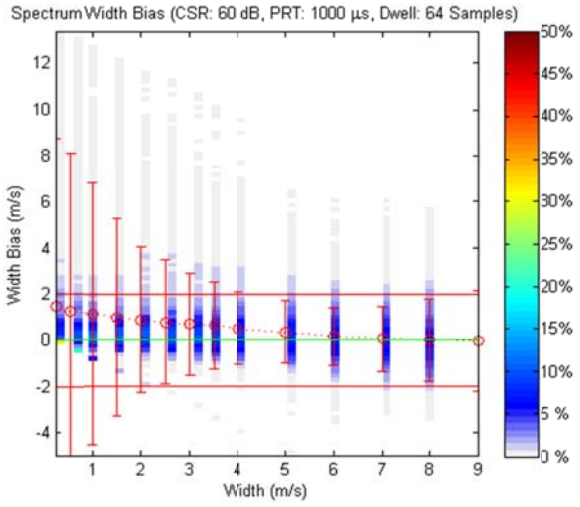

Fig. 3.12. Spectrum width bias performance of the CLEAN-AP filter as a function of true spectrum width. Clutter level is at 60 dB CSR with a simulated weather signal of 20 dB SNR and velocities throughout the Nyquist co-interval. For each true spectrum width, 500 realizations are shown and the color indicates the percentage of occurrences.

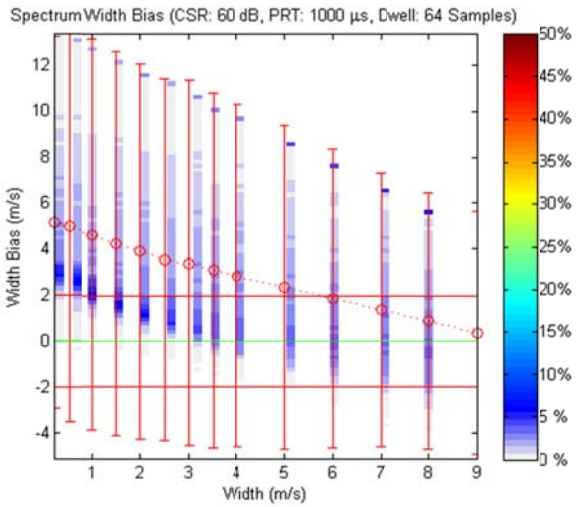

Fig. 3.13. Spectrum width bias of the GMAP filter as a function of true spectrum width. Clutter level is at 60 dB CSR with a simulated weather signal of 20 dB SNR and velocities throughout the Nyquist co-interval. For each true spectrum width, 500 realizations are shown and the color indicates the percentage of occurrences.

3.2.9. *Real Data Analysis*

The CLEAN-AP filter provides a complete ground clutter mitigation capability incorporating both detection and filtering of ground clutter into a single integrated solution. The WSR-88D system has two separate algorithms to accomplish ground clutter mitigation. The GMAP filter provides the filtering for each range bin independent of other range bins; accordingly, the filter can be characterized using statistical analysis with simulations (e.g., Ice et al. 2004a). The Clutter Mitigation Decision (CMD) algorithm (Hubbert et al. 2009) provides the detection of ground clutter for the WSR-88D system (Ice et al. 2009). The CMD algorithm uses spatial continuity within a fuzzy logic framework to provide a decision to filter or not filter. As such, only a subjective analysis with real data can be used to compare the detection features of the CLEAN-AP clutter mitigation with that of CMD/GMAP clutter mitigation.

The CLEAN-AP filter was developed and has been operating on the NWRT PAR since the fall of 2008 in support of MPAR research (Torres et al. 2009). The PAR can acquire all measurements of the atmospheric environment using electronic beam steering; i.e., without antenna beam smearing from scanning. To transfer this technology to the WSR-88D, which measures the atmosphere by scanning in azimuth, it is beneficial to show that the CLEAN-AP filter can perform well with the effects of beam smearing. Although there was no tasking to NSSL from the ROC for the CLEAN-AP algorithm, the ROC agreed to provide an example of CMD/GMAP clutter mitigation for a cursory comparison with CLEAN-AP clutter mitigation. The ROC provided the lowest elevation level of 0.5° of a VCP 32 with super resolution enabled for this comparison. CMD is ran on the Surveillance scan at the 0.5° elevation, but not on the Doppler scan at the same elevation. Therefore, only the reflectivity is shown. For this comparison, CLEAN-AP and CMD/GMAP are compared using time series data collected from the WSR-88D at Tucson, AZ (KEMX) on April 22, 2009 during beta testing of the CMD implementation into the WSR-88D (Ice et al. 2009). The data set was chosen because of the mountainous terrain that surrounds the radar. During the beta test of the CMD/GMAP system, missed detections created persistent areas of high reflectivity in the Santa Catalina mountains (red ovals in figure 3.14) causing a redesign of the implementation of the CMD algorithm in the WSR-88D (Ice personal correspondence 2009). Time series data were played back both in the MATLAB environment to get the CLEAN-AP reflectivity output and in an offline WSR-88D system (e.g., Rhoton et al. 2005) to get the CMD/GMAP reflectivity output. Additionally, the unfiltered reflectivity was provided by the ROC through the offline WSR-88D system. The unfiltered and CMD/GMAP reflectivity outputs were

ingested into the MATLAB environment for display and direct comparison to the CLEAN-AP reflectivity. Figure 3.14 shows the comparison of CMD/GMAP (panel (a)), unfiltered (panel (b)), and CLEAN-AP (panel (c)) reflectivity output for this clear-air case. From this view, it can be seen that both CMD/GMAP and CLEAN-AP performed equally well in providing automated ground clutter mitigation. However, upon closer inspection of the figures, there are some interesting observations.

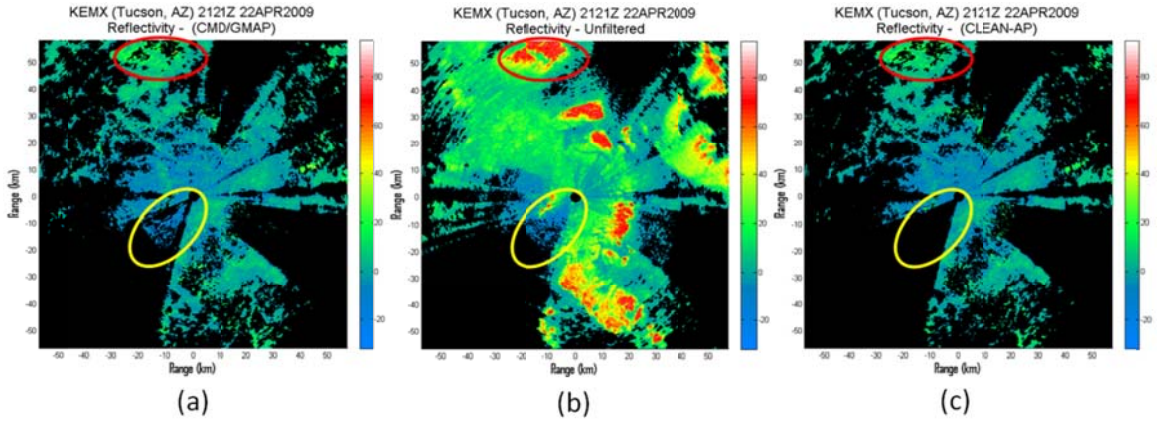

Fig. 3.14. Reflectivity replayed from time series data collected by the WSR-88D at Tucson, AZ (KEMX) on April 22, 2009. The red oval encompasses high clutter returns north-northwest of the radar in the Santa Catalina mountains on Mt. Lemon. The yellow oval encompasses low clutter returns south-west of the radar (a) Output of the WSR-88D offline system with CMD/GMAP enabled. (b) Output of the WSR-88D offline system with no clutter mitigation enabled (unfiltered). (c) Output from MATLAB with CLEAN-AP enabled.

Figure 3.15 shows a closer view of the Santa Catalina mountains (red oval north-northwest of the radar in figure 3.14). The high reflectivity values shown in the unfiltered reflectivity (panel (b)) are returns from the Santa Catalina mountains on Mt. Lemon. Both systems, CMD/GMAP (panel (a)) and CLEAN-AP (panel (c)) achieve nearly the same performance in mitigating the ground clutter; however, there is still evidence of high reflectivity values in the CMD/GMAP ground mitigation scheme (panel (a) red arrow). The reduced value in this region by the CMD/GMAP ground clutter mitigation scheme

indicates that CMD properly detected the region, but the GMAP filter did not provide adequate clutter suppression. Compare the CMD/GMAP performance to the CLEAN-AP performance in panel (c) (red arrow). Here, the CLEAN-AP filter properly detected and removed the ground clutter from this region.

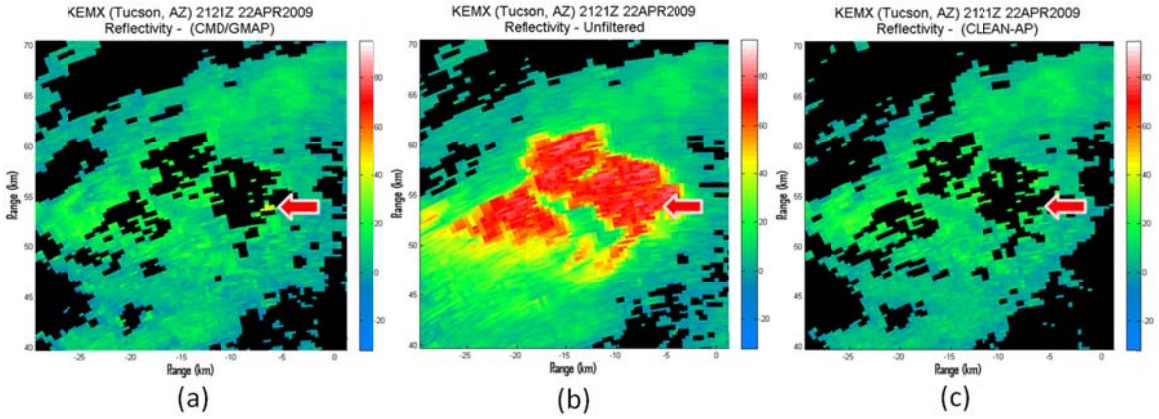

Fig. 3.15. Reflectivity replayed from time series data collected by the WSR-88D at Tucson, AZ (KEMX) on April 22, 2009. The region displayed is north-northwest of the radar in the Santa Catalina mountains on Mt. Lemon. (a) Output of the WSR-88D offline system with CMD/GMAP enabled. The red arrow shows that clutter mitigation was complete effective in removing the ground clutter. (b) Output of the WSR-88D offline system with no clutter mitigation enabled (unfiltered). (c) Output from MATLAB with CLEAN-AP enabled. The red arrow shows that clutter mitigation effectively removed the ground clutter.

In figure 3.16 (yellow oval in southwest region of the radar in figure 3.14), low level ground clutter from -20 to 8 dB is experienced. This low-level ground clutter is undetected by the CMD algorithm (left panel of figure 3.16), but is removed by the CLEAN-AP filter (right panel of figure 3.16). Although, this low-level ground clutter may seem operationally insignificant; upon closer inspection, there may be some operational impacts. It is evident that the radar experiences some beam blockage by the unnatural discontinuity in the reflectivity images from approximately 196° to 245° in azimuth, but rising terrain still provides substantial clutter returns in the region. The clutter power in this region after removing range correction and calibration adjustments is

between 13 to 41 dB clutter-to-noise ratio (CNR). The signal power from distributed targets drops at a rate of the $1/R^2$ (inverse range squared). Thus, weather signals at far ranges are weak compared to clutter signals near the radar. When weather signals exceed the unambiguous range in the Doppler scan, the weather signal will overlay (range fold) into this undetected/unfiltered ground clutter. The operational implications is that range folded echoes in the Doppler scan become masked by the unfiltered ground clutter caused by missed detection in the Surveillance scan. Additionally, the Doppler velocity and the spectrum width fields in the Doppler scan are biased toward zero where the unfiltered ground clutter remains causing discontinuities in these Doppler fields. These discontinuities can impede the performance of the velocity dealiasing and Velocity Azimuth Display (VAD) wind profile algorithms. Not only are the weather signatures biased by the unfiltered ground clutter, but insect and bird signatures are masked/biased as well when ground clutter is present. Although more real data cases are needed to provide a thorough evaluation of the CLEAN-AP filter; the preliminary evaluation provided shows great promise.

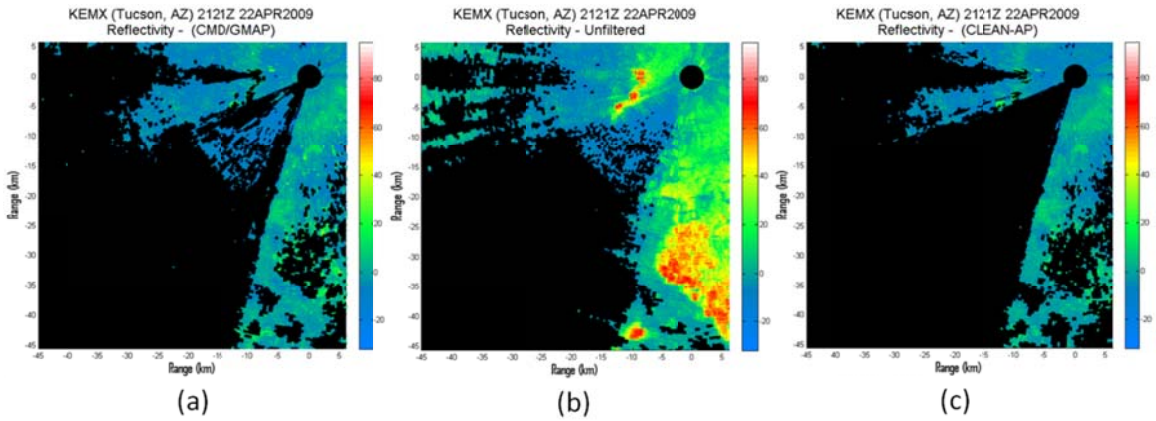

Fig. 3.16. Reflectivity replayed from time series data collected by the WSR-88D at Tucson, AZ (KEMX) on April 22, 2009. Low-level ground clutter is present in the region southwest of the radar from 196° to 245° in azimuth. (a) Output of the WSR-88D offline system with CMD/GMAP enabled. Residual ground clutter is present in the region due to non-detection. (b) Output of the WSR-88D offline system with no clutter mitigation enabled (unfiltered). (c) Output from MATLAB with CLEAN-AP enabled. Clutter mitigation effectively removed the ground clutter in the region.

3.3. References

Doviak, D. and D. Zrinć, 1993: Doppler Radar and Weather Observations, 2nd edition. Academic Press.

Data Quality Team, 2010: Personal correspondence.

Hubbert, J., M. Dixon, and S. Ellis, 2009: Weather radar ground clutter. Part II: Real-Time Identification and Filtering, Journal of Atmos. Oceanic Technol., vol. 26, 1118-1196.

Ice, R., D. Warde, D. Sirmans, D. Rachel, 2004a: Report on Open RDA – RVP8 Signal Processing, Part 1 – Simulation Study, WS-88D Radar Operations Center Report, January 2004. 87 pp.

___, D. Warde, D. Sirmans, D. Rachel, 2004b: Report on Open RDA – RVP8 Signal Processing, Part 2 – Engineering Analysis with Meteorological Data, WS-88D Radar Operations Center Report, July 2004. 56 pp.

___, R. Rhoton, J. Krause, D. Saxion, O. Boydstun, A. Heck, J. Chrisman, D. Berkowitz, W. Zittel, and D. Warde, 2009: Automatic clutter mitigation in the WSR-88D, design, evaluation, and implementation, Preprints 34th Radar Conf., Williamsburg, VA, Amer. Metoer. Soc.

___, (Radar Operations Center), 2009: Personal correspondence.

Rhoton, R., D. S. Saxion, G. T. McGehee, R. L. Ice, D. A. Warde, D. Sirmans, 2005: Radar Operation Center (ROC) Progress in RVP8 Time Series Playback for Signal Processing Evaluation, 21st International Conference on Interactive Information Processing Systems for Meteorology, Oceanography, and Hydrology.

Sirmans, D., 1992: Clutter filtering in the WSR-88D, OSF Internal Report. 125 pp.

Torres, S. M., C. Curtis, I. Ivic, D. Warde, E. Forren, J. Thompson, D. Priegnitz, and R. Adams, 2009: Update on signal processing upgrades for the National Weather Radar Testbed. Preprints, 25th IIPS for Meteorology, Oceanography, and Hydrology, Phoenix, AZ, USA, Amer. Meteor. Soc.

Warde, D. A. and D. M. Torres, 2009: Automatic detection and removal of ground clutter contamination on weather radars. Preprints, 34th Conference on Radar Meteorology, Williamsburg, VA, USA, Amer. Meteor. Soc.

Warde, D. A. and D. M. Torres, 2010: A novel ground-clutter-contamination mitigation solution for the NEXRAD network: the CLEAN-AP filter. Preprints, 26th Conference on IIPS for Meteorology, Oceanography, and Hydrology, Atlanta, GA, USA, Amer. Meteor. Soc.

WSR-88D System Specifications 2810000H, 25 April 2008, Radar Operations Center, 160 pp.

Zrnić, D. S., 1975: Simulation of weather like Doppler spectrum and signals, Journal of Applied Meteorology, 14, 619-620.

4. Evaluation of the Hybrid Spectrum Width Estimator

[This section follows in its original format]

1 Introduction

The spectrum width is a well known radar parameter related to the dispersion of radial velocities, and its value can be potentially useful for measuring the turbulent nature of radar scatterers and leading to better warnings of severe weather events (Lemon, 1999) and means of detecting turbulence for air transportation (Mahapatra, 1999). The popular approach for measuring the spectrum width uses a pulse pair logarithm approach, however its performance is questionable at the narrow spectrum where significant biases are observed. This deficiency can be be problematic in many weather conditions where a large dispersion range of velocities is observed; for example, a sheared layer that is commonly observed can produce significantly differing dispersion signatures depending on radar range, elevation angle, and other factors, and all these measurements are needed. As a result, an accurate and reliable technique for measuring the spectrum over a wide range is needed in order to instill confidence in this useful radar parameter.

Recently, a hybrid technique using multiple autocorrelation-based approaches to estimate this parameter was introduced Meymaris et al. (2009b). It was claimed that the values produced had better root-mean-squared error at the narrower spectrum width range compare to the popular approach. In this report, the performance of this estimator such as bias, variance, frequency of zeros were examined using simulations. While it will be shown that the results validates the claims, it was observed that some simple modifications can be made

to further improve the performance.

2 Methodology

2.1 Hybrid Spectrum Width Estimator

The method as described in Meymaris et al. (2009b) provides an estimate of the dispersion of the radial velocity by selecting from one of three temporal autocorrelation-based techniques a value of the estimated spectrum width that most appropriately describes characteristics obtained from the inputted short time sequence. An illustration of the method is depicted in Figure 1 for an aliasing velocity of 25 ms^{-1}, and it shows the three available choices with their appropriate ranges that can be seen to depend on the estimated spectrum width value and input time sequence length. According to Meymaris et al. (2009b), the three ranges are systematically given the label small, medium, and large. While not explicitly stated, these thresholds appears to have been obtained via simulations. Additionally, a fourth estimator based on the parabolic form of the autocorrelation function is used to provide the initial guess of the estimated spectrum width.

The approach for obtaining the spectrum width estimate of the short time series sequence $v(k)$ with M samples begins by estimating its auto correlation, which is defined as

$$R_i[v] \;=\; \frac{1}{M-i}\sum_{k=0}^{M-i-1} v^*(k)v(k+i). \tag{1}$$

Additionally, let $r[i] = |R_i[v]|$.

The hybrid spectrum width estimators uses a combination of the w_{13}, w_{12}, and w_{01} to provide

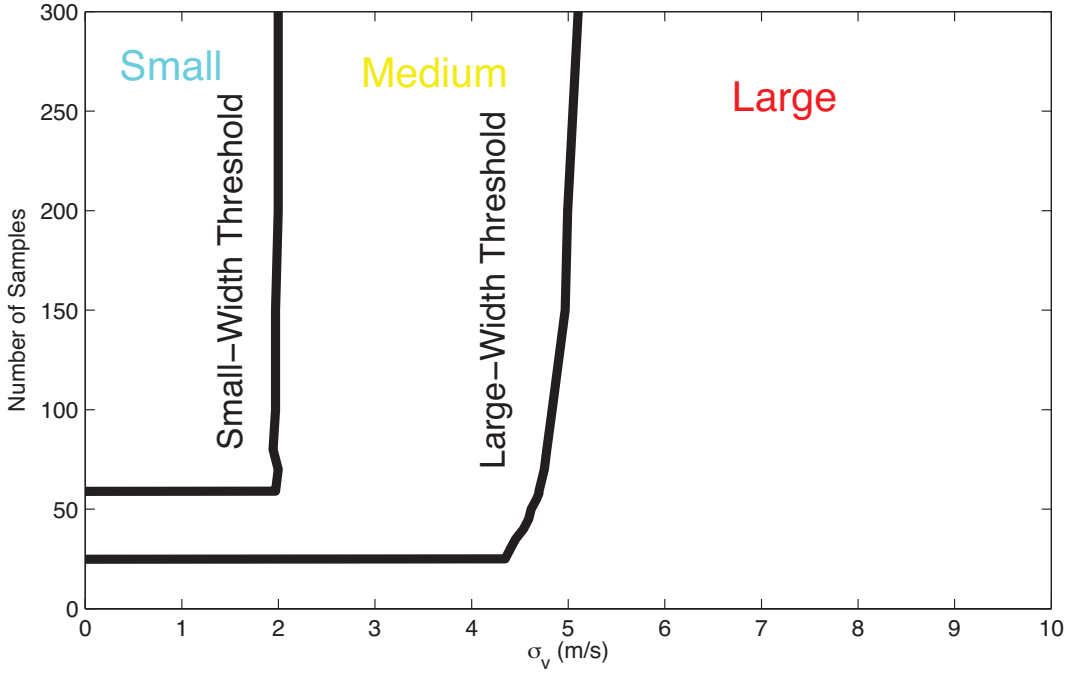

Figure 1: Hybrid Spectrum Width Estimator Model for an aliasing velocity of 25 ms^{-1}. Two sets of thresholds, which are labeled "small" and "large" widths in this figure, are used for categorizing the estimated spectrum width values and for selecting the choice of spectrum width estimator.

the spectrum width estimate. When the input spectrum width is small, the output of the w_{13} estimator is used within this range. If $r[3] \geq r[1]$ then $w_{13} = 0$, else

$$w_{13} = \frac{\sqrt{2}}{\pi\sqrt{3^2 - 1^2}} v_a \left[\ln\left(\frac{r[1]}{r[3]}\right) \right]^{1/2}, \quad (2)$$

where v_a is the aliasing velocity. At the medium range, the w_{12} estimator is used. The output of this estimator is: If $r[2] \geq r[1]$ then $w_{12} = 0$, else

$$w_{12} = \frac{2\sqrt{2}}{\pi\sqrt{3}} v_a \left[\ln\left(\frac{r[1]}{r[2]}\right) \right]^{1/2} \quad (3)$$

At the largest range, the w_{01} estimator is used. The output of this estimator is: If $r[1] \geq r[0] - P_N$ then $w_{01} = 0$, else

$$w_{01} = \frac{\sqrt{2}}{\pi} v_a \left[\ln\left(\frac{r[0] - P_N}{r[1]}\right) \right]^{1/2}, \quad (4)$$

where P_N is the noise power.

The fourth estimator that is used in the initial spectrum width estimate is

$$w_{012} = \frac{1}{\pi} v_a \sqrt{-2 \min(0, -0.1923 \ln(r[0] - P_N) - 0.0769 \ln(r[1]) + 0.2692 \ln(r[2]))} \quad (5)$$

The normalized spectrum width thresholds are listed in Table 1 according to Meymaris et al. (2009a). The values listed depend only on the number of samples and increase with large samples size, and linear interpolation is used to obtain the thresholds for sample sizes that fall between those listed.

The following pseudo-code can be used to describe this technique:

- Use Table 1 to obtain the thresholds.
- If $1/2(w_{01} + w_{012})$ is larger than the large values threshold, use the value obtained from w_{01}. Else,

Table 1: Hybrid Spectrum Width Thresholds (normalized to v_a from Meymaris et al. (2009a))

M	Thresholds	
	Small Values	Large Values
23.0000	-1.0000	-1.0000
24.0000	-1.0000	-1.0000
25.0000	-1.0000	0.1610
30.0000	-1.0000	0.1630
35.0000	-1.0000	0.1650
40.0000	-1.0000	0.1680
45.0000	-1.0000	0.1700
50.0000	-1.0000	0.1710
55.0000	-1.0000	0.1730
58.0000	-1.0000	0.1740
59.0000	0.0730	0.1740
70.0000	0.0740	0.1760
80.0000	0.0720	0.1770
100.0000	0.0730	0.1790
150.0000	0.0730	0.1840
200.0000	0.0740	0.1850
300.0000	0.0740	0.1890

- if w_{13} is smaller than the small values threshold, use the value obtained from w_{13}. Else,
- use the value obtained from w_{12}.

3 Modified Hybrid Spectrum Width Estimator

Compared to the results obtained using w_{01}, the results obtained using the hybrid spectrum width estimator are significantly improved. These results will, however, be presented later. Nevertheless, one of the most obvious improvement is observed at narrow spectrum widths, where the standard deviation and bias are better, which lead to better mean-squared error values at these ranges. Additionally, the percentage of complex widths obtained at the narrow spectrum widths, which is also a measure of the performance at these range, decreases when using the hybrid spectrum width estimators. These two improvements are desirable in providing better spectrum width estimates.

Even though the performance of the hybrid spectrum width estimator is improved compared to that of the w_{01} estimator, its performance could be improved using several simple modifications. Observe the optimal estimator range for these values shown in Figure 2. The solid black lines are the thresholds used in the hybrid spectrum width estimator. The color images below these lines depict the optimal choice of the estimated spectrum width estimator for different sets of sample sizes, signal-to-noise ratio, and spectrum width values. The values for the small, medium, and large thresholds for optimal performance actually varies according to these parameters and do not match the static thresholds as presented for the hybrid spectrum width estimator. By matching these thresholds, some additional improvements in the estimated spectrum width can be obtained.

Another modification to the hybrid spectrum width estimator that can be applied to improve the estimated spectrum width is to incorporate the w_{adp} estimator at the small spectrum width when the signal-to-noise ratio is sufficiently large. This estimator, which was presented

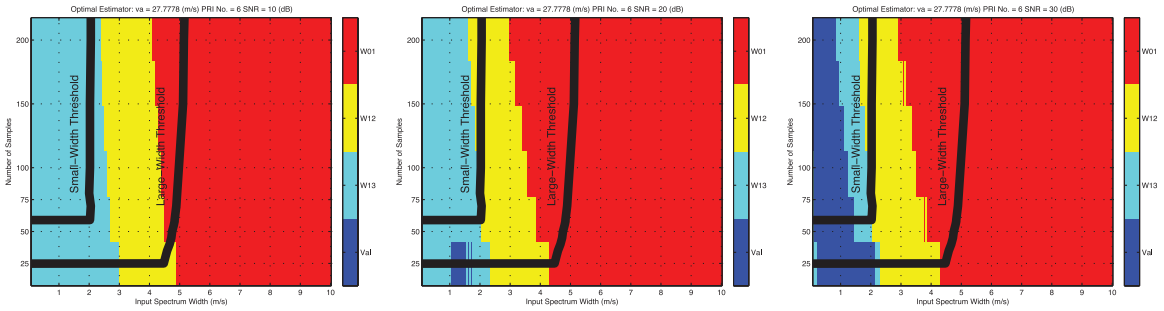

Figure 2: Overlay of the hybrid spectrum width thresholds versus the range obtained for the optimal estimator (based on mean-squared error). Left to right: SNR = 10 (dB), SNR = 20 (dB), and SNR = 30 (dB).

in Melnikov and Doviak (2002), has the advantage of lower bias and standard deviation compared to the w_{13} estimator when these conditions are satisfied, and the frequency of non-zero estimates at the small spectrum width is lower using this estimator. The w_{adp} estimator has the following expression

$$w_{adp} = \frac{v_a}{\pi} \left| \ln \left(\frac{1}{\left\{ 1 - \left[\frac{\triangle P}{r[0] - P_N} \right]^{1/2} \right\} \{1 + \mathrm{SNR}\}^{1/2}} \right) \right|^{1/2}, \tag{6}$$

where

$$\triangle P = \frac{1}{M-1} \sum_{k=0}^{M-2} |v(k+1)|^2 - |v(k)|^2. \tag{7}$$

When $\triangle P >= P$, set $w_{adp} = 0$.

A final modification to the hybrid spectrum width estimator involves applying data quality control by exploiting conditions when one or multiple of the w_{01} w_{12} or w_{13} estimators produce a zero value. This modification aims at limiting the estimated spectrum width value to the small range from the knowledge that the condition to realize such a value is statistically insignificant at the medium and rare at the large spectrum width ranges. This conditional

probability example, which is illustrated in Figure 3 using simulated data, shows that the true spectrum width should be small when one of the three w_{01} w_{12} or w_{13} estimators produce zero values. As a result, it is possible to replace the zero value with a non-zero but a small value produced by one of the other estimator and track for conditions when narrow spectrum width values are incorrectly estimated. Shown in Tables 2 and 3 are now thresholds values for the w_{01} and w_{12} estimators that depend on signal-to-noise ratios and number of samples.

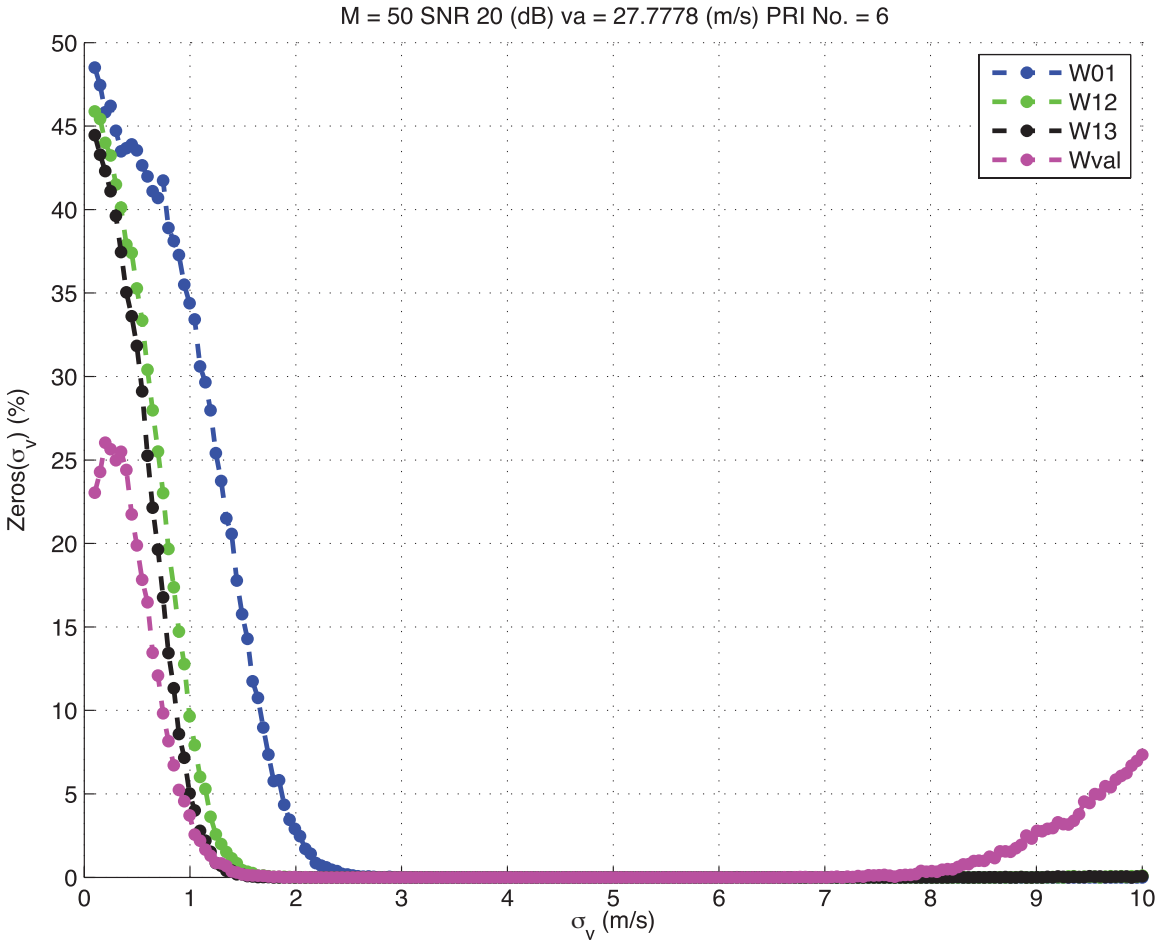

Figure 3: Frequency of estimates with zero values for a selected simulation case.

Additionally, the threshold for w_{apd} are $\begin{bmatrix} 0.80 & 0.95 & 1.10 & 1.25 & 1.50 & 1.95 \end{bmatrix}$ for $M = \begin{bmatrix} 25 & 50 & 75 & 100 & 150 & 200 \end{bmatrix}$, respectively when the SNR is above 20 dB.

The following pseudo-code can be used to describe this technique:

Table 2: Hybrid Spectrum Width Thresholds for w_{01} (Non-normalized)

M / SNR	10 (dB)	20 (dB)	25 (dB)	30 (dB)
25	4.9500	4.3500	4.3500	4.2500
50	4.6000	3.8500	3.8500	3.8000
75	4.4500	3.6000	3.5500	3.5000
100	4.3500	3.4000	3.3500	3.4000
150	4.2500	3.1500	3.1500	3.1000
200	4.1000	3.0000	2.9500	2.9500

Table 3: Hybrid Spectrum Width Thresholds for w_{12} (Non-normalized)

M / SNR	10 (dB)	20 (dB)	25 (dB)	30 (dB)
25	2.8500	2.3500	2.2500	1.9500
50	2.7000	2.1500	2.0500	1.5000
75	2.5900	2.0000	1.9500	1.2500
100	2.5000	1.9000	1.8500	1.1000
150	2.4500	1.7000	1.6500	0.9500
200	2.4500	1.6500	1.6000	0.8000

- Use Tables 3 and 2 and linear interpolation to obtain the thresholds. Additionally, obtain the threshold for w_{apd} if needed.

- If w_{01} is larger than the large values threshold, use the value obtained from w_{01}. Else,

- If w_{12} is larger than the medium threshold, use w_{12}. Else,

- If w_{apd} is smaller than its threshold use the value obtained from w_{apd}. Else,

- use w_{13}.

The following quality control of the estimated spectrum width values are used:

- If the SNR is above 20 dB, check to make sure the estimated value fall within its intended optimal range or use value of the estimator at the larger range.

- If the output spectrum width is zero, insert another spectrum width value from either w_{01} w_{12} and w_{13} if it is also small.

- If the output spectrum width value is large and at least one of the estimate of w_{01} w_{12} and w_{13} is small, either insert a replacement if it is small or insert 0.

4 Simulations and Results

The performance of the hybrid and modified hybrid estimators in terms of standard deviation, bias, mean-squared-error, and frequency of non-zero estimates was obtained via simulations. This was achieved by analyzing the output values of the spectrum width obtained from the w_{01}, hybrid spectrum width estimator, and the modified hybrid spectrum width estimators using input sequences that were generated using the technique described in Zrnić (1975). The performance of the estimators were observed for spectrum width values that ranged from 0.1 to 10 ms^{-1}, samples from 25 to 200, and signal-to-noise ratios from 10 to 30 dB. For each set of configuration, ten thousand independent sequences were generated, and the output from these simulations were used to obtain the statistics of the performance of the estimators.

4.1 Pulse Pair Logarithmic Estimator

For comparison, the performance of the w_{01} estimator was also simulated, and the values related to the performance of this estimator are plotted in Figure 4. The results show that the estimator performs relatively well when the spectrum width is larger than 2 ms^{-1}, and the performance of this estimator improves when either the number of samples or signal-to-noise ratio is increased. Additionally, the estimator has a bias value that is relatively near zero ($\approx$0 ms^{-1}) over this range, while it has a standard deviation that increases with larger values of the spectrum width. The performance of the estimator dramatically worsens and deviates from the desired values by several folds when the true spectrum width is below 2 ms^{-1} . Additionally, the estimator produces estimates that are zeros at a frequency of

approximately 50 % of the time when the spectrum widths less than 1 ms^{-1}. Compared to the frequency above 4 ms^{-1} where the frequency of zeros for the output values are insignificant, most of the values produced by this estimator in this small region are relatively ambiguous.

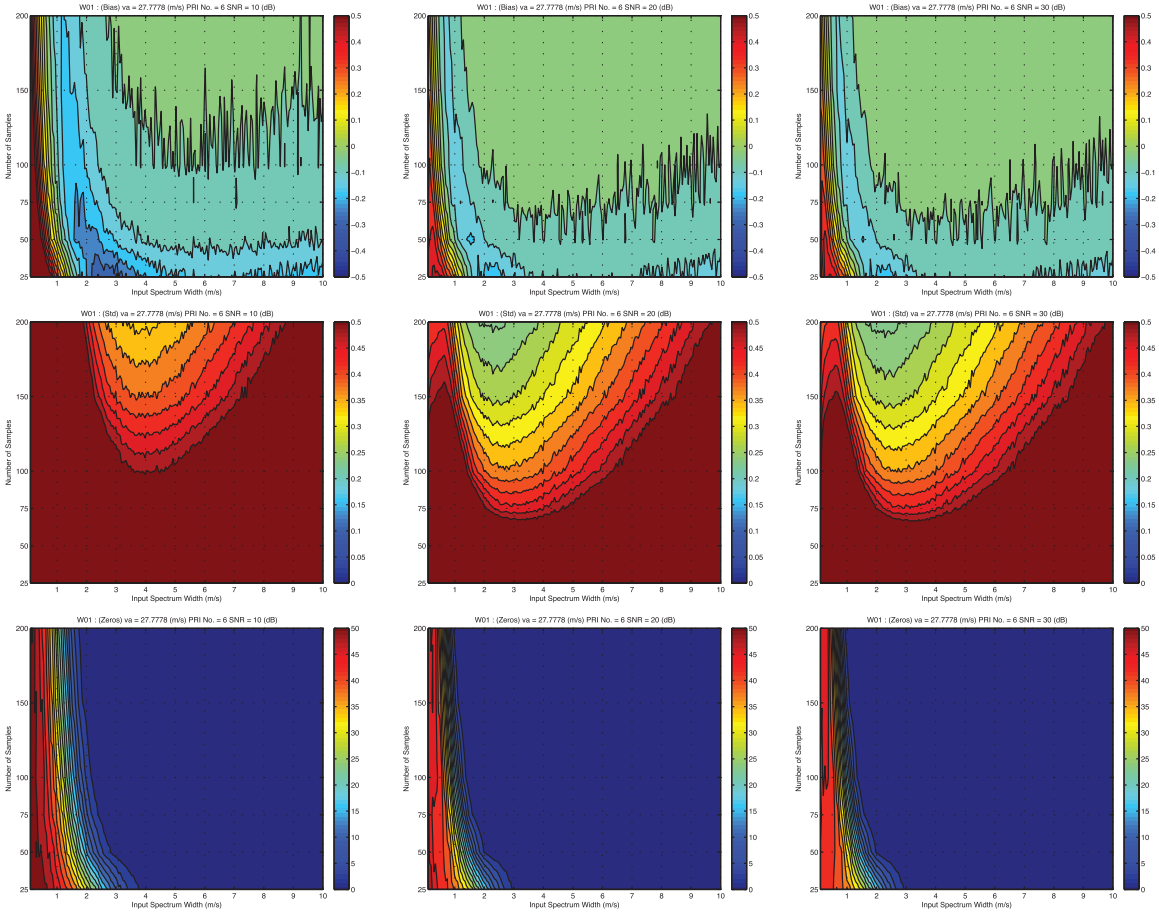

Figure 4: Performance of the w_{01} estimator: Top to bottom: bias, standard deviation, and frequency of zeros. Right to left: SNR = 10 (dB), SNR = 20 (dB), and SNR = 30 (dB).

4.2 Hybrid Spectrum Width Estimator

The same sequences of time series signals used in producing the statistics generated for the w_{01} estimator were also applied to the hybrid spectrum width estimator to evaluate its performance, and the results of these simulations are plotted in Figure 5. The results show that the hybrid spectrum width estimator are mostly desirable with values that are generally very good. When compared to the performance obtained using the w_{01} estimator, the results are similar when the spectrum width is greater than 7 ms^{-1}, while the results are more noticeably different below this soft threshold. At values below 4 ms^{-1}, the hybrid spectrum width estimator is consistently better the w_{01} estimator with lower values of bias, standard deviation, and frequency of zeros, which are all desirable. The difference is particularly evident for the results when the spectrum width is below 2 ms^{-1}, where the bias and standard deviation are closer to zero and the frequency of the zero estimates is smaller for the hybrid spectrum width estimator. In some cases, the performance of the hybrid spectrum width estimator is improved by at least 50% as compared to those obtained by the w_{01}. Unfortunately, the hybrid spectrum width estimator does not always perform better than the w_{01} estimator, and the results obtained for the hybrid spectrum width estimator with spectrum width between 4 and 7 ms^{-1} demonstrate this. Over this range of true spectrum width values, the degradation of the standard deviation observed with the hybrid spectrum width estimator is more detrimental than the improvement obtained with the bias . Nevertheless, the benefits of the hybrid spectrum width estimator gained from its improved performance over the w_{01} outweighs its disadvantageous, and its disadvantage is only relatively minor when these values are compared.

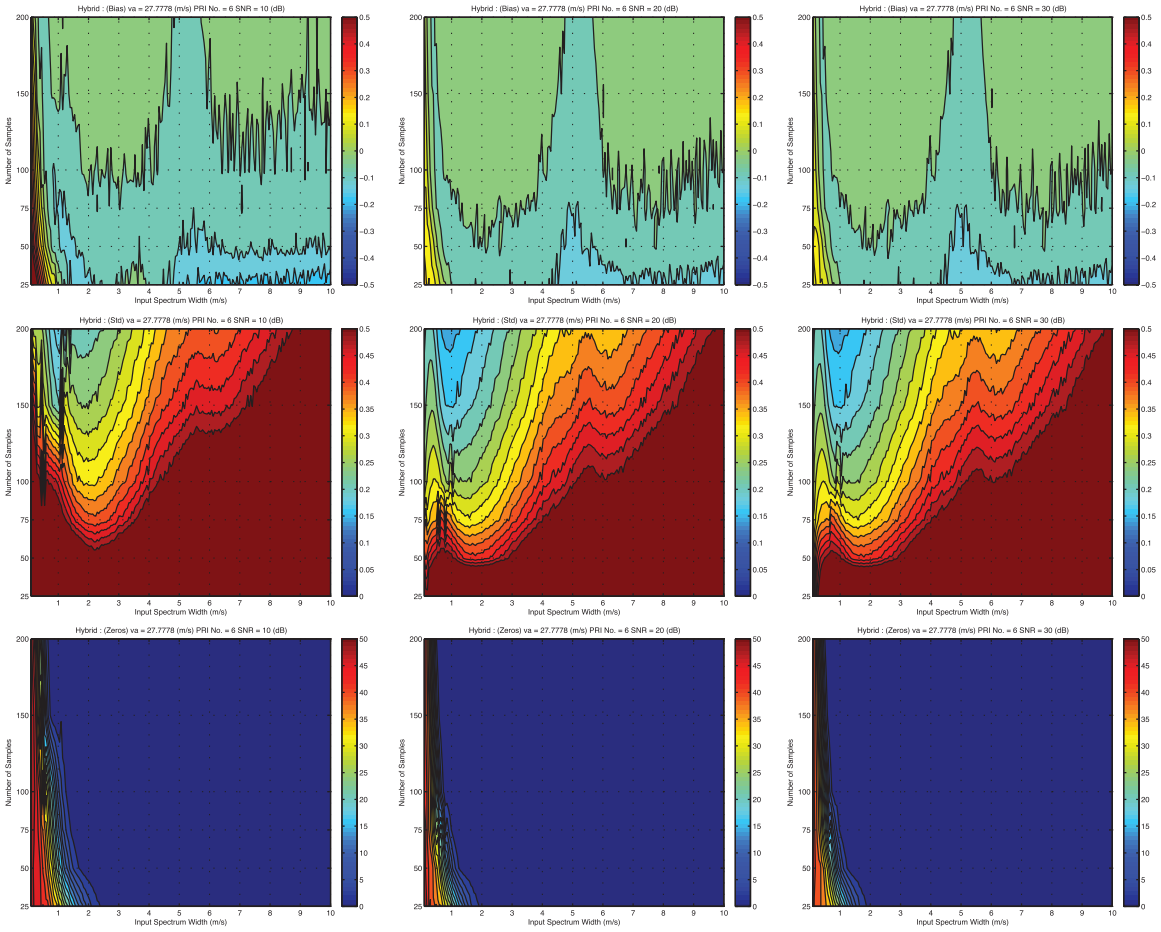

Figure 5: Performance of the hybrid spectrum width estimator: Top to bottom: bias, standard deviation, and frequency of zeros. Left to right: SNR = 10 (dB), SNR = 20 (dB), and SNR = 30 (dB).

4.3 Modified Hybrid Spectrum Width Estimator

A similar setup as used in evaluating the hybrid spectrum width estimator was used to obtain the performance of the modified hybrid spectrum width estimator. Using the same sequences of the time series signals, the results of these simulations are plotted in Figure 6 and show that the results obtained with the modified hybrid spectrum estimator are mostly desirable with values that are generally very good. When compared to the performance obtained using the w_{01} estimator, the results are better when the spectrum width is less than 5 ms^{-1}. The bias and standard deviation are closer to zero and the frequency of the zero estimates is significantly small for the modified hybrid spectrum width estimator. In some cases, the frequency of zeros generated by the modified hybrid spectrum width estimator is less than 25%, which is significantly better than that obtained using the w_{01} estimator. Unfortunately, the performance of the modified hybrid spectrum width estimator is slightly worse than the w_{01} estimator when the true spectrum width is larger than 5 ms^{-1} where a more negative bias is observed, and it is slightly worse when the spectrum width is between 3 and 6 ms^{-1} and the number of samples is less than 50, where the degradation of the standard deviation outweighs the benefit of the improved bias. In contrast, the performance of modified hybrid spectrum width estimator in term of the mean-squared error metric is generally as good or better than the hybrid spectrum width estimator. The comparison, which is plotted in Figure 7, shows that the modified hybrid spectrum width estimator outperform the hybrid spectrum width estimator in most cases and produces lower bias, standard deviation, and frequency of zeros. The modified hybrid spectrum width estimator produces worse bias when the spectrum width is larger than 5 ms^{-1}, and larger standard deviation when the number of samples is less than 50 and the true spectrum width is between 3 and 5 ms^{-1}.

Nevertheless, the performance of the modified spectrum width estimator is generally better than the hybrid spectrum width estimator.

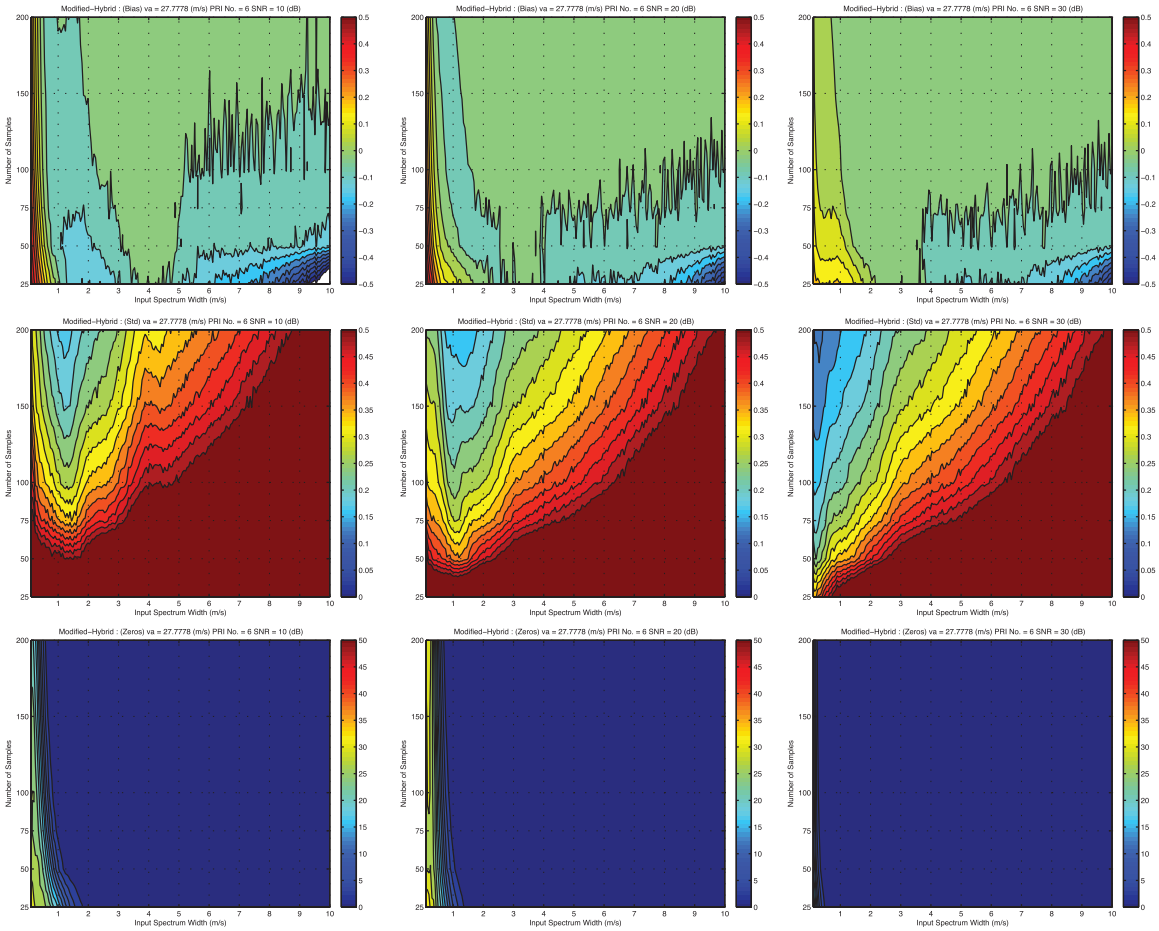

Figure 6: Performance of the modified hybrid spectrum width estimator: Top to bottom: bias, standard deviation, and frequency of zeros. Left to right: SNR = 10 (dB), SNR = 20 (dB), and SNR = 30 (dB).

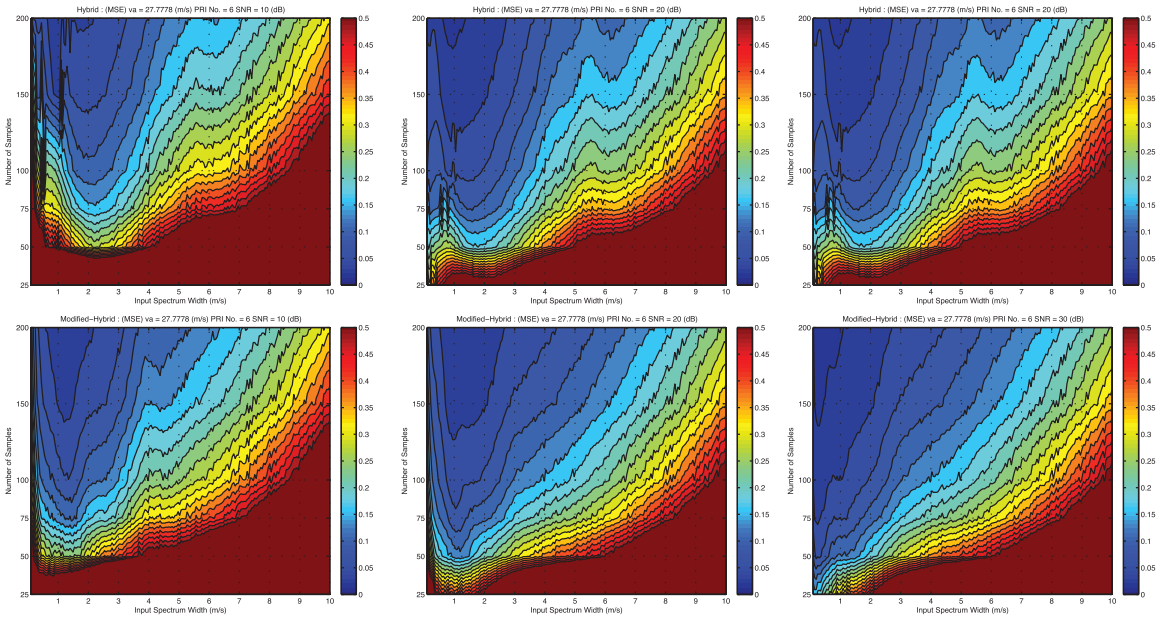

Figure 7: MSE of the original (top) and modified (bottom) hybrid spectrum width estimators. Left to right: SNR = 10 (dB), SNR = 20 (dB), and SNR = 30 (dB).

5 Conclusion

Results of the simulations to evaluate the hybrid spectrum width estimator show that this technique generally performs better than the w_{01} estimator. The results of the two techniques are approximately identical when the spectrum width is greater than 7 ms^{-1}, while a significant difference is observed below this soft threshold. At values below 4 ms^{-1}, the hybrid spectrum width estimator is consistently better than the w_{01} estimator with lower values of bias, standard deviation, and frequency of zero estimates, which are all desirable. The difference is particularly evident for the results when the spectrum width is below 2 ms^{-1}, where the bias and standard deviation are closer to zero and the frequency of the zero estimates is smaller for the hybrid spectrum width estimator. However, the hybrid spectrum width estimator performs worse than the w_{01} estimator when the true spectrum width ranges between 4 and 7 ms^{-1}, the signal-to-noise ratio is greater than 20 dB, and the number of samples is larger than 50. In these conditions, the degradation of the standard deviation that is observed with the hybrid spectrum width estimator is more detrimental than the improvement obtained from the bias. Nevertheless, the overall gains of the hybrid spectrum width estimator over the w_{01} estimator outweighs its disadvantageous, and the disadvantages are only relatively minor when these values are examined.

After the above simulations, some modifications that included using an adaptive threshold, incorporating the w_{adp} spectrum width estimator, and adding some quality control censoring were implemented into the hybrid spectrum width estimator. Using the same sequences of the time series signals, the results obtained with the modified hybrid spectrum estimator are also generally very good. When compared to the performance obtained using the w_{01}

estimator, the results are better when the spectrum width is less than 5 ms^{-1}. The bias and standard deviation are closer to zero and the frequency of the zero estimates is significantly better for the modified hybrid spectrum width estimator. Unfortunately, the performance of the modified hybrid spectrum width estimator is slightly worse than the w_{01} estimator when the true spectrum width is larger than 5 ms^{-1}, where a more negative bias is observed, and it is slightly worse when the spectrum width is between 3 and 6 ms^{-1} and the number of samples is less than 50, where the degradation of the standard deviation outweighs the benefit of the improved bias. Nevertheless, the general consensus is that it is a significant improvement over the w_{01} estimator. In contrast, the performance of modified hybrid spectrum width estimator in term of the mean-squared error metric is generally as good or better than the hybrid spectrum width estimator with lower bias, standard deviation, frequency of zeros. An exception occurred when the number of samples is less than 50 and the true spectrum width is between 3 and 5 ms^{-1}, where the modified hybrid spectrum width estimator produces worse bias when the spectrum width is larger than 5 ms^{-1}, and larger standard deviation.

References

Lemon, L., 1999: Operational uses of velocity spectrum width data. *29th Conf. on Radar Meteorology*, Montreal, QC, Amer. Meteor. Soc., 776–779.

Mahapatra, P., 1999: Aviation weather surveillance systems. *IEE Radar, Sonar, Navigation, and Avionics Series*, **8**, 458.

Melnikov, V. and R. Doviak, 2002: Spectrum widths from echo power differences reveal meteorological features. *J. Atmos. Oceanic Technol.*, **19 (11)**, 1793–810.

Meymaris, G., J. Williams, and J. Hubbert, 2009a: Hybrid spectrum width estimator. Tech. rep., The National Center for Atmospheric Research.

Meymaris, G., J. Williams, and J. Hubbert, 2009b: Performance of a proposed hybrid spectrum width estimator for the nexrad orda. *AMS 25th International Conference on Interactive Information and Processing Systems for Meterology, Oceanography and Hydrology*, Pheonix, AZ.

Zrnić, D. S., 1975: Simulation of weatherlike doppler spectra and signals. *J. Appl. Meteorol.*, **14**, 619–620.

LIST OF NSSL REPORTS FOCUSED ON POSSIBLE UPGRADES

TO THE WSR-88D RADARS

Torres S., M., D. Warde, and D. Zrnić, 2010: Signal Design and Processing Techniques for WSR-88D Ambiguity Resolution: Staggered PRT Updates. NOAA/NSSL Report, Part 13, 142 pp.

Torres S., M., D. Warde, and D. Zrnić, 2009: Signal Design and Processing Techniques for WSR-88D Ambiguity Resolution: Staggered PRT Updates and Generalized Phase Codes. NOAA/NSSL Report, Part 12, 156 pp.

Torres S., M. and D. Zrnić, 2007: Signal Design and Processing Techniques for WSR-88D Ambiguity Resolution: Evolution of the SZ-2 Algorithm. NOAA/NSSL Report, Part 11, 145 pp.

Zrnić, D.S., Melnikov, V. M., J. K. Carter, and I. Ivić, 2007: Calibrating differential reflectivity on the WSR-88D, (Part 2). NOAA/NSSL Report, 34 pp.

Torres S., M. and D. Zrnić, 2006: Signal Design and Processing Techniques for WSR-88D Ambiguity Resolution: Evolution of the SZ-2 Algorithm. NOAA/NSSL Report, Part 10, 71 pp.

Torres S., M. Sachidananda, and D. Zrnić, 2005: Signal Design and Processing Techniques for WSR-88D Ambiguity Resolution: Phase coding and staggered PRT. NOAA/NSSL Report, Part 9, 112 pp.

Zrnić, D.S., Melnikov, V.M., and J.K. Carter, 2005: Calibrating differential reflectivity on the WSR-88D. NOAA/NSSL Report, 34 pp.

Torres S., M. Sachidananda, and D. Zrnić, 2004: Signal Design and Processing Techniques for WSR-88D Ambiguity Resolution: Phase coding and staggered PRT: Data collection, implementation, and clutter filtering. NOAA/NSSL Report, Part 8, 113 pp.

Zrnić, D., S. Torres, J. Hubbert, M. Dixon, G. Meymaris, and S. Ellis, 2004: NEXRAD range-velocity ambiguity mitigation. SZ-2 algorithm recommendations. NCAR-NSSL Interim Report.

Melnikov, V, and D Zrnić, 2004: Simultaneous transmission mode for the polarimetric WSR-88D – statistical biases and standard deviations of polarimetric variables. NOAA/NSSL Report, 84 pp.

Bachman, S., 2004: Analysis of Doppler spectra obtained with WSR-88D radar from non-stormy environment. NOAA/NSSL Report, 86 pp.

Zrnić, D., S. Torres, Y. Dubel, J. Keeler, J. Hubbert, M. Dixon, G. Meymaris, and S. Ellis, 2003: NEXRAD range-velocity ambiguity mitigation. SZ(8/64) phase coding algorithm recommendations. NCAR-NSSL Interim Report.

Torres S., D. Zrnić, and Y. Dubel, 2003: Signal Design and Processing Techniques for WSR-88D Ambiguity Resolution: Phase coding and staggered PRT: Implementation, data collection, and processing. NOAA/NSSL Report, Part 7, 128 pp.

Schuur, T., P. Heinselman, and K. Scharfenberg, 2003: Overview of the Joint Polarization Experiment (JPOLE), NOAA/NSSL Report, 38 pp.

Ryzhkov, A, 2003: Rainfall Measurements with the Polarimetric WSR-88D Radar, NOAA/NSSL Report, 99 pp.

Schuur, T., A. Ryzhkov, and P. Heinselman, 2003: Observations and Classification of echoes with the Polarimetric WSR-88D radar, NOAA/NSSL Report, 45 pp.

Melnikov, V., D. Zrnić, R. J. Doviak, and J. K. Carter, 2003: Calibration and Performance Analysis of NSSL's Polarimetric WSR-88D, NOAA/NSSL Report, 77 pp.

NCAR-NSSL Interim Report, 2003: NEXRAD Range-Velocity Ambiguity Mitigation SZ(8/64) Phase Coding Algorithm Recommendations.

Sachidananda, M., 2002: Signal Design and Processing Techniques for WSR-88D Ambiguity Resolution, NOAA/NSSL Report, Part 6, 57 pp.

Doviak, R., J. Carter, V. Melnikov, and D. Zrnić, 2002: Modifications to the Research WSR-88D to obtain Polarimetric Data, NOAA/NSSL Report, 49 pp.

Fang, M., and R. Doviak, 2001: Spectrum width statistics of various weather phenomena, NOAA/NSSL Report, 62 pp.

Sachidananda, M., 2001**:** Signal Design and Processing Techniques for WSR-88D Ambiguity Resolution, NOAA/NSSL Report, Part 5, 75 pp.

Sachidananda, M., 2000**:** Signal Design and Processing Techniques for WSR-88D Ambiguity Resolution, NOAA/NSSL Report, Part 4, 99 pp.

Sachidananda, M., 1999**:** Signal Design and Processing Techniques for WSR-88D Ambiguity Resolution, NOAA/NSSL Report, Part 3, 81 pp.

Sachidananda, M., 1998**:** Signal Design and Processing Techniques for WSR-88D Ambiguity Resolution, NOAA/NSSL Report, Part 2, 105 pp.

Torres, S., 1998: Ground Clutter Canceling with a Regression Filter, NOAA/NSSL Report, 37 pp.

Doviak, R. and D. Zrnić, 1998**:** WSR-88D Radar for Research and Enhancement of Operations: Polarimetric Upgrades to Improve Rainfall Measurements, NOAA/NSSL Report, 110 pp.

Sachidananda, M., 1997**:** Signal Design and Processing Techniques for WSR-88D Ambiguity Resolution, NOAA/NSSL Report, Part 1, 100 pp.

Sirmans, D., D. Zrnić, and M. Sachidananda, 1986**:** Doppler radar dual polarization considerations for NEXRAD, NOAA/NSSL Report, Part I, 109 pp.

Sirmans, D., D. Zrnić, and N. Balakrishnan, 1986**:** Doppler radar dual polarization considerations for NEXRAD, NOAA/NSSL Report, Part II, 70 pp.

Appendix A. Staggered PRT Algorithm Description (July 2010)

A.1. Preface

This document extends the previous Staggered PRT algorithm description from July 2009 by including dual polarization sequences and the calculation of polarimetric variables. This algorithm description includes a high-level description with the overall processing logic followed by a detailed explanation of each pre-computation and processing step.

Most of the July 2009 algorithm steps are now repeated for both H- and V-channels calculation. On the other hand, the SACHI filter has been modified to preserve the spectral phases in order to allow the calculation of polarimetric variables. Now, the output of the SACHI filter produces autocorrelations for both H- and V-channels and also the cross-correlation between them. As with previous versions, most of the steps in the SACHI algorithm are described in algorithmic form to ease implementation and reduce ambiguity. The DC removal ground clutter filter has been retained to operate on those range gates where only long-PRT data is available and ground clutter filtering is needed and now it includes both channels.

As in the July 2009 description, the algorithm is able to handle overlaid echoes, extending the recovery of Doppler moments to the unambiguous range of the long PRT. Moment-specific overlaid power thresholds are used to identify recoverable data and flag unrecoverable Doppler moments. Finally, ground clutter is also assumed to be within the unambiguous range of the short PRT.

A.2. Assumptions

1) The transmission sequence alternates two pulse repetition times (PRT) as: T_1, T_2, T_1, T_2 … for a total of M pulses.

2) The PRT ratio $T_1/T_2 = 2/3$, where $\kappa_m = 2$, $\kappa_n = 3$ and $T_2 - T_1 = T_u$.

3) All range gates are available and there is a perfect alignment of range gates between the two PRTs (i.e., a given range gate represents the same resolution volume in space for every transmitted pulse). Also, the number of range gates for each PRT is: $N_1 = T_1/\tau_s$ and $N_2 = T_2/\tau_s$, where τ_s is the sampling period.

4) There are no significant echoes beyond the maximum unambiguous range corresponding to T_2 (r_{a2}).

5) There is no significant ground clutter beyond the maximum unambiguous range corresponding to T_1 (r_{a1}).

6) The number of staggered PRT samples per range gate (M) is even.

7) The algorithm operates on a radial worth of data at a time.

A.3. Inputs

1) Dual polarization complex time-series data:

$V_H(n, m) = I_H(n, m) + jQ_H(n, m)$,

$V_V(n, m) = I_V(n, m) + jQ_V(n, m)$,

where subscripts H and V denote horizontal and vertical polarization, $0 \leq n < N_1$ for even m, $0 \leq n < N_2$ for odd m and $0 \leq m < M$. Note that n indexes the range gates and m the sweeps (or pulses).

2) Associated metadata:

λ is the radar wavelength in meters
N_H is the noise power in linear units for the horizontal channel
N_V is the noise power in linear units for the vertical channel
dBZ0 is the system calibration constant in dB
ATMOS is the elevation-dependent atmospheric attenuation in dB/km
ΔR is the spacing between range gates in km ($\Delta R = c\tau_s/2$)
T_Z is the signal-to-noise ratio threshold for reflectivity in dB
T_V is the signal-to-noise ratio threshold for velocity in dB
T_W is the signal-to-noise ratio threshold for spectrum width in dB
T_{OV} is the velocity overlaid threshold in dB (*Note: recommended value is 0 dB*)
T_{OW} is the spectrum width overlaid threshold in dB (*Note: recommended value is 10 dB*)

3) Data window:

$d'(m)$, where $0 \leq m < 5M/2$. Note that d' does not need to be normalized or scaled in any way. A tapered data window such as the Blackman window is recommended for best performance of the SACHI ground clutter filter. Otherwise, rectangular window (i.e., no window) should be applied.

4) Ground clutter filter bypass map:

$B(n)$, where n indexes the range bins with the same resolution as the time-series data along a radial, and the map corresponds to the elevation and azimuth of the radial being processed. B is 0 if clutter filtering is required and 1 otherwise. In this algorithm, the clutter map is ignored beyond the unambiguous range corresponding to the short PRT where clutter is assumed not to be present.

A.4. Outputs

1) Reflectivity, Doppler velocity, and spectrum width calculated from H channel data:

$Z(n)$	for $0 \leq n < N_2$,
$v(n)$ and $w(n)$	for $0 \leq n < N_2$.

2) Differential reflectivity, differential phase and correlation coefficient calculated from H and V channel data:

$Z_{DR}(n)$	for $0 \leq n < N_2$,
$\Phi_{DP}(n)$	for $0 \leq n < N_2$,
$\rho_{HV}(n)$	for $0 \leq n < N_2$.

3) Signal-to-noise ratio and overlaid censoring flags*:

$NS_Z(n)$, $NS_V(n)$ and $NS_W(n)$	for $0 \leq n < N_2$,
$OV_V(n)$ and $OV_W(n)$	for $0 \leq n < N_2$.

* $NS_Z(n)$ is used for censoring $Z_{DR}(n)$, $\Phi_{DP}(n)$ and $\rho_{HV}(n)$.

A.5. Functions and Conventions

1) $|\cdot|$ – Returns the absolute value of a complex number or the absolute value of each element of a matrix of complex numbers.

2) arg – Returns the principal phase angle of the input complex number in radians. The algorithm is written to accommodate this phase in the interval $[0, 2\pi)$ or $[-\pi, \pi)$.

3) $\arg\min_k$ – Returns the index k to the element in the input vector that has the minimum value.

4) diag – Returns a square matrix with the input vector along the principal diagonal (row index = column index) of the matrix and all other elements not on the principal diagonal equal to zero. The number of rows (columns) of the matrix is equal to the number of elements in the vector.

5) ceiling – Returns the smallest integer value not less than the input number.

6) floor – Returns the largest integer value not greater than the input number.

7) round – Returns the nearest integer to the input number.

8) max – Returns the maximum value among the input numbers.

9) Italicized names are used to denote scalars (e.g., *Noise*).

10) Bolded names are used to denote vectors or matrices (e.g., **A**). Italicized names with indexing in parentheses are used to denote elements of a vector or matrix [e.g., $A(i,j)$].

11) * – Denotes complex conjugate.

12) T – Denotes matrix transpose.

13) j – Denotes the imaginary unit $\sqrt{-1}$.

A.6. High-level Algorithm description

If first run of SPRT algorithm
1) Pre-computation of velocity dealiasing rules
2) Pre-computation of M-independent SACHI filter parameters

End
If the number of samples (M) changed
3) Pre-computation of window parameters
4) Pre-computation of M-dependent SACHI filter parameters

End
For each range bin n, where $0 \leq n < N_2$
If $n \geq N_1$
5) Short-PRT Segment-III Data Reconstruction

End
If $B(n) = 0$ AND $n < N_1$
6) SACHI Clutter Filtering (Segment-I/II gate with segment-I/II clutter)

Else
If $n \geq N_1$ AND $B(n - N_1) = 0$
7) DC Removal Clutter Filtering (Segment-III gate with segment-I clutter)

Else
8) No Clutter Filtering

End
9) Power and correlation computations for each PRT
10) Combined power and cross-correlation computation

End
End
11) Strong point clutter canceling
For each range bin n, where $0 \leq n < N_2$
12) Signal power computation
13) Reflectivity computation
14) Velocity computation
15) Spectrum width computation
16) Differential reflectivity computation
17) Differential phase computation
18) Cross-correlation coefficient computation
19) Determination of significant returns for reflectivity and polarimetric variables
20) Determination of significant returns for velocity
21) Determination of significant returns for spectrum width

End
For each range bin n, where $0 \leq n < N_2$
22) Determination of overlaid returns for velocity and spectrum width

End

A.7. Step-by-step algorithm description

1) Pre-computation of velocity dealiasing rules

This method is described in the paper "Design, Implementation, and Demonstration of a Staggered PRT Algorithm for the WSR-88D" by Torres et al. (2004). Herein, VDA_c are the normalized velocity difference transfer function (VDTF) constant values and VDA_p are the normalized number of Nyquist co-intervals for dealiasing.

A set of velocity dealiasing rules is pre-computed at the initiation of the SPRT algorithm as follows:

(Compute type-I and II positive VDTF discontinuity points. κ_m and κ_n are the integers in the PRT ratio)
$p = 0$
While $2p + 1 < \kappa_m$
    $D_1(p) = (2p + 1)/\kappa_m$
    $TYPE_1(p) = 1$
    $p = p + 1$
End
$q = 0$
While $2q + 1 < \kappa_n$
    $D_2(q) = (2q + 1)/\kappa_n$
    $TYPE_2(q) = 2$
    $q = q + 1$
End

(Create TYPE by combining and sorting both sets of discontinuity points)
Concatenate D_1 and D_2 to create D with $p + q$ elements.
Concatenate $TYPE_1$ and $TYPE_2$ to create $TYPE$ with $p + q$ elements.
Sort $TYPE$ in a "slave" mode using D as the "master".

(Compute VDTF constants and dealiasing factors for non-negative discontinuity points)
$VDA_c(p + q) = 0$
$VDA_p(p + q) = 0$
For $0 \leq k < p + q$
    If $TYPE(k) = 1$
        $VDA_c(p + q + k + 1) = VDA_c(p + q + k) - 2/\kappa_m$
        $VDA_p(p + q + k + 1) = VDA_p(p + q + k) + 1/\kappa_m$
    Else
        $VDA_c(p + q + k + 1) = VDA_c(p + q + k) + 2/\kappa_n$
        $VDA_p(p + q + k + 1) = VDA_p(p + q + k)$
    End
End

(Compute VDTF constants and dealiasing factors for negative discontinuity points)
For $-(p+q) \le k < 0$
$VDA_c\,(p+q+k) = -VDA_c\,(p+q-k)$
$VDA_p\,(p+q+k) = -VDA_p\,(p+q-k)$
End

(Note that since the PRT ratio does not change, these vectors can be hard-coded in a real-time implementation of the SPRT algorithm.)

2) Pre-computation of *M*-independent SACHI filter parameters

This method is described in NSSL Signal Design and Processing Techniques for WSR-88D Ambiguity Resolution (Report 3, Report 9 and Report 11). The SACHI filter parameters could be pre-computed at the initiation of the SPRT algorithm as follows:

(Create 5-by-5 convolution matrix, $\mathbf{C_r}$*)*

$$\mathbf{C_r} = \begin{bmatrix} C(0) & C(4) & C(3) & C(2) & C(1) \\ C(1) & C(0) & C(4) & C(3) & C(2) \\ C(2) & C(1) & C(0) & C(4) & C(3) \\ C(3) & C(2) & C(1) & C(0) & C(4) \\ C(4) & C(3) & C(2) & C(1) & C(0) \end{bmatrix} = \begin{bmatrix} \mathbf{C}_{\mathbf{r},1} & \mathbf{C}_{\mathbf{r},2} & \mathbf{C}_{\mathbf{r},3} & \mathbf{C}_{\mathbf{r},4} & \mathbf{C}_{\mathbf{r},5} \end{bmatrix},$$

where $C(k) = \frac{1}{\sqrt{10}} \sum_{n=0}^{4} c(n) \exp\left(-j2\pi nk/5\right)$; for $0 \le k < 5$ and **c** = [1, 0, 1, 0, 0], and $\mathbf{C}_{\mathbf{r},k}$ is the *k*-th column of $\mathbf{C_r}$.

(Calculate magnitude deconvolution matrix, $\mathbf{C_{md}}$*)*
(Note: The following formulas are written in matrix algebra notation with the conventions described above)

$$\mathbf{C_{md}} = \left|\mathbf{C_r}\right|^{-1} = \begin{bmatrix} \mathbf{C}_{\mathbf{md},1} \\ \mathbf{C}_{\mathbf{md},2} \\ \mathbf{C}_{\mathbf{md},3} \\ \mathbf{C}_{\mathbf{md},4} \\ \mathbf{C}_{\mathbf{md},5} \end{bmatrix} = \begin{bmatrix} -4.6281 & -2.0697 & 4.6281 & 4.6281 & -2.0697 \\ -2.0697 & -4.6281 & -2.0697 & 4.6281 & 4.6281 \\ 4.6281 & -2.0697 & -4.6281 & -2.0697 & 4.6281 \\ 4.6281 & 4.6281 & -2.0697 & -4.6281 & -2.0697 \\ -2.0697 & 4.6281 & 4.6281 & -2.0697 & -4.6281 \end{bmatrix},$$

where $\mathbf{C}_{\mathbf{md},k}$ is the *k*-th row of $\mathbf{C_{md}}$.

(Calculate matrices $\mathbf{C_{f1}}$ *and* $\mathbf{C_{f2}}$ *using* 1^{st} *and* 5^{th} *columns of* $\mathbf{C_r}$*)*

$$\mathbf{C_{f1}} = \mathbf{C}_{\mathbf{r},1}\mathbf{C}_{\mathbf{r},1}^{*T} = \begin{bmatrix} 0.4 & 0.0382 + j0.1176 & 0.2618 - j0.1902 & 0.2618 + j0.1902 & 0.0382 - j0.1176 \\ 0.0382 - j0.1176 & 0.0382 & -0.0309 - j0.0951 & 0.0809 - j0.0588 & -0.0309 - j0.0225 \\ 0.2618 + j0.1902 & -0.0309 + j0.0951 & 0.2681 & 0.0809 + j0.2490 & 0.0809 - j0.0588 \\ 0.2618 - j0.1902 & 0.0809 + j0.0588 & 0.0809 - j0.2490 & 0.2618 & -0.0309 - j0.0951 \\ 0.0382 + j0.1176 & -0.0309 + j0.0225 & 0.0809 + j0.0588 & -0.0309 + j0.0951 & 0.0382 \end{bmatrix}$$

$$\mathbf{C_{f2}} = \mathbf{C}_{\mathbf{r},5}\mathbf{C}_{\mathbf{r},5}^{*T} = \begin{bmatrix} 0.0382 & -0.0309 - j0.0951 & 0.0809 - j0.0588 & -0.0309 - j0.0225 & 0.0382 - j0.1176 \\ -0.0309 + j0.0951 & 0.2618 & 0.0809 + j0.249 & 0.0809 - j0.0588 & 0.2618 + j0.1902 \\ 0.0809 + j0.0588 & 0.0809 - j0.249 & 0.2618 & -0.0309 - j0.0951 & 0.2618 - j0.1902 \\ -0.0309 + j0.0225 & 0.0809 + j0.0588 & -0.0309 + j0.0951 & 0.0382 & 0.0382 + j0.1176 \\ 0.0382 + j0.1176 & 0.2618 - j0.1902 & 0.2618 + j0.1902 & 0.0382 - j0.1176 & 0.4 \end{bmatrix}$$

where **T* stands for the matrix conjugate transpose (a.k.a. Hermitian) operation.
(Calculate the correction coefficients ξ_2 and ξ_3 *for correction vector* **X***)*

$$\xi_k = \frac{1}{\mathbf{C}_{\mathbf{md},1}\left|\mathbf{C}_{\mathbf{r},k} - \left(\mathbf{C}_{\mathbf{r},1}^{*T}\mathbf{C}_{\mathbf{r},k}\right)\mathbf{C}_{\mathbf{r},1}\right|}; k = 2, 3.$$

$\xi_2 = 1.1056$ and $\xi_3 = 1.7889$.

(Note: since the PRT ratio does not change, these matrices and coefficients can be hard-coded in a real-time implementation of the SPRT algorithm. The numbers provided here are for reference purposes only; the highest precision available is recommended for hard-coding these numbers.)

3) Pre-computation of window parameters

(Calculate the extended number of coefficients)
$M_x = 5M / 2$

(Calculate the number of pulse pairs)
$M_p = M / 2$

(Calculate normalized window d for un-normalized window function d' with M_x points)

$$d(m) = d'(m)\left(\sqrt{\frac{1}{M_x}\sum_{m=0}^{M_x-1}\left[d'(m)\right]^2}\right)^{-1};\ 0 \le m < M_x.$$

(Calculate window correction factor for lag-1)

$$d_c = \frac{1}{M_x}\sum_{m=0}^{M_x-2} d(m)d(m+1)$$

4) Pre-computation of *M*-dependent SACHI filter parameters

(Compute correction vector, **X***)*
For $0 \le k <$ ceiling(M_p/2)
  $X(k) = 1$
End
For ceiling(M_p/2) $\le k <$ ceiling(M_p/2) + M_p
  $X(k) = \xi_2$
End
For ceiling(M_p/2) + $M_p \le k <$ ceiling(M_p/2) + $3M_p$
  $X(k) = \xi_3$
End
For ceiling(M_p/2) + $3M_p \le k <$ ceiling(M_p/2) + $4M_p$
  $X(k) = \xi_2$
End
For ceiling(M_p/2) + $4M_p \le k < M_x$
  $X(k) = 1$
End

A.8. Processing steps

5) Short-PRT Segment-III Data Reconstruction

Long-PRT Segment-I data is used as a proxy for short-PRT segment-III data

For $0 \le m < M_p$
$V_H(n, 2m) = V_H(n - N_1, 2m + 1)$
$V_V(n, 2m) = V_V(n - N_1, 2m + 1)$
End

6) SACHI Clutter Filtering

The SACHI filter algorithm is used when clutter filtering is required inside the maximum unambiguous range corresponding to T_1 (r_{a1}).

(Form derived time series, V_{Hd} and V_{Vd}, from input time series V_H and V_V)
For $0 \le m < M_p$
$V_{Hd}(5m) = V_H(n, 2m)$
$V_{Hd}(5m + 1) = 0$
$V_{Hd}(5m + 2) = V_H(n, 2m + 1)$
$V_{Hd}(5m + 3) = 0$
$V_{Hd}(5m + 4) = 0$

$V_{Vd}(5m) = V_V(n, 2m)$
$V_{Vd}(5m + 1) = 0$
$V_{Vd}(5m + 2) = V_V(n, 2m + 1)$
$V_{Vd}(5m + 3) = 0$
$V_{Vd}(5m + 4) = 0$
End

(Compute DFT of windowed extended time series power compensated for added zeroes)

$$F_H(k) = \left(\sqrt{\frac{5}{2}}\right)\left(\frac{1}{M_x}\sum_{m=0}^{M_x-1} V_{Hd}(m)d(m)\exp(-j2\pi km/M_x)\right); k = 0, 1 \ldots, M_x - 1.$$

$$F_V(k) = \left(\sqrt{\frac{5}{2}}\right)\left(\frac{1}{M_x}\sum_{m=0}^{M_x-1} V_{Vd}(m)d(m)\exp(-j2\pi km/M_x)\right); k = 0, 1 \ldots, M_x - 1.$$

(Determine clutter filter width parameter, q)
(Use GMAP to return the number of coefficients identified as clutter, $GMAP_{Hcoef}$ and $GMAP_{Vcoeff}$. Pass to GMAP the 5th of the Doppler spectrum containing the main clutter replica; i.e., $|F_{\{H,V\}}(0)|^2, \ldots, |F_{\{H,V\}}[\text{ceiling}(M_p/2) - 1]|^2, |F_{\{H,V\}}[M_x - \text{floor}(M_p/2)]|^2, \ldots, |F_{\{H,V\}}(M_x - 1)|^2\}$*; initialize GMAP for spectra with* $v_a/5$, *and*

get the number of coefficients identified as clutter to estimate q for both H and V channels)
$q_H = floor\ [(GMAP_{Hcoef} + 1)/2]$
$q_V = floor\ [(GMAP_{Vcoef} + 1)/2]$

(Use the largest q to create the clutter filter vectors for polarimetric variable calculation)
$q' = max(q_H, q_V)$
(Create clutter filter vectors I_{f1}',I_{f2}')
For $0 \le k < M_p$
  If $k < q'$
    $I_{f1}'(k) = 1$
    $I_{f2}'(k) = 0$

  ElseIf $k \le M_p - q'$
    $I_{f1}'(k) = 0$
    $I_{f2}'(k) = 0$
  Else
    $I_{f1}'(k) = 0$
    $I_{f2}'(k) = 1$
  End
End

(Row-wise re-arrange F_H and F_V into 5-by-M_p matrices, $\mathbf{F_{Hr}}$ and $\mathbf{F_{Vr}}$*)*
For $0 \le k < M_p$
  $F_{Hr}(0, k) = F_H(k)$
  $F_{Hr}(1, k) = F_H(k + M_p)$
  $F_{Hr}(2, k) = F_H(k + 2M_p)$
  $F_{Hr}(3, k) = F_H(k + 3M_p)$
  $F_{Hr}(4, k) = F_H(k + 4M_p)$

  $F_{Vr}(0, k) = F_V(k)$
  $F_{Vr}(1, k) = F_V(k + M_p)$
  $F_{Vr}(2, k) = F_V(k + 2M_p)$
  $F_{Vr}(3, k) = F_V(k + 3M_p)$
  $F_{Vr}(4, k) = F_V(k + 4M_p)$
End

(Compute the clutter filtered spectrum matrices, $\mathbf{F_{Hf}}$ and $\mathbf{F_{Vf}}$*)*
(Note: The following formulas are written in matrix algebra notation. Complex-matrix multiplications can be implemented using four real-matrix multiplications as: $\mathbf{AB} = (\mathbf{A_r} + j\mathbf{A_i})(\mathbf{B_r} + j\mathbf{B_i}) = (\mathbf{A_rB_r} - \mathbf{A_iB_i}) + j(\mathbf{A_rB_i} + \mathbf{A_iB_r})$ *)*

$$\mathbf{F}_{\mathrm{Hf}} = \mathbf{F}_{\mathrm{Hr}} - \mathbf{C_{f1}}\mathrm{F}_{\mathrm{Hr}}\,\mathrm{diag}\left(\mathbf{I_{f1}}'\right) - \mathbf{C_{f2}}\mathbf{F}_{\mathrm{Hr}}\,\mathrm{diag}\left(\mathbf{I_{f2}}'\right)$$
$$\mathbf{F}_{\mathrm{Vf}} = \mathrm{F}_{\mathrm{Vr}} - \mathbf{C_{f1}}\mathbf{F}_{\mathrm{Vr}}\,\mathrm{diag}\left(\mathbf{I_{f1}}'\right) - \mathbf{C_{f2}}\mathbf{F}_{\mathrm{Vr}}\,\mathrm{diag}\left(\mathbf{I_{f2}}'\right)$$

(Row-wise unfold $\mathbf{F_{Hf}}$ *and* $\mathbf{F_{Vf}}$ *into* F_{Hdf} *and* F_{Vdf}*)*

For $0 \le k < M_p$

$F_{Hdf}(k) = F_{Hf}(0, k)$

$F_{Hdf}(k + M_p) = F_{Hf}(1, k)$

$F_{Hdf}(k + 2M_p) = F_{Hf}(2, k)$

$F_{Hdf}(k + 3M_p) = F_{Hf}(3, k)$

$F_{Hdf}(k + 4M_p) = F_{Hf}(4, k)$

$F_{Vdf}(k) = F_{Vf}(0, k)$

$F_{Vdf}(k + M_p) = F_{Vf}(1, k)$

$F_{Vdf}(k + 2M_p) = F_{Vf}(2, k)$

$F_{Vdf}(k + 3M_p) = F_{Vf}(3, k)$

$F_{Vdf}(k + 4M_p) = F_{Vf}(4, k)$

End

(Compute power for both channels, P_H*' and* P_V*, and cross-corr at lag 0,* $R_{HV}(0)$*)*

$$P'_H(n) = \sum_{k=0}^{M_x-1} \left| F_{Hdf}(k) \right|^2$$

$$P_V(n) = \sum_{k=0}^{M_x-1} \left| F_{Vdf}(k) \right|^2$$

$$R_{HV}(n) = \sum_{k=0}^{M_x-1} F^*_{Hdf}(k) \cdot F_{Vdf}(k)$$

(Proceed with the conventional SACHI Clutter Filtering, only H-channel data)

$q = q_H$

If $q < q'$

(Create clutter filter vectors I_{f1}*,* I_{f2}*)*

For $0 \le k < M_p$

If $k < q$

$I_{f1}(k) = 1$

$I_{f2}(k) = 0$

ElseIf $k \le M_p - q$

$I_{f1}(k) = 0$

$I_{f2}(k) = 0$

Else

$I_{f1}(k) = 0$

$I_{f2}(k) = 1$

End

End

$$\mathbf{F_f} = \mathbf{F}_{\mathrm{Hr}} - \mathbf{C_{f1}}\mathbf{F}_{\mathrm{Hr}}\,\mathrm{diag}(\mathbf{I_{f1}}) - \mathbf{C_{f2}}\mathbf{F}_{\mathrm{Hr}}\,\mathrm{diag}(\mathbf{I_{f2}})$$

Else

$$\mathbf{F_f} = \mathbf{F}_{\mathrm{Hf}}$$

End

(Create clutter filter vectors, $\mathbf{I_1}$*, and* $\mathbf{I_2}$*)*

For $0 \le k < M_p$

  If $k < q$

    $I_1(k) = 0$

    $I_1(k + M_p) = 0$

    $I_1(k + 2M_p) = 0$

    $I_1(k + 3M_p) = 0$

    $I_1(k + 4M_p) = 0$

    $I_2(k) = 1$

    $I_2(k + M_p) = 1$

    $I_2(k + 2M_p) = 1$

    $I_2(k + 3M_p) = 1$

    $I_2(k + 4M_p) = 1$

  ElseIf $k \le M_p - q$

    $I_1(k) = 1$

    $I_1(k + M_p) = 1$

    $I_1(k + 2M_p) = 1$

    $I_1(k + 3M_p) = 1$

    $I_1(k + 4M_p) = 1$

    $I_2(k) = 0$

    $I_2(k + M_p) = 0$

    $I_2(k + 2M_p) = 0$

    $I_2(k + 3M_p) = 0$

    $I_2(k + 4M_p) = 0$

  Else

    $I_1(k) = 0$

    $I_1(k + M_p) = 0$

    $I_1(k + 2M_p) = 0$

    $I_1(k + 3M_p) = 0$

    $I_1(k + 4M_p) = 0$

    $I_2(k) = 1$

    $I_2(k + M_p) = 1$

    $I_2(k + 2M_p) = 1$

    $I_2(k + 3M_p) = 1$

    $I_2(k + 4M_p) = 1$

  End

End

(Magnitude deconvolved matrix, $\mathbf{F_d}$*)*

$$\mathbf{F_d} = \mathbf{C_{md}} \left| \mathbf{F_f} \right|$$

(Row-wise unfold $\mathbf{F_d}$ *into* F_{df}*)*
For $0 \le k < M_p$
$F_{df}(k) = F_d(0, k)$
$F_{df}(k + M_p) = F_d(1, k)$
$F_{df}(k + 2M_p) = F_d(2, k)$
$F_{df}(k + 3M_p) = F_d(3, k)$
$F_{df}(k + 4M_p) = F_d(4, k)$
End

*(Compute the lag-*1 *autocorrelation,* R_{1df}*)*

$$R_{1df} = \frac{1}{d_c} \sum_{k=0}^{M_x - 1} \left| F_{df}(k) \right|^2 \exp\left(j 2\pi k / M_x \right)$$

(Compute vector $\mathbf{I_v}$ *with M/*2 *ones centered on* $\arg(R_{1df})$*)*
(Round to the nearest spectral coefficient. Choose symmetric window of coefficients around it)

$$k_{0df} = \text{round}\left[\frac{M_x \arg\left(R_{1df} \right)}{2\pi} \right]$$

If $k_{0df} < 0$
$k_{0df} = k_{0df} + M_x$
End
If $k_{0df} \ge M_x$
$k_{0df} = k_{0df} - M_x$
End
$k_{1df} = k_{0df} - \text{floor}(M / 4)$
If $k_{1df} < 0$
$k_{1df} = k_{1df} + M_x$
End
$k_{2df} = k_{0df} + \text{ceiling}(M / 4) - 1$
If $k_{2df} \ge M_x$
$k_{2df} = k_{2df} - M_x$
End

(k_{0df} *is the coefficient corresponding to* $\arg(R_{1df})$*,* k_{1df} *and* k_{2df} *specify the extent of* M_p *spectral coefficients centered on the mean velocity. If* $k_{1df} < k_{2df}$*, the ones span from* k_{1df} *to* k_{2df}*; otherwise, the ones will span from* k_{1df} *to* $M_x - 1$*, and 0 to* k_{2df}*)*
If $k_{1df} < k_{2df}$
For $0 \le k < M_x$
If $k < k_{1df}$ OR $k > k_{2df}$
$I_v(k) = 0$
Else
$I_v(k) = 1$
End
End

Else
  For $0 \le k < M_x$
    If $k < k_{1df}$ AND $k > k_{2df}$
      $I_v(k) = 0$
    Else
      $I_v(k) = 1$
    End
  End
End

(Interpolate the elements for the region around zero velocity in F_{df} with linearly interpolated values from S_1 and S_2)
If $q > 0$
  $S_1 = \left|F_{df}(q)\right|^2$
  $S_2 = \left|F_{df}(M_x - q)\right|^2$
  For $0 \le k < M_x$
    If $k < q$
      $F_i(k) = \left[S_2 + (S_1 - S_2)(q + k) / 2q\right]^{1/2}$
    ElseIf $k > M_x - q$
      $F_i(k) = \left[S_2 + (S_1 - S_2)(q + k - M_x) / 2q\right]^{1/2}$
    Else
      $F_i(k) = F_{df}(k)$
    End
  End
Else
  (Don't interpolate if not needed)
  For $0 \le k < M_x$
    $F_i(k) = F_{df}(k)$
  End
End

(Compute the corrected spectrum, F_c)
For $0 \le k < M_x$
  $F_c(k) = F_i(k)\, I_1(k) + F_i(k)\, I_2(k)\, I_v(k)\, X(k)$
End

(Compute vector $\mathbf{I_c}$ with ones where there's a non-zero spectral component in vector $\mathbf{F_c}$)
For $0 \le k < M_x$
  $I_c(k) = I_1(k) + I_2(k)\, I_v(k)$
End

(Compute the mean power, P_c, and autocorrelation at lag T_u, R_{1c}, using F_c)

$$P_c = \sum_{k=0}^{M_x-1} \left|F_c(k)\right|^2$$

$$R_{1c} = \frac{1}{d_c} \sum_{k=0}^{M_x-1} \left|F_c(k)\right|^2 \exp\left(j2\pi k/M_x\right)$$

(Retain only M coefficients centered on velocity based on R_{1c} and delete the rest from F_c and I_c)

$$k_{0c} = \text{round}\left[\frac{M_x \arg\left(R_{1c}\right)}{2\pi}\right]$$

If $k_{0c} < 0$
  $k_{0c} = k_{0c} + M_x$
End
If $k_{0c} \geq M_x$
  $k_{0c} = k_{0c} - M_x$
End
$k_{1c} = k_{0c} - M_p$
If $k_{1c} < 0$
  $k_{1c} = k_{1c} + M_x$
End
$k_{2c} = k_{0c} + M_p - 1$
If $k_{2c} \geq M_x$
  $k_{2c} = k_{2c} - M_x$
End
If $k_{1c} < k_{2c}$
  For $0 \leq k < M_x$
    If $k < k_{1c}$ OR $k > k_{2c}$
      $F_m(k) = 0$
      $I_m(k) = 0$
    Else
      $F_m(k) = F_c(k)$
      $I_m(k) = I_c(k)$
    End
  End
Else
  For $0 \leq k < M_x$
    If $k < k_{1c}$ AND $k > k_{2c}$
      $F_m(k) = 0$
      $I_m(k) = 0$
    Else
      $F_m(k) = F_c(k)$
      $I_m(k) = I_c(k)$
    End
  End
End

(Compute the modified mean power, P_m, and autocorrelation at lag T_u, R_{1m}, using F_m)

$$P_m = \sum_{k=0}^{M_x-1} \left|F_m(k)\right|^2$$

$$R_{1m} = \frac{1}{d_c} \sum_{k=0}^{M_x-1} \left|F_m(k)\right|^2 \exp\left(j2\pi k/M_x\right)$$

(Compute noise correction factors)

$$N_c = \frac{1}{M_x} \sum_{k=0}^{M_x-1} I_c(k)$$

$$N_m = \frac{1}{M_x} \sum_{k=0}^{M_x-1} I_m(k)$$

(Compute overlaid power correction if in segment I)

If $n < N_2 - N_1$

$$S_{ov} = \frac{1}{2}\left[\frac{1}{M_p} \sum_{m=0}^{M_p-1} \left|V_H\left(n+N_1, 2m+1\right)\right|^2 - Noise\right]$$

If $S_{ov} < 0$

$S_{ov} = 0$

End

Else

$S_{ov} = 0$

End

(Correct powers to remove overlaid contamination adjusted for each spectrum)

$P_m = P_m - N_m S_{ov}$

If $P_m < 0$

$P_m = 0$

End

$P_c = P_c - N_c S_{ov}$

If $P_c < 0$

$P_c = 0$

End

(Compute spectrum width power ratio adjustment)

$S_m = P_m - N_m Noise$

If $S_m < 0$

$S_m = 0$

End

If $S_m > 0$

$$P_{adj} = \frac{\left|R_{1m}\right|}{S_m}$$

Else

$P_{adj} = 0$

End

(Compute signal power)

$S_c = P_c - N_c Noise$

If $S_c < 0$

$S_c = 0$

End

(Compute short PRT autocorrelation at lag T_1)

$$R_{H1}(n) = S_c \cdot P_{adj}^4 \exp\left[j2\arg\left(R_{1c}\right)\right]$$

(Compute long PRT autocorrelation at lag T_2)

$$R_{H2}(n) = S_H \cdot P_{adj}^9 \exp\left[j3\arg\left(R_{1c}\right)\right]$$

(Adjust signal power to include noise)

$P_H(n) = S_c + Noise$

(Note that the outputs of SACHI are $P'_H(n)$, $P_V(n)$, $R_{HV}(n)$, $P_H(n)$, $R_{H1}(n)$ and $R_{H2}(n)$)

7) DC Removal Clutter Filtering (Segment-III gate with segment-I clutter)

This DC Removal clutter filtering algorithm removes the mean (DC) component of the short-PRT segment-III gates in those locations where the site-dependent clutter filter bypass map *B* indicates the need for clutter within segment I.

(Calculate the mean of the even pulses.)

$$V_{Hm} = \frac{1}{M_p} \sum_{m=0}^{M_p - 1} V_H(n, 2m)$$

$$V_{Vm} = \frac{1}{M_p} \sum_{m=0}^{M_p - 1} V_V(n, 2m)$$

(Subtract mean from even pulses.)

For $0 \le m < M_p$

$V_{HF}(2m) = V_H(n, 2m) - V_{Hm}$

$V_{HF}(2m + 1) = V_H(n, 2m + 1)$

$V_{VF}(2m) = V_V(n, 2m) - V_{Vm}$

$V_{VF}(2m + 1) = V_V(n, 2m + 1)$

End

8) No Clutter Filtering

For $0 \leq m < M$

$V_{HF}(m) = V_H(n, m)$

$V_{VF}(m) = V_V(n, m)$

End

9) Power and correlation computations for each PRT

If $n < N_1$

(Compute power from even pulses, if available)

$$P_{H1} = \frac{1}{M_p} \sum_{m=0}^{M_p - 1} \left| V_{HF}(2m) \right|^2$$

$$P_{V1} = \frac{1}{M_p} \sum_{m=0}^{M_p - 1} \left| V_{VF}(2m) \right|^2$$

(Compute cross-correlation from even pulses, if available)

$$R_{HV1}(n) = \frac{1}{M_p} \sum_{m=0}^{M_p - 1} V_{HF}^*(2m) V_{VF}(2m)$$

End

(Compute power from odd pulses)

$$P_{H2} = \frac{1}{M_p} \sum_{m=0}^{M_p - 1} \left| V_{HF}(2m+1) \right|^2$$

$$P_{V2} = \frac{1}{M_p} \sum_{m=0}^{M_p - 1} \left| V_{VF}(2m+1) \right|^2$$

(Compute cross-correlation from odd pulses)

$$R_{HV2}(n) = \frac{1}{M_p} \sum_{m=0}^{M_p - 1} V_{HF}^*(2m+1) V_{VF}(2m+1)$$

(Compute lag-1 correlations from all pulses from H channel)

$$R_{H1}(n) = \frac{1}{M_p} \sum_{m=0}^{M_p - 1} V_{HF}^*(2m) V_{HF}(2m+1)$$

$$R_{H2}(n) = \frac{1}{M_p - 1} \sum_{m=0}^{M_p - 2} V_{HF}^*(2m+1) V_{HF}(2m+2)$$

10) Combined power and cross-correlation computation

To use as much information as possible, data are extracted from the two power arrays with different rules for each of the three segments depicted in Figure A.1. For segment I, data are extracted only from P_1, since P_2 may be contaminated on those range bins with

overlaid powers. An average of P_1 and P_2 is extracted for segment II, given that both power vectors are "clean" there. Finally, segment IḭI data are obtained from P_2. In algorithmic form:

If $n < N_2 - N_1$
(Segment I)
$P_H(n) = P_{H1}$
$P_V(n) = P_{V1}$
ElseIf $n < N_1$
(Segment II)
$P_H(n) = \frac{1}{2}\left(P_{H1} + P_{H2}\right)$
$P_V(n) = \frac{1}{2}\left(P_{V1} + P_{V2}\right)$
Else
(Segment III)
$P_H(n) = P_{H2}$
$P_V(n) = P_{V2}$
End
$P'_H(n) = P_H$

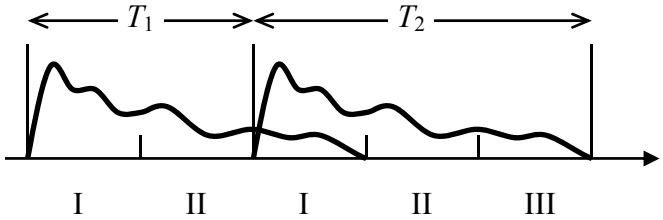

Fig. A.1. Signal powers in the staggered PRT algorithm. Roman numerals indicate segment numbers.

The same rules apply for the cross-correlation computation.

If $n < N_2 - N_1$
(Segment I)
$R_{HV}(n) = R_{HV1}$
ElseIf $n < N_1$
(Segment II)
$R_{HV}(n) = \frac{1}{2}\left(R_{HV1} + R_{HV2}\right)$
Else
(Segment III)
$R_{HV}(n) = R_{HV2}$
End

11) Strong point clutter canceling

Processing is as in the current system. Strong-point clutter canceling is applied to P_H, P'_H, R_{H1} and R_{H2} based on radial power continuity in P_H. For the remainder of the algorithm it is assumed that the outputs of this step are P_H, P'_H, R_{H1} and R_{H2}.

12) Signal power computation

If $P_H(n) < N_H$
  $S_H = 0$
Else
  $S_H = P_H(n) - N_H$
End

If $P'_H(n) < N_H$
  $S'_H = 0$
Else
  $S'_H = P_H'(n) - N_H$
End

If $P_V(n) < N_V$
  $S_V = 0$
Else
  $S_V = P_V(n) - N_V$
End

13) Reflectivity computation

(Range in km)
$R = n\Delta R + \Delta R/2$
(Reflectivity in dBZ. $\log_{10}$ *is the base-*10 *logarithm)*
If $S_H > 0$
  $Z(n) = 10\log_{10}(S_H) + dBZ0 + R\,ATMOS + 20\log_{10}(R) - 10\log_{10}(N_H)$,
Else
  $Z(n)$ should be set to the smallest possible reflectivity value
End

14) Velocity computation

(Compute Doppler velocities for each PRT using the corresponding correlation estimates)

$$v_1 = -\frac{\lambda}{4\pi T_1}\arg\left[R_{H1}(n)\right]$$

$$v_2 = -\frac{\lambda}{4\pi T_2}\arg\left[R_{H2}(n)\right]$$

(Compute extended Nyquist velocity)

$$v_a = \frac{\lambda}{2T_1}$$

(Dealias velocity using pre-computed rules)

$$l = \arg\min_k \left| v_1 - v_2 - VDA_c(k) v_a \right|$$

$$v(n) = v_1 + 2v_a \; VDA_p(l)$$

(Prevent dealiased velocities outside of the extended Nyquist co-interval)

If $v(n) > v_a$

$$v(n) = v(n) - 2v_a$$

End

If $v(n) < -v_a$

$$v(n) = v(n) + 2v_a$$

End

15) Spectrum width computation

The spectrum width estimator corresponds to the algorithm implemented in the legacy WSR-88D signal processor.

If $S_H = 0$ OR $\left| R_{H1}(n) \right| = 0$

(Insert spectrum width of white noise)

$$w(n) = \frac{\lambda}{4\sqrt{3}T_1}$$

ElseIf $S_H < \left| R_{H1}(n) \right|$

(Insert spectrum width of a constant)

$$w(n) = 0$$

Else

(Spectrum width computation. ln *is the natural logarithm)*

$$w(n) = \frac{\lambda}{2\sqrt{2}\pi T_1} \sqrt{\ln\left(\frac{S}{\left| R_{H1}(n) \right|} \right)}$$

If $w(n) > \frac{\lambda}{4\sqrt{3}T_1}$

$$w(n) = \frac{\lambda}{4\sqrt{3}T_1}$$

End

End

16) Differential reflectivity computation

If $S'_H > 0$ AND $S_V > 0$

$$Z_{DR}(n) = 10\log_{10}\frac{S'_H}{S_V}$$

ElseIf $S'_H = 0$

$Z_{DR}(n)$ should be set to the smallest possible value

ElseIf $S_V = 0$

$Z_{DR}(n)$ should be set to the highest possible value

End

17) Differential phase computation

$$\Phi_{DP}(n) = \arg\left[R_{HV}(n)\right]$$

18) Cross-correlation coefficient computation

If $S'_H > 0$ AND $S_V > 0$

$$\rho_{HV}(n) = \frac{\left|R_{HV}(n)\right|}{\sqrt{S'_H S_V}}$$

Else

$\rho_{HV}(n) = 0$

End

19) Determination of significant returns for reflectivity and polarimetric variables

The non-significant return indicator array (NS_Z) is a binary array where 0 indicates "significant" and 1 indicates "non-significant". This array is also used for $Z_{DR}(n)$, $\Phi_{DP}(n)$ and $\rho_{hv}(n)$.

If $S_H < N_H \cdot 10^{0.1T_Z}$

$NS_Z(n) = 1$

Else

$NS_Z(n) = 0$

End

20) Determination of significant returns for velocity

The non-significant return indicator array (NS_V) is a binary array where 0 indicates "significant" and 1 indicates "non-significant"

If $S_H < N_H \cdot 10^{0.1T_V}$
    $NS_V(n) = 1$
Else
    $NS_V(n) = 0$
End

21) Determination of significant returns for spectrum width

The non-significant return indicator array (NS_W) is a binary array where 0 indicates "significant" and 1 indicates "non-significant"

If $S_H < N_H \cdot 10^{0.1T_W}$
    $NS_W(n) = 1$
Else
    $NS_W(n) = 0$
End

22) Determination of overlaid returns for velocity and spectrum width

Censoring of velocity and spectrum width data is only necessary in segments I and III. This is done by analyzing P in segment I (P_1) and P in segment III (P_2) (see Fig. 1). The idea is to determine whether second trip signals mask first trip signals and vice versa. While such overlaid echoes appear in every other pulse and do not bias velocity estimates at those range locations, overlaid powers act as noise. Therefore, when overlaid powers are above a preset fraction of their non-overlaid counterparts, the corresponding velocity and spectrum width estimates exhibit very large errors and must be censored. The overlaid indicator arrays (OV_V and OV_W) are binary arrays where 0 indicates "not overlaid" and 1 indicates "overlaid".

If $n < N_2 - N_1$
    (Segment I: Range gates that may or may not have overlaid echoes)
    (Check power ratio using velocity threshold)
    If $P_H(n) > P_H(n + N_1)\ 10^{0.1T_{OV}}$
        $OV_V(n) = 0$
    Else
        (Power ratio not met, but consider non-significant returns as non-existent)
        If $NS_V(n + N_1) = 1$
            $OV_V(n) = 0$
        Else
            $OV_V(n) = 1$
        End

End
(Check power ratio using width threshold)
If $P_H(n) > P_H(n + N_1)\ 10^{0.1T_{OW}}$
$OV_W(n) = 0$
Else
(Power ratio not met, but consider non-significant returns as non-existent)
If $NS_W(n + N_1) = 1$
$OV_W(n) = 0$
Else
$OV_W(n) = 1$
End
End
ElseIf $n < N_1$
(Segment II: Range gates that, based on the assumptions, never have overlaid echoes)
$OV_V(n) = 0$
$OV_W(n) = 0$
Else
(Segment III: Range gates that may or may not have overlaid echoes)
(Check power ratio using velocity threshold)
If $P_H(n) > P_H(n - N_1)\ 10^{0.1T_{OV}}$
$OV_V(n) = 0$
Else
(Power ratio not met, but consider non-significant returns as non-existent)
If $NS_V(n - N_1) = 1$
$OV_V(n) = 0$
Else
$OV_V(n) = 1$
End
End
(Check power ratio using width threshold)
If $P_H(n) > P_H(n - N_1)\ 10^{0.1T_{OW}}$
$OV_W(n) = 0$
Else
(Power ratio not met, but consider non-significant returns as non-existent)
If $NS_W(n - N_1) = 1$
$OV_W(n) = 0$
Else
$OV_W(n) = 1$
End
End
End
(Note that when processing the overlaid and significant return flags, the overlaid flags take a lower priority. That is, if a range bin is tagged as non-significant and also as overlaid, the overlaid indication is ignored and the gate is treated as a non-significant return only; e.g., painted black as opposed to purple)

Appendix B. Related Publications

The following conference paper relates to the reported material on CLEAN-AP and follows in its original form.

Warde, D., and S. Torres, 2009: Automatic detection and removal of ground clutter contamination on weather radars. Preprints, *34th Int. Conf. on Radar Meteor.*, Williamsburg, VA. Amer. Meteor. Soc., Paper P10.11.

P10.11 AUTOMATIC DETECTION AND REMOVAL OF GROUND CLUTTER CONTAMINATION ON WEATHER RADARS

David A. Warde* and Sebastián M. Torres
Cooperative Institute for Mesoscale Meteorological Studies, The University of Oklahoma, and
NOAA/OAR National Severe Storms Laboratory, Norman, Oklahoma

1. INTRODUCTION

Radar backscatter from the ground can contaminate weather signals, often resulting in severely biased meteorological estimates. If not removed, these clutter returns tend to bias reflectivity high as well as Doppler velocity and spectrum width toward zero. A ground clutter filter (GCF) can mitigate this contamination and provide unbiased meteorological estimates but typically with reduced quality. Moreover, significant biases could occur if the GCF is applied when clutter is not present and the weather signal has near-zero Doppler velocities. Thus, the overall quality of the meteorological estimates needlessly suffers when a GCF is misapplied. The problem of applying the GCF becomes very complex, especially when considering the dynamic nature of the atmosphere. Anomalous propagation can cause the radar beam to increase contact or overshoot the clutter, giving the appearance that the clutter shifts within or disappears from the radar volume coverage very rapidly. In this dynamic environment, spectral examination of the received echoes provides a means to determine the presence of clutter in real time without having to rely on static clutter maps. However, spectral analysis on a finite number of samples suffers from spectral leakage. To combat spectral leakage, tapered windows are typically applied. Strong clutter returns may require the use of windows with high dynamic ranges, but the use of these windows reduces the quality and resolution of the meteorological estimates. On the other hand, weaker clutter returns may only require low dynamic range windows, which help preserve the quality and resolution of the meteorological estimates. Consequently, a 'smart' filter is needed that can examine the received radar echoes, apply a tapered window that best suits the conditions, determine the exact number of spectral coefficients affected by clutter contamination, and, only then, apply the GCF.

In this paper, we introduce a spectral GCF capable of satisfying the aforementioned considerations. The filter is referred to as Clutter Environment ANalysis using Adaptive Processing (CLEAN-AP) and performs real-time detection and suppression of ground clutter returns in dynamic atmospheric environments. We characterize the statistical performance of the CLEAN-AP filter with simulated clutter/weather mix and show real weather examples.

* Corresponding Author Address: David A. Warde, CIMMS/University of Oklahoma, National Severe Storms Laboratory, National Weather Center, 120 David L. Boren Blvd. Norman, OK, 73072; David.A.Warde@noaa.gov

2. GROUND CLUTTER FILTERING

The effects of ground clutter contamination on meteorological estimates are well understood. Ground clutter is characterized as having strong received power with a very narrow spectrum width and near zero velocity (Doviak and Zrnić 1993, Sirmans 1987, Sirmans 1992). The large concentration of power in a small band of frequencies centered at zero tends to bias both velocity and spectrum width estimates toward zero while increasing the reflectivity estimate.

Equally known is the mitigation of ground clutter contamination. A high pass filter tuned to capture the Doppler characteristics of the ground clutter can mitigate the contamination and provide meaningful estimates. Sirmans (1992) detailed the use of a five-pole elliptic infinite impulse response (IIR) filter for the NEXRAD WSR-88D radar system to mitigate ground clutter. A notch width parameter selection of low, medium and high allowed the operator to tune the filter to suppress varying levels of clutter contamination. In 2004, Ice et. al. (2004a, 2004b) evaluated the Gaussian Model Adaptive Processing (GMAP) (Siggia and Passarrelli 2004) filter as a replacement GCF for the NEXRAD WSR-88D radar system. The main advantages of this spectral GCF are its ability to automatically tune the filter with a single parameter and to recover spectral coefficients in the stop band of the filter.

Although mitigation of ground clutter is rather straight forward, filtering also has its drawbacks in that meteorological estimates along the zero-isodop (i.e., the contour of near-zero radial velocity weather) are biased or completely removed. When a bias is observed, the GCF induces a slight shift in the velocity estimate away from zero while increasing the spectrum width and reducing the reflectivity estimates. Thus, judicious application of the GCF by the operator is warranted (Chrisman et. al. 1994). Recently, an automated ground clutter detection algorithm, Clutter Mitigation Decision (CMD) (Hubbert et. al. 2009), designed by scientists and engineers at the National Center for Atmospheric Research (NCAR) has been implemented into the NEXRAD WSR-88D radar system (Ice et. al. 2009). The fuzzy logic based algorithm provides real time ground clutter mitigation decision eliminating the need for operator interaction.

Here we show an efficient GCF algorithm, CLEAN-AP, which combines both the detection and mitigation of ground clutter contamination from the weather radar returns. The filter dynamically changes its clutter suppression characteristics to optimally match the ground clutter environment. When a large ground

clutter contamination is detected the filter provides clutter suppression of up to 60 dB; and, when no ground clutter contamination is present, the filter provides no suppression of weather signals.

2. GROUND CLUTTER DETECTION

The digitized complex, in-phase and quadrature-phase (I and Q), voltage samples of received distributed weather echoes of a coherent Doppler weather radar are independent random variables in phase and amplitude (Doviak and Zrnić 1993). If the observation time of this stochastic process is limited to a several milliseconds, the process can be considered wide-sense stationary (WSS). Typical WSR-88D dwell times range from about 35 ms to about 80 ms in Surveillance and Doppler modes to about 250 ms in Clear Air mode (FMH-11). As such, spectral moment estimation is a useful tool to analyze these digitized voltages and extract meteorological estimates from other undesired signals such as ground clutter.

Typically, the periodogram is used to create the power spectral density; however, the periodogram may not be suited to identify ground clutter contamination. Additionally, exact replication of the power spectral density is not possible with a finite dwell time using the digital Fourier transform (DFT) unless the received signals are exactly periodic over the basis of the transform. Since the digitized I and Q voltages represent a continuum of received frequencies, the aperiodic received signals will spread (leak) across the frequency domain of the DFT. Tapered windows such as Hamming, von Hann (Hanning), or Blackman can be used to control the amount of spectral leakage at the cost of decreased resolution and increased variance of the estimates (Harris 1978, Nuttall 1981).

Spectral leakage is an unfortunate side effect of the limited record length of the digitized signal, but increased record lengths would most likely violate the WSS notion for the weather estimate and result in impractical dwell times. Fortunately, spectral leakage can be measured using the phases of the coefficients in the linear cross-correlation spectrum (here out referred to as cross-spectrum) of the signal with itself as:

$$F(k) = X_k^*(m)X_k(m+l) \quad (1)$$

where X = DFT($d \cdot x$), k is the coefficient of the DFT, m is the sample index, l is the delay or lag, d is the tapered window and x is the digitized received complex voltage.

It is easy to show that when the tapered window (d) is rectangular, the cross-spectrum in equation (1) is the periodogram for l = 0 and leads to a complex spectrum for which the sum is the lag-l autocorrelation when l > 0. The cross-spectrum in equation (1) preserves the phase relation of both periodic and aperiodic signals. Thus, each coefficient in the cross-spectrum of equation (1) becomes the superposition of a single periodic signal with all the aperiodic signals that make up the digitized I and Q samples. The aperiodic signals bias the coefficients of the cross-spectrum and the argument of the resultant phasor indicates the amount of bias.

An analysis of the cross-spectrum of equation (1) created by using a delay of 1 sample (l = 1), reveals that narrow spectrum width signals provide increased phase bias than a like signal with a larger spectrum width. This is significant since the spectrum width of weather is expected to be much greater (2 m/s to 4 m/s in convective storms) than the spectrum width of ground clutter (< 0.3 m/s) (Sirmans 1992).

Fig. 1 shows the magnitude (left) and phase (right) relationship of the cross-spectrum at lag-1 of two 20 dB signals with a velocity of 0 m/s. The signal in blue has a wide spectrum width of 4 m/s and the signal in red has a narrow spectrum width of 0.3 m/s. The green line in the phase plot indicates that periodic signals are not affected by the presence of aperiodic signals in the signal (e.g., white noise); whereas, deviations from the green line indicate biases caused by aperiodic signals present in the spectrum. Note that where the signal is present, the narrow spectrum width signal has more coefficients that are phase biased than does the wider spectrum width signal. This behavior of narrow spectrum width signals is due to the large power/frequency gradient (i.e., large concentration of power in a small band of frequencies) and provides the method to identify ground clutter contamination near zero velocity used in the CLEAN-AP filter. In regions where the signal drops near the noise level, the phase becomes random.

3. CONTROLLING SPECTRAL LEAKAGE

As mentioned, a true representation of the power spectral density cannot be achieved from the digitized complex voltages due to the finite observation period; thus, it becomes necessary to monitor the intrinsic spectral leakage of our time-limited signals. It should be noted that spectral leakage in and of itself is not a problem, but the presence of two signal sources (e.g., ground clutter and weather) impinging on each other is a problem. Take for example a pure tone at a frequency that is midway between two basis vectors of the DFT. The pure tone will be spread to the maximum extent. The spectral leakage can be visualized as the convolution of the tapered window spectrum with this aperiodic tone. Using the cross-spectrum at lag-1, the phase is constant at a single phase (representative of the frequency of the signal).

An example of a pure tone that is sampled midway between the basis vectors of the DFT is shown in Fig. 2. Since the cross-spectral phase is equal throughout the Nyquist co-interval, the magnitude of the sum of the cross-spectrum coefficients at lag-1 (or at any lag) is equal to the magnitude of the sum of the cross-spectrum at lag-0 (i.e., periodogram). That is, the pure tone signal is completely correlated at all lags of the cross-spectrum as expected.

To preserve the superposition of the pure tones of the weather signal, a method is needed that ensures clutter contamination does not bias the coefficients of the weather signal. Tapered windows provide a method to smooth (whiten or flatten) the cross-spectrum (Schwartz and Shaw 1975); thus, controlling the clutter

power gradient across frequencies. The consequence of this smoothing process is the loss of fidelity of the weather signal in the form of increased variance and loss of resolution (Torres 2007).

There are many sources in the literature that describe the effects of tapered windowing, so this paper will not review these effects. However, there are two characteristics of the tapered window spectrum that are of interest when controlling spectral leakage: highest sidelobe level and sidelobe falloff rate. Harris (1975) and Nuttall (1981) detail these characteristics for many of the common tapered windows and Table 1 provides a quick reference to five windows used in the CLEAN-AP filter. Although the Hamming window has a lower sidelobe level than does the Hanning window, it is listed first in Table 1 because of the sidelobe falloff rate is much lower.

Table 1. Tapered window sidelobe characteristics

Window	Highest Sidelobe Level (dB)	Sidelobe Falloff Rate (dB/octave)
Rectangular	-13	-6
Hamming	-43	-6
Hanning (a = 2.0)	-32	-18
Blackman	-58	-18
Blackman-Nuttall	-98	-18

The highest sidelobe level and the sidelobe falloff rate of the tapered window provide the method to control spectral leakage. If the clutter-to-noise ratio (CNR) is limited to the highest sidelobe level, then the leakage of the clutter signal away from zero will occur at or below the noise level. Additionally, by choosing a tapered window which exhibits a good sidelobe falloff rate, the clutter contamination will be suppressed well below the noise level concentrating the clutter bias at frequencies near zero. An estimation of CNR used by the CLEAN-AP filter is provided by comparing the average DC (or zero-frequency) power to the noise power:

$$\mathrm{CNR} = \frac{\frac{1}{M}\left|\sum_{m=0}^{M-1} x(m)\right|^2}{\mathrm{noise}} \qquad (2)$$

4. CLEAN-AP ALGORITHM DESCRIPTION

For each range bin:

a. Compute the estimated CNR using equation (2)

b. Select a tapered window from Table 1 such that the estimated CNR does not exceed the highest sidelobe level.

c. Create two complex time-series as: $x_1 = x(m_1)$ and $x_2 = x(m_2)$, where $0 \le m_1 < M-1$ and $1 \le m_2 < M$.

d. Compute the DFT of windowed spectrum X_1 and X_2 from x_1 and x_2 respectively.

e. Compute the periodogram from X_1 and the lag-1 cross-spectrum using equation (1) (with X_1 as the first term and X_2 as the second term).

f. Compare the absolute value of the argument of each coefficient of the cross-spectrum at lag-1 to a clutter bias threshold parameter (angular error).

g. Notch the coefficients of the periodogram and cross-spectrum where the cross-spectrum coefficients are less than the angular error and exceed the spectral noise level.

h. Identify the range bin as filtered if a notch has been applied.

i. Linearly interpolate across the spectral notch width for both the periodogram and the cross-spectrum.

j. Estimate the meteorological parameters per Doviak and Zrnić (1993).

5. SIMULATION ANALYSIS

Reasonable weather and clutter simulations are provided by modeling the signals as having a Gaussian power spectrum (Sirmans and Bumgarner 1975, Zrnić 1975) with a larger number of coefficients than are needed in the time series. Using simulations, the clutter filter characteristics and clutter detection capability of the CLEAN-AP filter can be shown. The following paragraphs depicts some selected performance characteristics of the filter.

5.1 *Ground Clutter Suppression*

A good indication of the performance of the CLEAN-AP filter can be obtained from the amount of ground clutter suppression that the filter can provide. Simulations of clutter/weather mix were created and processed through the CLEAN-AP filter. Fig. 5 shows a scatter plot of power bias of the filtered weather as a function of increasing clutter-to-signal ratio (CSR) levels. As seen in the figure, the filter provides about 60 dB of clutter suppression without biasing the weather signal power estimate. After a CSR of about 60 dB, over suppression of the simulated weather signal is seen by the negative biases exhibited in the scatter plot. At an approximate CSR of 80 dB and above, the clutter levels saturate the weather signal as observed by positive biases. To place the clutter suppression performance into context, the CLEAN-AP filter easily provides the clutter suppression requirements of 50 dB required for operations in the U.S. network of weather surveillance radars (i.e., the NEXRAD network of WSR-88D radars).

5.2 *Reflectivity Bias*

The reflectivity bias from the filtering process when ground clutter is not present is shown in Fig. 6 through Fig. 8. In these figures, power bias is shown as a function of the spectrum width using simulations of a 20 dB weather signal with 0 m/s velocity and varying spectrum widths. Different pulse-repetition-frequencies are used for the three weather modes described in the FMH-11. The CLEAN-AP filter provides small biases over the range of spectrum widths. Performance is shown against the filters used (past and present) in the WSR-88D for the operational scanning modes: Clear Air, Surveillance, and Doppler. The blue dots on each plot indicate the WSR-88D reflectivity bias requirements (WSR-88D SS).

5.3 *Ground Clutter Detection*

The CLEAN-AP filter has the ability to identify ground clutter in the presence of weather echoes as shown in Fig. 9 where clutter likelihood is plotted as a function of CSR. The detection rate is calculated as the mean of 5100 detections (identified filtering of a range bin as in 4h above) at each CSR level for a simulated 20 dB signal with varying velocities and a 4 m/s spectrum width. The CLEAN-AP filter has approximately 50% detection rate down to -12 dB CSR and about 83% detection rate at 0 dB CSR with over 90% detection rate above about 3.7 dB CSR.

5.4 *Velocity Bias*

The CLEAN-AP filter has no appreciable velocity bias (< 0.8 m/s) over the entire Nyquist co-interval for a composite signal with 55 dB CSR as seen in Fig. 10. The scatter plot shows the filtered velocity bias as a function of 100 simulations for each velocity tested. The CLEAN-AP filter easily meets WSR-88D velocity bias requirments (< 2 m/s) at the highest clutter suppression (50 dB) levels.

5.5 *Spectrum Width Bias*

The CLEAN-AP filter provides unbiased spectrum width estimates with low error of estimates as seen in Fig. 11 when providing 55 dB of clutter suppression. In this figure, the green line shows zero bias; while the red lines indicate the WSR-88D allowed bias of 2 m/s for filtered spectrum width estimates. The red circles indicate the estimate mean and the red bars indicate the standard deviation at the mean. The CLEAN-AP filter easily meets WSR-88D spectrum width bias and error of estimate requirments (< 2 m/s) at the highest clutter suppression levels (50 dB).

5.6 *Window Selection*

Closely related to low errors of estimates is the selection of low dynamic-range tapered windows. On the other hand, high dynamic-range tapered windows are needed for adequate clutter suppression. The CLEAN-AP filter provides automated tapered window selection among five windows as listed in Table 1. Fig. 11 shows how the CLEAN-AP filter selects the lowest dynamic-range window when ground clutter is low and increasingly selects a higher dynamic-range window as the amount of ground clutter increases. This performance ensures the best possible quality of estimate for a given ground clutter environment.

6. REAL WEATHER EXAMPLES

The CLEAN-AP filter was implemented in the Fall of 2008 into the weather digital signal processing suite of the National Weather Radar Testbed (NWRT) Phased Array Radar (PAR) located in Norman, Oklahoma (Torres et. al. 2009). During the Phased Array Radar Innovative Sensing Experiment (PARISE) (Heinselman et. al. 2009), the CLEAN-AP filter provided automatic ground clutter detection and suppression. In Fig. 11, the CLEAN-AP filter is shown to remove ground clutter caused by anomalous propagation. The filter performance is contrasted against the operational WSR-88D radar system KTLX in Oklahoma City. In the operational system, operators applied filtering at all ranges to combat the dynamic atmospheric conditions as the inversion moved over the region to the North of the radar.

In Fig. 12, normal propagation (NP) clutter contamination biases are shown to be removed from reflectivity, velocity and spectrum width near the NWRT PAR (red circles) without affecting areas outside the clutter regions. The images captured a mesocyclone (yellow circles) just 2 hours before it developed into an EF0 tornado that touched down at lake Stanley Draper in southern Oklahoma City, OK. Note that there are no observable differences inside the yellow circles indicating that the CLEAN-AP filter did not bias the weather estimates in this region.

7. SUMMARY

We have introduced a new spectral GCF, referred to as CLEAN-AP, capable of automatic real-time detection and mitigation of ground clutter contamination in weather radars. We have characterized the statistical performance of the CLEAN-AP filter and compared the performance with NEXRAD WSR-88D standards. Through simulations, we have shown that the filter is capable of providing clutter filtering on par with current techniques, but does so without operator interaction. Examples of the filters real-time performance was shown to remove clutter contamination in both severe AP and NP events without detriment to meteorological estimates as part of the NWRT PAR digital signal processing suite.

ACKNOWLEDGEMENTS

This conference paper was prepared by David Warde and Sebastián Torres with funding provided by NOAA/Office of Oceanic and Atmospheric Research under NOAA-University of Oklahoma Cooperative

Agreement #NA17RJ1227, U.S. Department of Commerce. The statements, findings, conclusions, and recommendations are those of the authors and do not necessarily reflect the views of NOAA or the U.S. Department of Commerce. The authors would like to thank the NSSL software engineers, with special thanks to Eddie Forren for his invaluable expertise in implementing the CLEAN-AP filter on the NWRT PAR and Rick Adams for his constant attention to data collection opportunities and replay of numerous hours of NWRT PAR time-series data.

REFERENCES

Chrisman, J., D. Rinderknecht, and R. Hamilton, 1994: WSR-88D Clutter Suppression and Its Impact on Meteorological Data Interpretation. Postprints, The First WSR-88D Users' Conference, Norman, OK, USA, Oct 1994.

Doviak, D. and D. Zrinć, 1993: Doppler Radar and Weather Observations, 2nd edition. Academic Press.

Federal Meteorological Handbook, Number 11, 1989. Part B, Doppler radar theory and meteorology.

Harris, F., 1978: On the use of windows for harmonic analysis with the discrete Fourier transform, *Proc. IEEE*, vol. 66, 51-83.

Heinselman, P., S. Torres, R. Adams, C. Curtis, E. Forren, I. Ivic, D. Priegnitz, J. Thompson, and D. Warde, 2009: Phased array radar innovative sensing experiment, *Preprints 34th Radar Conf*., Williamsburg, VA, Amer. Metoer. Soc.

Hubbert, J., M. Dixon, and S. Ellis, 2009: Weather radar ground clutter. Part II: Real-Time Identification and Filtering, *Journal of Atmos. Oceanic Technol.*, vol. 26, 1118-1196.

Ice, R., D. Warde, D. Sirmans, D. Rachel, 2004a: Report on Open RDA – RVP8 Signal Processing, Part 1 – Simulation Study, WS-88D Radar Operations Center Report, January 2004. 87 pp.

___, D. Warde, D. Sirmans, D. Rachel, 2004b: Report on Open RDA – RVP8 Signal Processing, Part 2 – Engineering Analysis with Meteorological Data, WS-88D Radar Operations Center Report, July 2004. 56 pp.

___, R. Rhoton, J. Krause, D. Saxion, O. Boydstun, A. Heck, J. Chrisman, D. Berkowitz, W. Zittel, and D. Warde, 2009: Automatic clutter mitigation in the WSR-88D, design, evaluation, and implementation, *Preprints 34th Radar Conf*., Williamsburg, VA, Amer. Metoer. Soc.

Schwartz, M. and L. Shaw, 1975: Signal Processing: Discrete Spectral Analysis, Detection, and Estimation. McGraw-Hill.

Siggia, A., and J. Passarelli, 2004: Gaussian model adaptive processing (GMAP) for improved ground clutter cancellation and moment calculation. *Proc. Third European Conf. on Radar in Meteorology and Hydrology*, Visby,Gotland, Sweden, ERAD, 67–73.

Sirmans, D., and Bill Bumgarner, 1975: Numerical comparison of five mean frequency estimators. *Journal of Applied Meteorology*, vol.14, 991-1003.

___, 1987: NEXRAD suppression of land clutter echo due to anomalous microwave propagation - Part I, NSSL Internal Report. 54 pp.

___, 1992: Clutter filtering in the WSR-88D, OSF Internal Report. 125 pp.

Torres, S., C. Curtis, D. Zrnic, M. Jain, 2007: Analysis of the new NEXRAD spectrum width estimator. *Proc. 33rd Conference on Radar Meteorology*, Cairns, Australia, AMS, CD-ROM, P7.8.

___, ___, I. Ivic, D. Warde, E. Forren, J. Thompson, D. Priegnitz, and R. Adams, 2009: Update on signal processing upgrades for the National Weather Radar Testbed. Preprints, 25th IIPS for Meteorology, Oceanography, and Hydrology, Phoenix, AZ, USA, Amer. Meteor. Soc.

Nuttall, A., 1981: Some windows with very good sidelobe behavior, *Trans. ASSP*, vol. 29, pp. 84-91.

WSR-88D System Specifications 2810000H, 25 April 2008, Radar Operations Center, 160 pp.

Zrnić, D. S., 1975: Simulation of weather like Doppler spectrum and signals, Journal of Applied Meteorology, 14, 619-620.

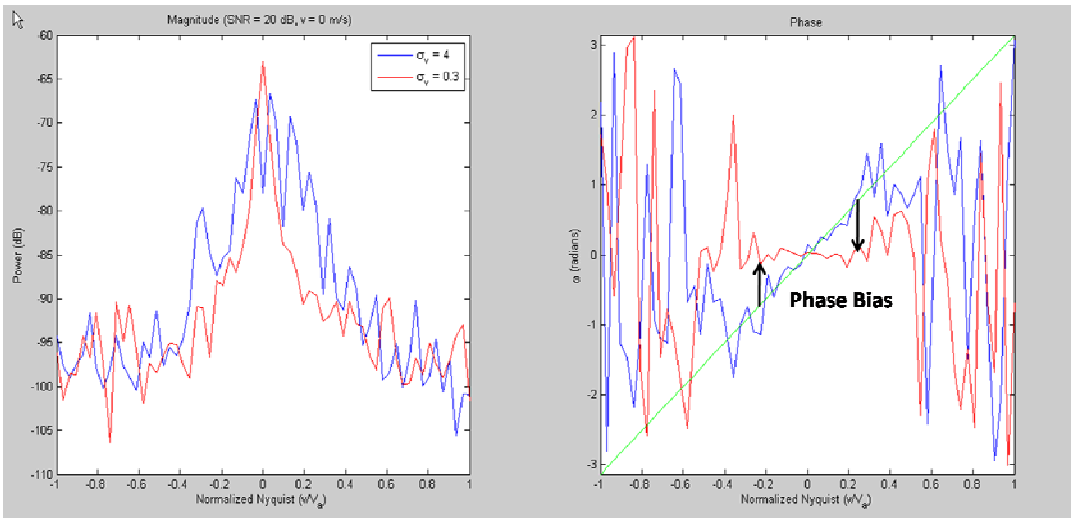

Fig. 1. Lag-1 Cross-Spectrum of two signals:
sig1 (SNR = 20 dB, v = 0 m/s, σ_v = 4 m/s) and sig2 (SNR = 20 dB, v = 0 m/s, σ_v = 0.3 m/s)

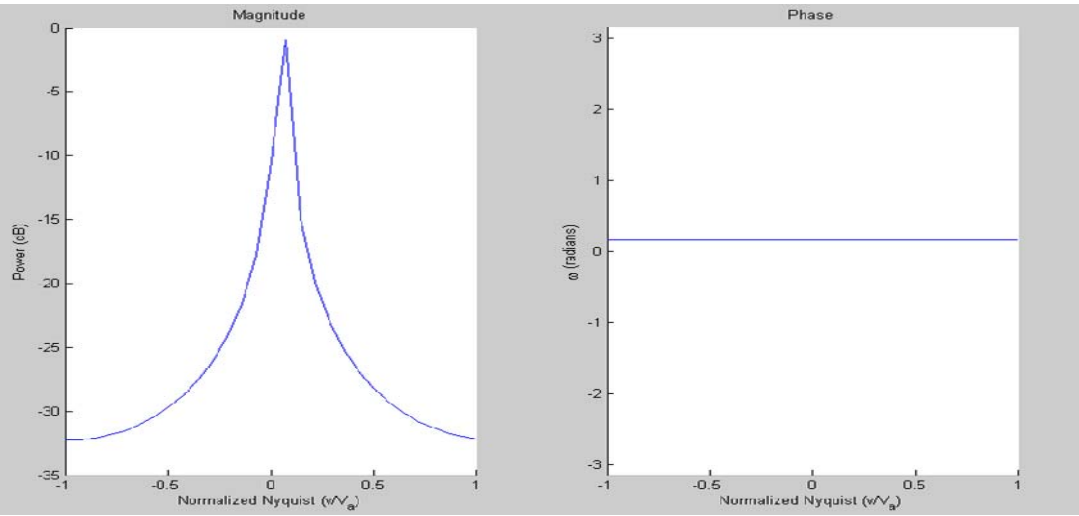

Fig. 2. Lag-1 Cross-Spectrum of pure tone leakage across Nyquist co-interval (v/V_a = 0.05 ≡ ω/π)

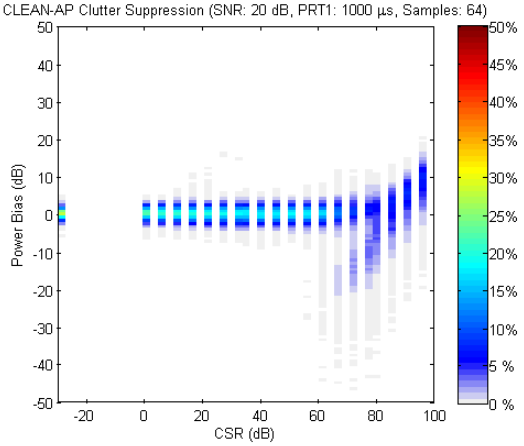

Fig. 3. Example of Clutter Suppression exhibited by the CLEAN-AP filter

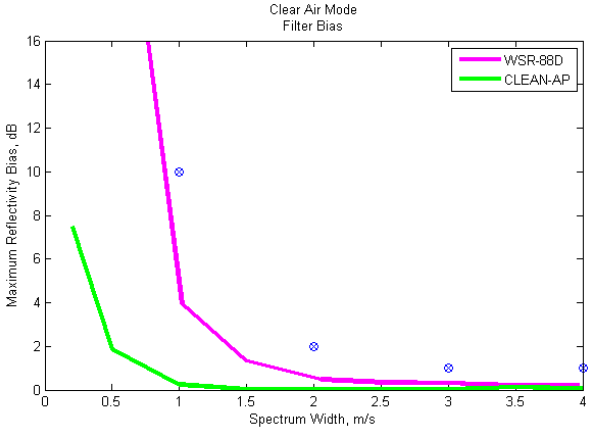

Fig. 4. Reflectivity bias in Clear Air Mode for the WSR-88D and the CLEAN-AP filters.

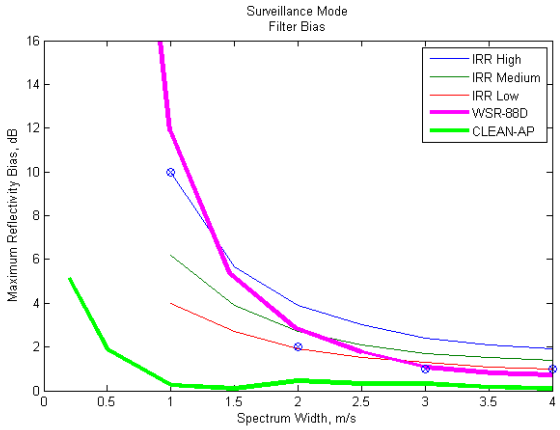

Fig. 5. Reflectivity bias in Surveillance Mode for the WSR-88D and the CLEAN-AP filters.

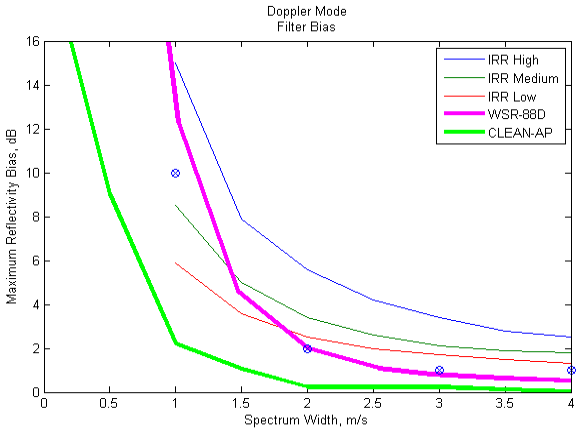

Fig. 6. Reflectivity bias in Doppler Mode for the WSR-88D and the CLEAN-AP filters.

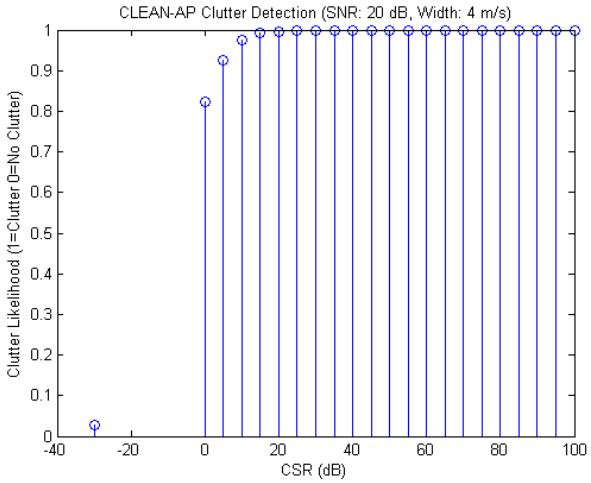

Fig. 7. Example of likelihood of ground clutter detection using the CLEAN-AP filter.

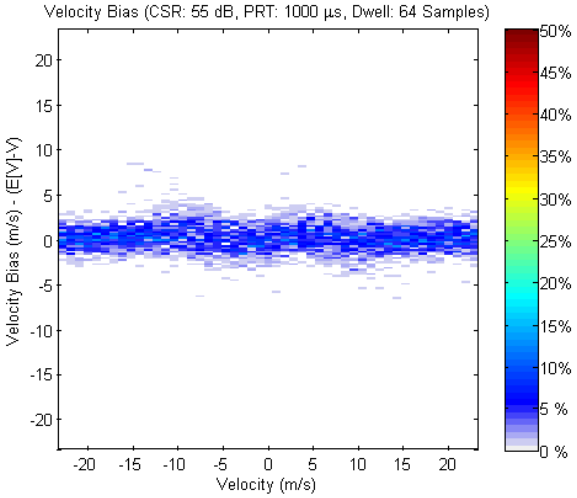

Fig. 8. Example of velocity bias in a high-suppression regime for the CLEAN-AP filter.

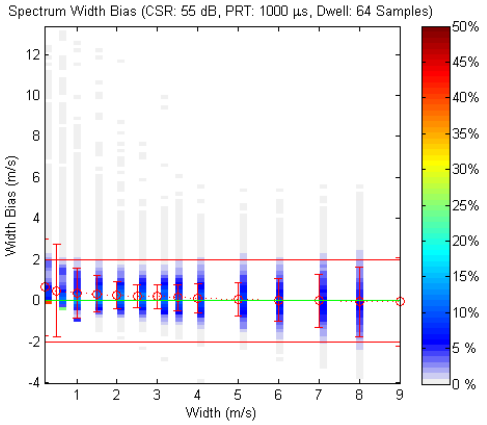

Fig. 9. Example of spectrum width bias and error of estimate in a high-suppression regime for the CLEAN-AP filter.

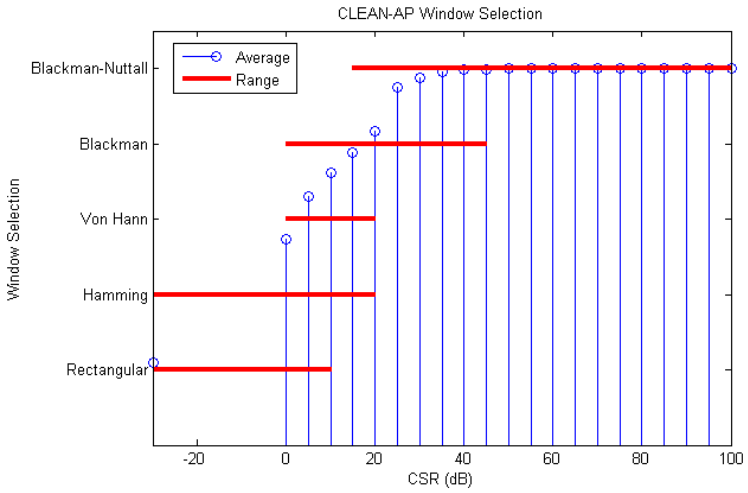

Fig. 10. Window selection in the CLEAN-AP filter.

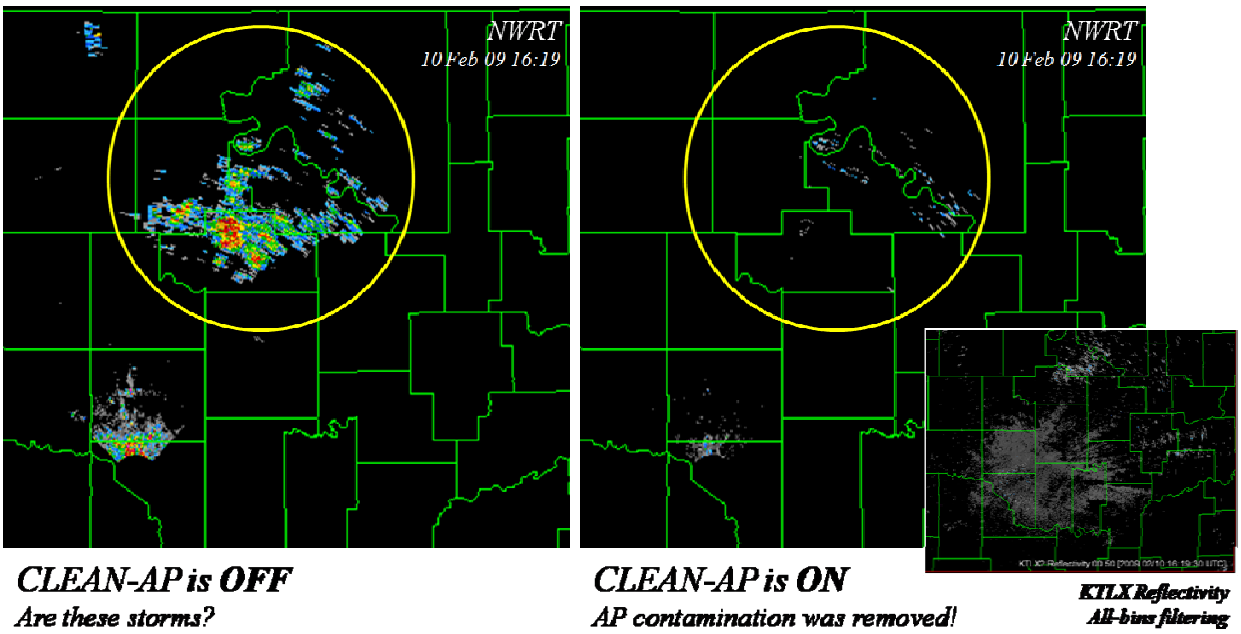

Fig. 11. Displays of Reflectivity from NWRT (with and without CLEAN-AP applied) compared with KTLX (Oklahoma City WSR-88D system) during normal operations.

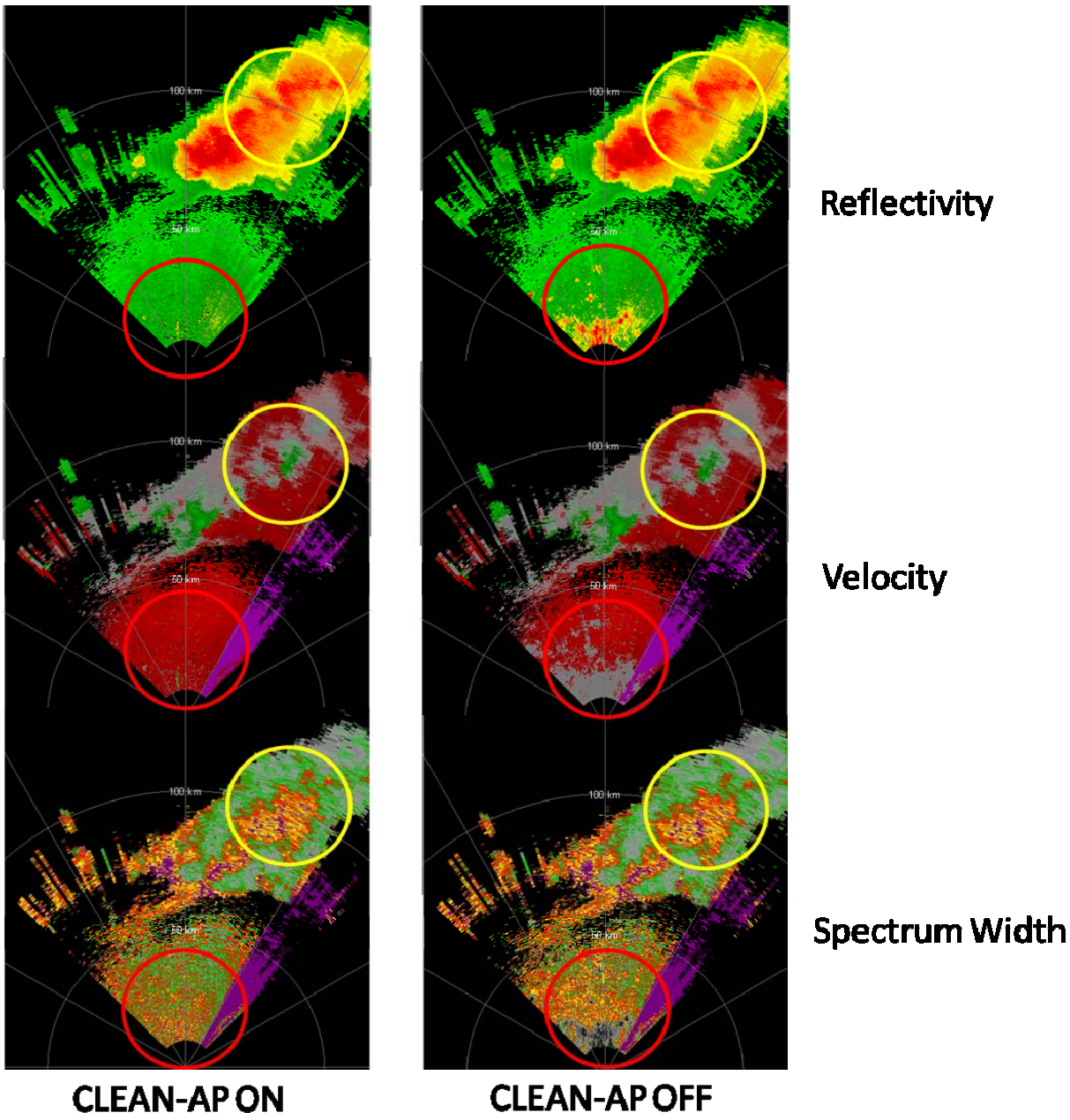

Fig. 12. Displays of reflectivity, velocity, and spectrum width with CLEAN-AP on and off, the red circles indicate where normal clutter contamination is present when not filtering (reflectivity is biased high, velocity is biased toward zero, and spectrum width is biased toward zero in this region)